Finite Element Based Lifetime Predictions of Wind Turbine Blade Coatings

Tristan Hamers

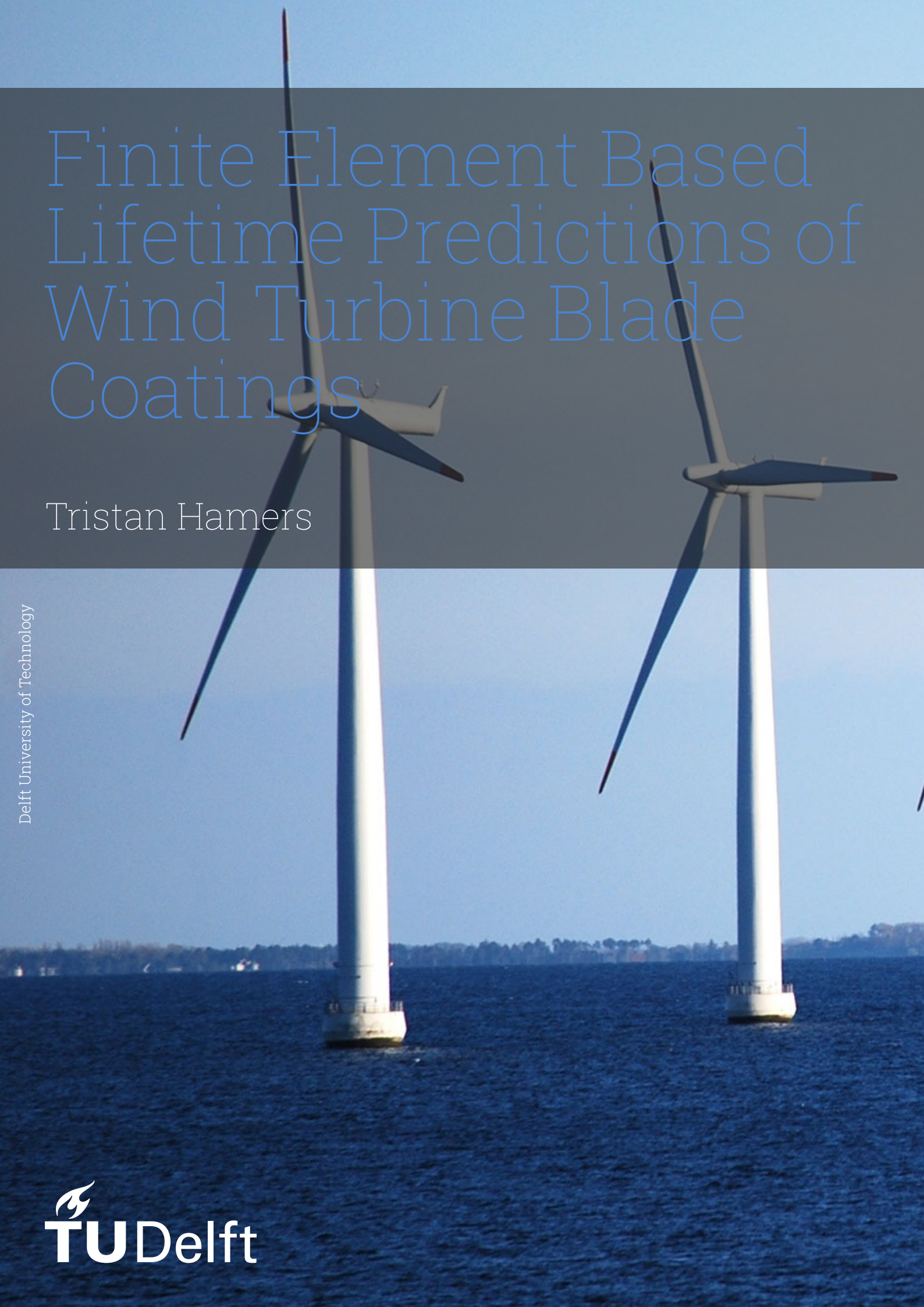

Delft University of Technology

TU Delft

Finite Element Based Lifetime Predictions of Wind Turbine Blade Coatings

by

Tristan Hamers

In partial fulfilment of the requirements of the degrees:

Master of Science

in Engineering (European Wind Energy)

At the Technical University of Denmark

Master of Science

in Aerospace Engineering

At Delft University of Technology

to be defended publicly on Tuesday August 16, 2022 at 9:00 AM.

Student number:	4483022	
Project duration:	November 1, 2021 – August 16, 2022	
Thesis committee:	Dr. J.J.E Teuwen	TU Delft - supervisor
	Assoc. Prof. L.P. Mikkelsen	DTU - supervisor
	Assoc. Prof. K. Masania	TU Delft
	Dr. ir. J.A. Pascoe	TU Delft
	Prof. E. Lund	DTU

An electronic version of this thesis is available at http://repository.tudelft.nl/.

Technical University of Denmark

d

Preface

The following report covers the work performed for the completion of the thesis for the MSc. program: European Wind Energy - Rotor Design, with a specialisation in structures and composites. The majority of the project has been performed at DTU Wind Energy, within the scope of the DURALEDGE research project. Furthermore, a substantial contribution comes from the faculty of Aerospace Engineering of Delft University of Technology.

Further contributions are made to the following:

I Nikolai Frost-Jensen Johansen, *Impact Fatigue and thermal effects*, 3rd International Symposium on Leading Edge Erosion of WT Blades [1], 03-02-2021: 10:20-10:40, online

- Student performed data analysis of raw SPIFT test data.

II Tristan Willem Hamers, *RE lifetime prediction workflow*, DURALEDGE 2-days topical workshop, 08-06-2022 09:00-10:30, Risø DTU National Laboratory for Sustainable Energy

- Student is the main author and presenter.

Author: Tristan Willem Hamers
Supervisors: Lars Pilgaard Mikkelsen
Julie Teuwen
Co-Supervisors: Jakob llsted Bech
Kristine Munk Jespersen

[1] https://www.conferencemanager.dk/3rdlee

Acknowledgements

The work performed in this thesis would not have been possible without the guidance and advice of my two main supervisors Lars Pilgaard Mikkelsen and Julie Teuwen. Your constant feedback and suggestions helped me navigate through the challenges of the day-to-day thesis work.

Furthermore I would like to thank my co-supervisor Kristine for introducing me to the workflow. Thank you Jakob for the numerous 'quick chats' providing me with fresh ideas and renewed motivation. A special mention for Nicolai Frost-Jensen Johansen who guided me through the SPIFT testing campaign and assisted with any maintenance requirements for the SPIFT equipment and the analysis of the validation RET data. Finally, thank you Nick Hoksbergen for performing all the numerical simulations I required and the in-depth discussions that followed. It has been a pleasure working with all of you.

A special gratitude to all contributors to the DURALEDGE project for allowing me to work with the new generation coating materials, contribute to project meetings and allowing me to present my work in the topological workshop. The discussions that followed provided me with invaluable feedback and renewed insights into the material.

My final thanks goes out to my family and girlfriend Amaya for their unconditional support. This work would not have been possible without you.

Abstract

Operating turbines suffering from leading edge erosion (LEE) experience significant (up to 5%) annual energy production (AEP) loss and require expensive maintenance campaigns. Evaluation of state-of-the-art coating systems relies on rain erosion testing (RET) with no accepted method for the computational evaluation of the coatings lifetime. In this work, the computation framework for rain erosion developed in the DURALEDGE research project of DTU Wind Energy is subjected to analyses and used for the comparison of erosion performance of four novel leading-edge coating systems. Improvements for the computation workflow are proposed and implemented into the workflow. Furthermore, relevant conclusions are drawn linking the material's visco-elastic properties to erosion performance.

Summary

Leading-edge erosion is a phenomenon that causes degradation of operating wind turbine blades due to environmental factors such as rain, hail or particles in the air. It can cause significant aerodynamic degradation of the blade and thereby lower annual energy production. The framework developed within the scope of the DTU wind energy DURALEDGE research project provides a benchmark computational evaluation methodology which can be used for the evaluation of leading-edge protection systems. In this work, four novel leading-edge coating materials with varying binder (357 and 368) and filler volume fractions (15% and 30%) have been analysed, utilising this workflow. These materials will be referred to as BxxxFVyy. Furthermore, the different stages of the workflow have been subjected to detailed analysis and improvements have been proposed.

Two main steps can be distinguished in the computational workflow: material analysis and the rain erosion lifetime prediction. The material analysis captures the coating material's visco-elastic properties in terms of mastercurves, based on experimental DMTA data. The material's fatigue properties are expressed in a stress-based SN curve, based on SPIFT (Single Point Impact Fatigue Test) analysis of the coating system. The rain erosion lifetime tool combines the results of a single droplet impact finite element simulation, with a python-based rain erosion simulation tool. The workflow is tuned towards recreating RET whirling arm test conditions and can be validated with experimental data.

In the processing of the DMTA data, an automated master curve construction tool has been developed, aimed at improving the accuracy and reproducibility of the final mastercurve. However, the final mastercurve remains a source of uncertainty, especially in the extreme frequency range. This uncertainty originates from extrapolating the DMTA data from the frequency range available in conventional DMTA testing ($[10^{-1}, 10^{3}]$ Hz), to the frequency range relevant to impact fatigue ($>10^{5}$ Hz), by utilising the time-temperature superposition principle. This is further increased in the model calibration step where the Yeoh hyperelastic model and a Prony series are fitted to the final materials mastercurve.

Comparing the novel coating materials mastercurve, it is found that the binder type dominates the visco-elastic behaviour of the mastercurve. Binder system 357 shows relatively higher damping in the high-frequency range of the curve when compared to binder system 368. Furthermore, for both binder systems, a higher filler volume fraction shows a slightly lower energy dissipation when compared to the low filler volume case in the high-frequency region. However, this difference is small and is expected to fall into the uncertainty range of the final curve.

The material's behaviour upon impact is investigated utilising infrared (IR) and acoustic emission (AE) measurement during SPIFT testing. Binder system 357 shows, relative to binder system 368, higher surface temperatures and lower energy absorption by the AE sensor, indicating greater energy dissipation upon impact. This is in line with observations made in the mastercurves, where a higher value of tanδ is found in the high-frequency range for this binder system. For the filler volume fraction, opposite behaviour is seen between the binder systems. For binder system 368, a higher filler volume fraction leads to increased energy dissipation upon impact, in line with observations made in the mastercurves. However, for binder system 368, an opposite trend is seen. This could indicate inaccuracies in the mastercurves for this binder system, or be explained by a difference in reference temperature of the mastercurve (20 °C) and ambient operating temperature in SPIFT analysis (28 °C).

Furthermore, the material systems are subjected to impact fatigue testing. For both filler volume fraction cases of binder system 357, no relevant failure patterns could be distinguished in the initial fatigue tests. This means a VN curve can not be constructed for coating materials B357-FV30 and B357-FV15. For binder system 368, the high filler volume fraction shows a lower lifetime for the full range of impact velocities in SPIFT testing. The SPIFT testing results are characterised by defect-driven failure. This, combined with subjectivity introduced in the visual damage detection, leads to substantial uncertainty in the SPIFT results.

Finally, the RE lifetime prediction tool, based on the single droplet impact simulation is further investigated. The velocity dependence of the lifetime prediction at the start of this work was underestimated. The problem is tracked numerical noise, originating in the single droplet impact finite element simulation, dominating the damage calculation. Two alternative solution methods are proposed: the minimum stress amplitude threshold (MST) and the stress amplitude conversion (SAC) method. MST filters out low amplitude fluctuations in the stress history by placing a minimum value on stress variations to be considered in the damage calculation. However, no physical basis is found for this minimum stress value. In SAC, the full stress history of a single droplet is converted into a single stress wave of which the amplitude is determined by the extreme stress values of the impact event. This is similar to the methodology used in the determination of the damage criteria. SAC is the accepted method and is implemented in the workflow.

The lifetime prediction is performed for coating materials B368-FV30 and B368-FV15. B368-FV15 is predicted to have the greatest lifetime, opposite to the results from the SPIFT analysis. This is due to an extreme extrapolation of the SPIFT impact fatigue results represented in the stress-based SN curve damage criteria. Validation of these results reveals the relative performance of the two material systems is captured. Furthermore, the validation data reveals the high damping binder system (357), combined with a low filler volume (15%) shows optimal RET performance.

Contents

List of Figures

List of Tables

Nomenclature

δ	Phase angle
$\dot{\epsilon}$	Strain rate
ϵ	Strain
η	Coefficient of viscosity
γ	Droplets per m^2
λ_i	principle stress ratio's
ω	Radial frequency
ω_{Ti}	Frequency sweep for temperature i
ψ	Volume concentration
ρ_0	Liquid impact density
σ	Stress
τ	Relaxation time
θ	Impact angle
A	SN parameter
a_T	Horizontal shift factor
B	SN parameter
C_0	Speed of Sound
C_d	Drag coefficient
C_i	William Landel Ferry constant
C_l	Lift coefficient
C_{i0}	Yeoh model paramaters
D	Damage Parameter
D_{i0}	Yeoh model paramaters

E''	Loss modulus
E'	Storage modulus
$E*$	Complex modulus
E	Young's modulus
f	Frequency
G	Shear modulus
g_i	Shear moduli
H	Activation energy
H	Impingement
h	Height droplet equivalent cylinder
I	Rain intensity
I_i	Cauchy-green deformation tensor
k_i	Bulk moduli
L	Length evaluation surface
$N0$	Number specific impacts
N	Number of Impacts
n_i	Eigenvector
P_{hammer}	Water Hammer Pressure
q	Droplet concentration
R	Radius
S_{ij}	Cauchy stress tensor
T_d	Degradation temperature
T_g	Glass transition temperature
t_{sim}	Simulation time
U_i	Impingement rate
V	Wind speed
v_{drop}	Droplet free-fall velocity

V_{impact} Impact velocity

V_{rated} Rated Wind speed

V_{tip} Tip Speed

W Helmholtz free energy

Z Dynamic Impedance

List of Abbreviations

AEP Annual Energy Production

AE Acoustic Emission

AMPS Absolute Maximum Principle Stress

DMTA Dynamic Mechanical Thermal Analysis

DURALEDGE Durable leading edges for high tip speed wind turbine blades

FEM Finite Element Method

GFRP Glass Fibre Reinforced Polymer

HAWT Horizontal Axis Wind Turbine

IR Infra-red

LEE Leading Edge Erosion

MAPS Maximum Principle Stress

MIPS Minimum Principle Stress

PU Polyurethane

RET Rain Erosion Test

RE Rain Erosion

SF Sampling Frequency

SI Sampling Interval

SPIFT Single Point Impact Fatigue Tester

ST Simulation Time

SVM Singed Von Mises

TSR Tip Speed ratio

VM Von Mises

CHAPTER 1

Introduction

1.1 Trends in Global Wind Energy

The 2015 Paris agreement states that the global temperature rise due to human involvement has to be kept well below 2 °C. This can only be achieved by changing the global energy market from its fossil fuel dependency to renewable energy sources. This is where wind energy has already proven to play a vital role in the years to come. As of 2020, a total global capacity of 743 GW has been installed globally, with a record increase of 93 GW in 2020 [7]. The International Energy Agency (IEA) published the 'World Energy Outlook (2020)', covering the way the global energy market is likely to evolve over the coming years [8]. The implications for the wind energy market are shown in Figure 1.1. Drastic increase in installed capacity per year is expected over the coming years, indicating the growth the wind energy market will experience.

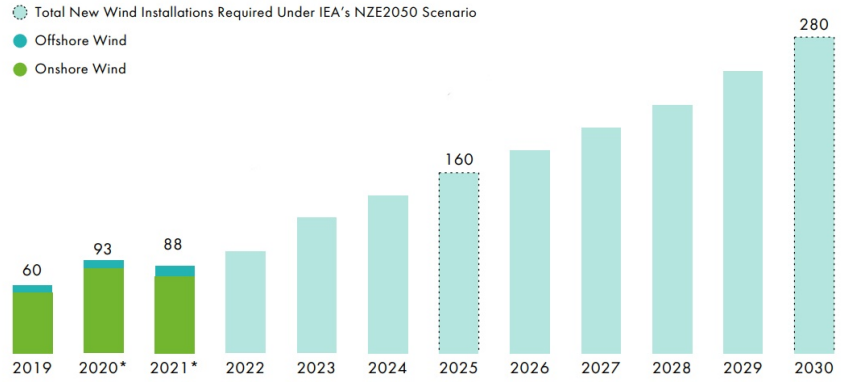

Figure 1.1: Annual wind capacity installation and expectancy's for the coming years. Volume for 2022-2030 are estimates. Adapted from [7].

The majority of this capacity is taken up by the conventional Horizontal Axis Vertical Wind Turbine (HAWT) [24]. In broad terms, this turbine type consists of a tower, nacelle containing a generator and blades. The blades are rotated by the wind, converting its kinetic energy into mechanical energy. The generator, in turn, converts the mechanical energy into electricity. The power production of a turbine is a function of air density, rotor swept area, rotor efficiency and wind speed squared. Figure 1.2 schematically shows the evolution of turbine size and capacity for the last years. A substantial increase in

turbine size can be seen which can be explained by cost evaluation of this type of energy production. Increasing the rotor swept area, increases power output per turbine, lowering overall operating cost [25].

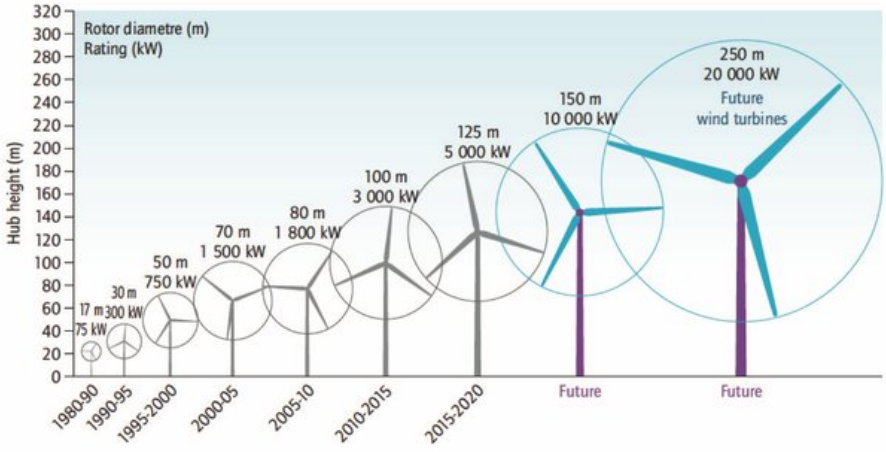

Figure 1.2: Wind turbine capacity and rotor diameter evolution for the last 20 years, including future outlook. From [9].

Increasing the swept area of the rotor means increasing the rotor radius. With optimal aerodynamic conditions often found at tip-speed ratios in the range of eight to ten, tip speeds are expected to increase for the next generation turbines [2]. The relation of tip speed with rotor radius is visualised by Figure 1.3, for a number of turbines currently in operation. As can be seen, tip speeds of 80-100 m/s are not uncommon for operating turbines today. These values for tip speed are highly dependent on turbine operational strategies and are often limited since high tip speeds are associated with leading edge erosion.

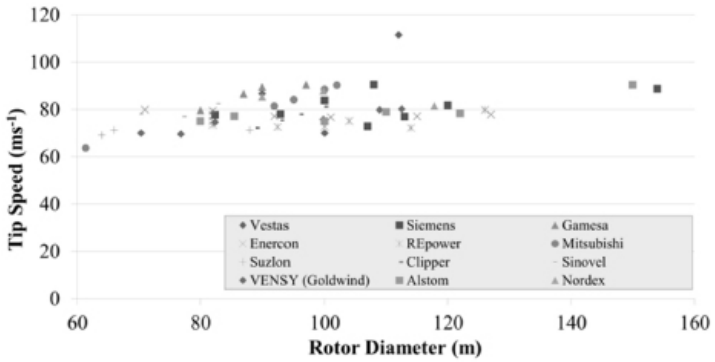

Figure 1.3: Blade tip speed vs rotor diameter for various wind turbine models. From [29].

1.2 Leading Edge Erosion (LEE)

Leading edge erosion is the degradation of the wind turbine's blade leading edge, due to environmental effects such as rain, hail, and sand-or-dust particles in the air. Defects in the blade's leading edge can lead to crack initiation and propagation, cavity creation and the loss of material [20]. A visualisation of the phenomena is shown in Figure 1.4. A wind turbine blade leading edge is shown for a different number of service years and the progression of the erosion is clearly seen. Damage initiation can, in some cases, already be seen after a single year of service. Significant erosion is found after 10 years, severely impacting the aerodynamics of the airfoil.

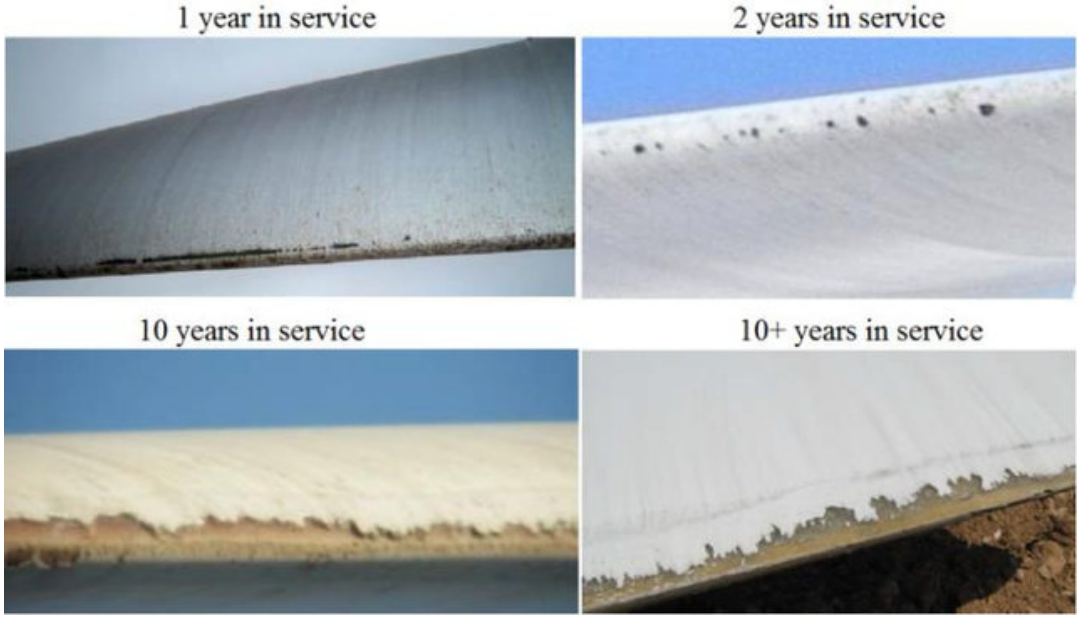

Figure 1.4: Leading edge erosion examples following different number of service years. From [29].

.

The aerodynamics of the airfoil is affected due to the increased surface roughness of its leading edge. The flow is disturbed when travelling over the airfoil, decreasing the operating lift coefficient (C_l) while increasing its drag coefficient (C_d), leading to a reduction in the blade's $\frac{C_l}{C_d}$. This will translate into a decrease in the operating power coefficient, lowering the efficiency of the turbine. For wind speeds above the turbine's rated wind speed, these effects can be partly compensated by its pitch controller. As for the lower wind speeds, energy loss will be experienced [34].

Translating the loss of aerodynamic efficiency in Anual Energy Production (AEP) loss, gives insight into the severity of the problem. Different studies have been performed with a range of losses between 2-5% reported due to different levels of erosion [19] [30]. Seeing

that the effects can already be seen within one to two years of service [36], a great loss can be accumulated over the wind turbine's lifetime when left untreated. This type of loss is unacceptable for wind farm operators and thus expensive maintenance campaigns are required to resolve these issues. This was seen in 2018 when Danish wind farm operator Ørsted was forced to repair up to 2000 offshore wind turbine blades, suffering from leading edge erosion [37]. The high cost associated with these types of repairs is to be avoided in the future, in order to make wind energy an economically attractive green energy source. Understanding leading edge erosion and its underlying mechanisms is vital in accurately predicting its occurrence and its prevention.

1.3 Research Objective

The work performed in this thesis aims to further understand the leading edge erosion phenomena and develop computational tools that can be used for lifetime predictions of leading edge protection systems. It utilises and aims to develop the rain erosion framework developed within DURALEDGE (Durable leading edges for high tip speed wind turbine blades)[1] research project of DTU Wind Energy. For this purpose, the following research objective has been set up:

To investigate potential wind turbine blade leading edge protective solutions by utilising the existing DTU Wind Energy DURALEDGE framework and put forth improvements for the computational evaluation of leading-edge erosion.

This objective can be further split up into tangible goals as below.

[**RG 1**] To investigate the current state-of-the-art of the DTU Wind Energy DURALEDGE framework, by analysing a novel coating material using the existing workflow.

[**RG 2**] To put forth improvements to the existing workflow by critically analysing and evaluating the individual segments of the workflow.

[**RG 3**] To investigate the velocity dependence of the current state-of-the-art lifetime prediction obtained by the DTU Wind Energy DURALEDGE framework.

[**RG 4**] To investigate the effect of binder type and micro-filters in novel leading-edge coating materials, by performing a lifetime analysis of different types of novel coating material systems.

[1] duraledge.dk

1.4 Thesis Outline

In order to meet the above-mentioned research objectives, the following thesis outline is proposed. An elaboration is provided for each Chapter.

Chapter 1 **Introduction**

Chapter 2 **State-of-the-art**
An investigation of the current state-of-the-art of leading edge erosion analysis is provided, accompanied by relevant background information.

Chapter 3 **The DTU Wind Energy DURALEDGE Rain Erosion Framework**
The work conducted in this research is performed within the rain erosion framework of the DTU Wind Energy DURALEDGE research project. The working mechanisms of this workflow are presented.

Chapter 4 **Methodology Evaluation**
The state-of-the-art of the DURALEDGE framework is subjected to additional analysis and alternative evaluation methods are proposed.

Chapter 5 **Material Analysis**
The novel leading edge coating systems are described and analysed. The relevant experimental work is elaborated upon and the material models used for subsequent analysis are calibrated.

Chapter 6 **RET Prediction and Validation**
The material's RET performance is computationally evaluated. Furthermore, the relavent experimental data is presented and used for validation of the RET lifetime prediction. The material systems are compared and relevant conclusions are drawn.

Chapter 7 **Conclusion and Recommendations**
The work conducted in this thesis is reflected upon and recommendations for future work are put forth.

CHAPTER 2
State of the Art

The following section deals with the state of the art of leading-edge erosion evaluation and provides relevant background information. It has been established that LEE is caused by impact with environmental particles such as rain, hail and sand particles, travelling with the wind. Capturing this phenomenon and predicting its occurrence is challenging since it is influenced by a great number of parameters such as the wind turbine operation and site conditions, as further discussed in section 2.1. The wind turbine blade structure and protection systems are discussed in section 2.2. Furthermore, section 2.3 provides a closer look into the modelling of typical leading edge protection solutions. Then, a more detailed look into erosion mechanisms and evaluation is provided in section 2.4. Finally, state-of-the-art experimental evaluation of LEP systems is discussed in section 2.5.

2.1 Wind Turbine Site Conditions

The operating conditions of a turbine are dictated by the site-specific wind conditions, determining operating parameters such as power production, blade pitching and rotational velocity. Knowledge of these parameters will provide insight into the impact cases an operating turbine will be subjected to throughout its lifetime.

2.1.1 Wind Turbine Operation

Wind turbine operation is determined by site-specific wind conditions. Wind is a random event, often captured by a Weibull probability density function [43]. This gives insight into the frequency of occurrence for different wind speeds. Directly related to this is the wind turbine rotational velocity. For wind speeds below the turbine's rated velocity, the turbine strives to operate at optimal tip speed ratio (TSR), optimising power production. For higher wind speeds, the rotational velocity is limited, limiting the power production by pitching the blades. Tip speeds are directly proportional to rotational velocity ($V_{tip} = \omega \cdot R$), with ω as rotational velocity in rad/s and R as turbine radius in m. When analysing impact cases on the blade, the blade's velocity component is the dominant contributor in the determination of impact speed. This implies that knowledge of turbine site-specific wind conditions will provide insight into the impact speeds of the blade with precipitation such as rain or hail.

2.1.2 Precipitation

Precipitation can take the form of rain, hail or snow. Of these rain is the most frequent, thereby having the largest erosion impact on operating wind turbine blades [42]. Site-

specific rain conditions can be captured by looking at the frequency of rain, rain intensity and droplet size [36]. Rain frequency can be described by 'wet periods' and periods of 'zero rainfall', making it a discrete process. This can be captured by analysing the percentage of time in which certain rain intensities occur [11]. Rain intensity on the other hand becomes a continuous process, assuming 'wet periods'. It captures the level of participation in terms of the amount of rainfall in a unit of time, usually classified in [mm/h]. Dependent on rain intensity, droplet size has been captured by the Marshall-Palmer function [31] for on-the-ground rain conditions. The rain conditions relevant to LEE occur at heights between 50-250m, depending on the turbine's hub height and blade length. Therefore, alternatives have been proposed, for example by Best [36], who describes the rain droplet size as a two-parameter Weibull distribution, dependent on rain intensity. Knowledge of site-specific rain conditions will allow for the assessment of loading conditions the wind turbine blade will be subjected. This is required when aiming for site-specific blade coating lifetime predictions.

2.2 Blade Structure and Protection

A wind turbine blade is shaped aerodynamically with a suction and pressure side, causing pressure differences over the blade. The loads associated with these aerodynamic forces, have to be carried by the blades over the full lifetime of the turbine. Below, a more detailed explanation is provided for the blade's main structural component. Furthermore, the most common leading edge protection solutions are further discussed.

2.2.1 Structural Components

Figure 2.1 shows a schematic of both the full blade and a typical cross-section along the blade. The pressure and suction side of the blade are joined at the contact points via the webs, making up the aerodynamic shell of the blade. This shell typically consists of a sandwich structure designed to withstand buckling. Loading of the blade can be divided into two main categories: flap- and edgewise loading. Flapwise loading, caused by pressure differences between the pressure and suction side, is taken up by the main spar and shear webs. Edgewise loading comes from gravitational and torque loading and is carried by the edges of the profile [32]. Finally, aeroelastic stability must be ensured for all operational conditions by ensuring sufficient structural stiffness combined with suitable control techniques.

Composite materials are widely used for the turbine blades, as a result of the high specific strength and stiffness that can be reached with this type of material. A common material found in wind turbine blades is glass fibre reinforced polymer (GFRP). For high blade lengths (>80 m), carbon fibre can be integrated into the composite lay-up improving the strength and stiffness properties of the blade [18]. .

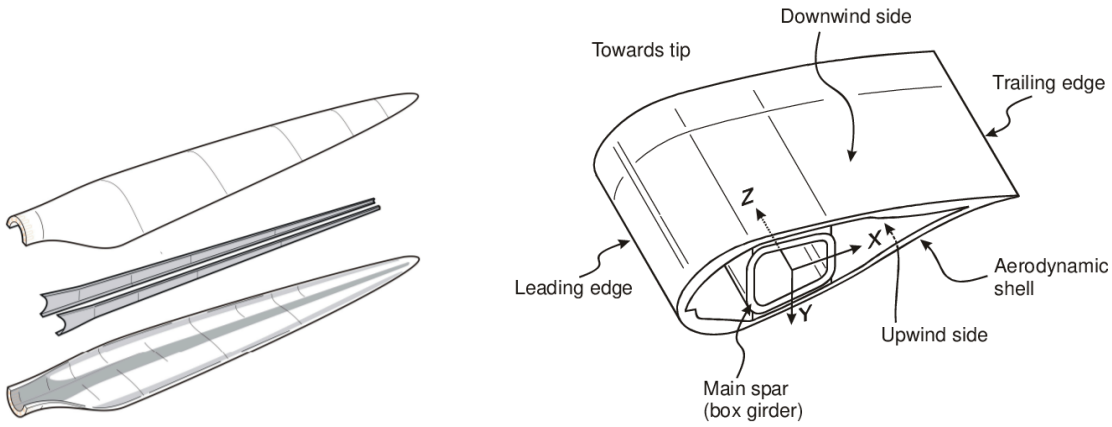

Figure 2.1: Schematic of wind turbine blade parts (left) and cross-section schematic of the wind turbine blade (right). From [40, 32].

2.2.2 Leading Edge Protection

Typically, a coating is applied to the leading edge of the blade, forming the main protection of the blade from environmental impact factors. This protects the structural, composite components of the blade which are prone to high maintenance costs. Different types of leading edge protection systems can be identified, as listed below [29].

(1) Gelcoats
These, often brittle, coating systems consist of thermoset polymer resin systems. In mould application is typically used for these polyester or epoxy-based systems. Due to this method of application, the material choice is limited to materials similar to the matrix of the composite structure, since the coating material and composite structure will be cured together during the production process.

(2) Polyurethane or Flexible coatings
These coating systems are widely used in industry due to their generally high impact resistance. It consists of multiple materials of which the composition can be altered to achieve the desired material properties. Application is possible via brush, roller or spray onto the turbine blade in the post-processing phase of production.

(3) Tapes
These flexible tapes can be applied to the blade in the post-processing phase. These tapes are often PU based, the main difference with the flexible coating comes from the application step (tape instead of spray application). [28]

(4) Erosion shield
Metallic erosion shields have been shown to provide excellent leading edge protection, greater than current operational wind turbine blade protection systems. The challenge lies in the stiffness mismatch between the shield and composite blade,

resulting in high shear forces under loading. These are to be taken up by the adhesive layer connecting the blade and shield, which has been proven to be insufficient to ensure the structural integrity of the blade, for the full turbine's lifetime. A solution for this mismatch in stiffness has not yet been found, meaning erosion shields are hardly used to combat leading edge erosion [21].

Of the above-listed protection systems, polyurethane coatings are the most common in industry today. It combines ease of application with good erosion resistance and thus becomes the most competitive solution [28]. A typical leading edge structure with a protective layer is shown in Figure 2.2. The laminate is covered with a putty filler layer and covered with the final protection layer, both with a thickness in the range of 0.5-1 mm.

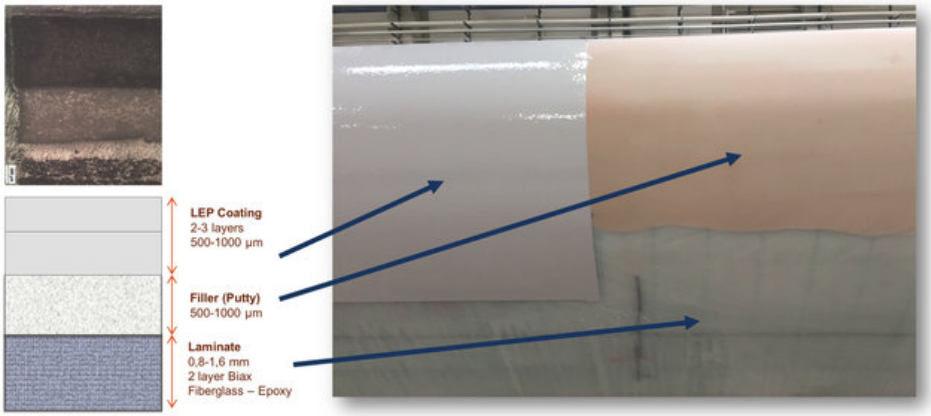

Figure 2.2: Typical leading edge structure with a protective coating. From [6].

2.3 Material Properties and Modelling

Since polyurethane coatings are found to be the most widely used materials for leading edge protection, an overview is provided on material characteristics and modelling techniques for this material type, exhibiting both visco- and hyperelastic behaviour.

2.3.1 Visco-elasticity

Visco-elastic materials are materials showing both viscous (liquid) and elastic (solid) behaviour when loaded. Its behaviour is both time and strain rate dependent. When loaded under constant stress, an initial elastic response is found. This then evolves into viscoelastic strain behaviour known as creep, exhibiting time dependant strain behaviour. When unloaded, a similar response is found. Instantaneous elastic spring back is seen followed by viscoelastic recovery. This behaviour is visualised in Figure 2.3.
Purely elastic materials can be modelled via Hooks law (Equation 2.1), while the viscous response can be modelled as a Newtonian fluid (Equation 2.2), with a linear relationship

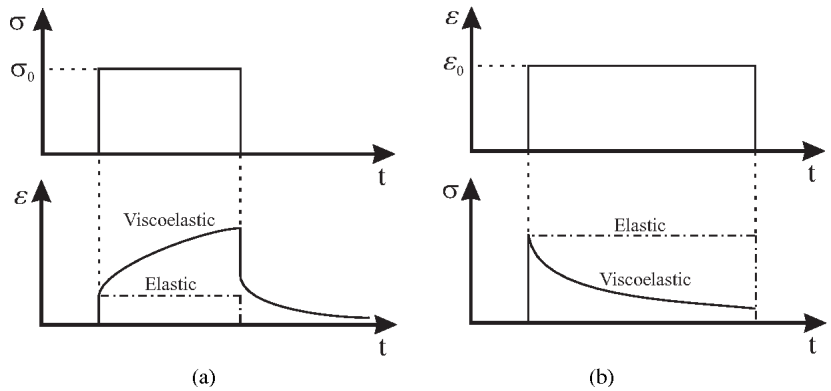

Figure 2.3: Visualisation of time-dependent stress-strain behaviour (creep) of visco-elastic material, for both constant stress (a) and constant strain (b). Adapted from [33].

between stress and strain rate. Modelling visco-elastic materials can be done via combining elastic solid material response and Newtonian liquid behaviour. An analogy with a spring and dash-pot system can be made. Different models have been proposed such as the Kevin-Voight, three-parameter solid model or Maxwell's model [26].

Maxwell's model captures this type of behaviour by placing a spring with stiffness E, in series with a dashpot with constant η [15], as visualised in Figure 2.4. When loaded under stress σ, an immediate elastic response is found, while the piston movement develops over time, capturing the time-dependent response of the material.

$$\sigma(t) = E\epsilon(t) \tag{2.1}$$

$$\sigma(t) = \eta\frac{\delta\epsilon}{\delta t} = \eta\dot{\epsilon} \tag{2.2}$$

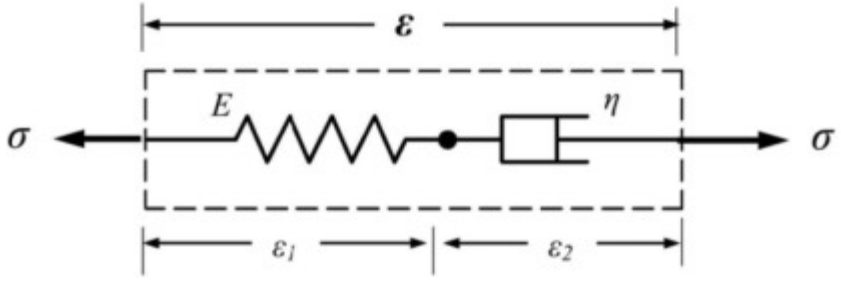

Figure 2.4: Schematic representation of Maxwell's spring-dashpot model for visco-elastic material response. From [45].

Since the spring and dash-pot are connected in series, the stress experienced by both will be equal. Furthermore, the total strain in the system can be found by adding both

strain contributions. Taking the time derivative provides the constitutive equation of the system:

$$\begin{aligned} \sigma + \frac{\eta}{E}\dot{\sigma} =& \eta\dot{\epsilon} \\ \tau =& \frac{\eta}{E} \end{aligned} \tag{2.3}$$

Here τ is introduced as the relaxation time. Solving this differential equation for a step strain condition at t=0 and initial condition $\sigma(0) = E\epsilon_0$, leaves the relaxation modulus:

$$E(t) = Ee^{\frac{-t}{\tau}} \tag{2.4}$$

Converting this in the frequency domain via Fourier transform, two contributions can be identified. The storage and loss modulus make up the complex modulus E*. The storage modulus is a measure of the material's in-phase (elastic) behaviour while the loss modulus represents the out-of-phase (viscous) behaviour. When loaded dynamically with radial frequency ω, the material storage and loss modulus can be captured in the frequency domain as follows:

$$\begin{aligned} E'(\omega) =& \frac{E\omega^2\tau^2}{1+\omega^2\tau^2} \\ E"(\omega) =& \frac{E\omega\tau}{1+\omega^2\tau^2} \end{aligned} \tag{2.5}$$

Maxwell's model can be extended to the generalised Maxwell's model. This model places n springs and dash-pots (Maxwell) elements in parallel with one free spring system. A schematic is shown in Figure 2.5. Adding infinite Maxwell elements allows the description of any system, increasing the model's accuracy as well as complexity.

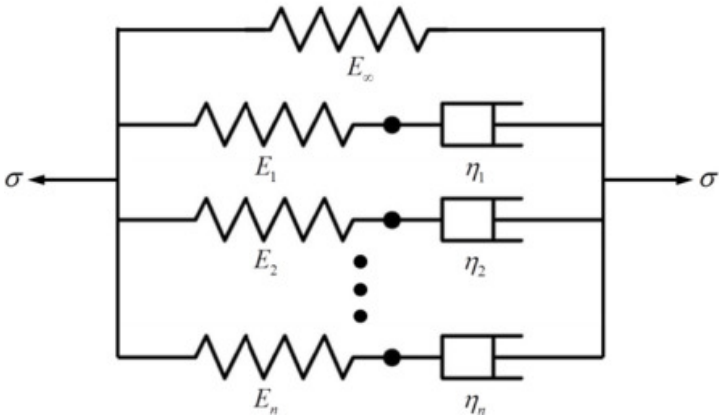

Figure 2.5: Generalised Maxwell model. From [45].

The stress-strain behaviour of this type model can now be captured as follows, where σ_∞ and ϵ_∞ are the stress and strain of the free spring respectively:

$$\begin{aligned} \sigma =& \sigma_\infty + \sum_{i=1}^{n} \sigma_i \\ \epsilon =& \epsilon_\infty = \epsilon_i \end{aligned} \tag{2.6}$$

Since the Maxwell elements are connected in parallel, their contributions can be added up. With E_∞ as the free springs stiffness and E_i, τ_i as the stiffness and relaxation time of the ith Maxwell element respectively, the relaxation modulus can be shown to equal:

$$E(t) = E_\infty + \sum_{i=1}^{N} E_n e^{\frac{-t}{\tau_n}} \tag{2.7}$$

Applying a Fourier transform to the relaxation modulus allows the storage and loss modulus of the system in the frequency domain to be determined as follows:

$$\begin{aligned} E'(\omega) =& E_\infty + \sum_{i=1}^{n} \frac{E_i \omega^2 \tau_i^2}{1 + \omega^2 \tau_i^2} \\ E"(\omega) =& \sum_{i=1}^{n} \frac{E_i \omega \tau_i}{1 + \omega^2 \tau_i^2} \end{aligned} \tag{2.8}$$

The same methodology holds for the shear relaxation modulus, given by Equation 2.9 as the sum of the equilibrium spring contribution and multiple Maxwell elements.

$$G(t) = G_\infty + \sum_{i=1}^{N} G_n e^{\frac{-t}{\tau_n}} \tag{2.9}$$

With G_0 as the sum of the instantaneous shear modulus of the equivalent spring and sum of the maxwell's elements, as shown Equation 2.10, and introducing g_i as $\frac{G_i}{G_0}$, the shear modulus can be written as

$$G_0 = G_\infty + \sum_{i=1}^{N} G_i \tag{2.10}$$

$$G(t) = G_0 \left(+ \sum_{i=1}^{N} g_i \right) + G_0 \sum_{i=1}^{N} g_i e^{\frac{-t}{\tau_n}} \tag{2.11}$$

The materials bulk modulus can be determined is a similar relation as shown in Equation 2.12. Here K_0 represents the instantaneous bulk modulus, while k_i is defined as $\frac{K_i}{K_0}$.

$$K(t) = K_0 \left(+ \sum_{i=1}^{N} k_i \right) + K_0 \sum_{i=1}^{N} k_i e^{\frac{-t}{\tau_n}} \tag{2.12}$$

Then, assuming isotropic materials, the instantaneous shear and bulk modulus are determined using the following relations, as a function of the material's instantaneous elastic moduli E_0 and ν_0.

$$G_0 = \frac{E_0}{2(1+\nu_0)} \tag{2.13}$$

$$K_0 = \frac{E_0}{3(1-2\nu_0)} \tag{2.14}$$

In ABAQUS, the visco-elastic material properties can be defined by approximating the above relations for shear and bulk modulus in the form of a Prony series.. Different combinations of g_i, k_i and τ_i can be determined via least-squares fit on experimental data.

2.3.2 Hyperelasticity

Hyper-elastic material exhibit a non-linear elastic response when subjected to loading. When unloaded, no energy dissipation occurs and the material goes back to its original state, as visualised in Figure 2.6. A linearly elastic stress-strain curve is shown for comparison.

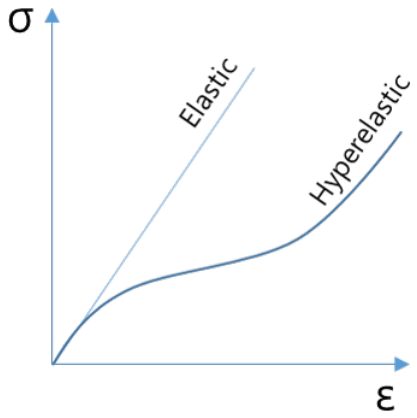

Figure 2.6: Linear elastic and hyperelastic response under loading. From [41].

This type of behaviour is found in elastics, rubbers, polymers and polyurethane leading-edge coating systems. Capturing this behaviour has proven to be challenging since linear elasticity as described in Hook's law is no longer valid for the full response behaviour. Alternatively, strain energy functions W, expressing the materials Helmholtz free energy, are used to capture the material's behaviour, as per Equation 2.15 [17].

$$W = f(I_1, I_2, I_3) \tag{2.15}$$

Here I_1, I_2 and I_3 represent the three invariant of the Cauchy-green deformation tensor and are defined as per Equation 2.16, with λ_1, λ_2 and λ_3 as the principle stress ratio's.

$$\begin{aligned} I_1 =& \lambda_1^2 + \lambda_2^2 + \lambda_3^2 \\ I_2 =& \lambda_1^2\lambda_2^2 + \lambda_2^2\lambda_3^2 + \lambda_3^2\lambda_1^2 \\ I_3 =& \lambda_1^2\lambda_2^2\lambda_3^2 \end{aligned} \tag{2.16}$$

Different models have been proposed that capture hyperelastic material behaviour, balancing model accuracy and complexity. These include the Neo-Hookean Mooney-Rivlin and Yeoh model [4]. Assuming incomprehensibility and independence of temperature, the Neo-Hookean model can be expressed as:

$$W(I_1) = \frac{\mu}{2}(I_1 - 3) \tag{2.17}$$

Here μ is the materials shear modulus. This model shows a linear response with I_1 and no dependence on invariant I_2. This might cause inaccuracies for larger strains, where a highly non-linear response is found. The strength of this model lies in the simplicity of implementation. Operating under the same assumptions as for Neo-Hookean, Mooney-Rovlin can be expressed as:

$$W(C_{10}, C_{01}) = C_{10}(I_1 - 3)C_{01}(I_2 - 3) \tag{2.18}$$

Here, linear dependence on I_2 is included, increasing the accuracy of the model. However, instabilities may be found for this model for negative C_{01}. The Yeoh model, shown in Equation 2.19, provides more stable results by including high order dependence on I_1. This allows for non-linear high strain response [4].

$$W(C_{10}, C_{20}, C_{30}) = C_{10}(I_1 - 3) + C_{20}(I_1 - 3)^2 + C_{30}(I_1 - 3)^3 \tag{2.19}$$

2.4 Erosion Evaluation

The largest contributor to leading edge erosion has been shown to be rain impact on the blade [42]. Erosion evaluation due to repeated rain impact is two-fold. A single impact case should be analysed, of which the results can be extended to capture the effect of repeated impact and the formation of erosion over time.

2.4.1 Single Droplet Impact

When a single droplet impacts a substance, the deceleration of the droplet causes a pressure wave in the liquid and solid surface. The pressure disturbs the stress equilibrium in the impact material and stress waves are formed and propagate through the material [5]. As visualised in Figure 2.7, the Rayleigh wave (moving along the surface of the impact material), the shear wave (moving in the transverse direction) and the compressive wave (moving in the longitudinal direction) can be identified. Failure can occur when the amplitude of these stress waves exceeds the material dynamical fracture strength.

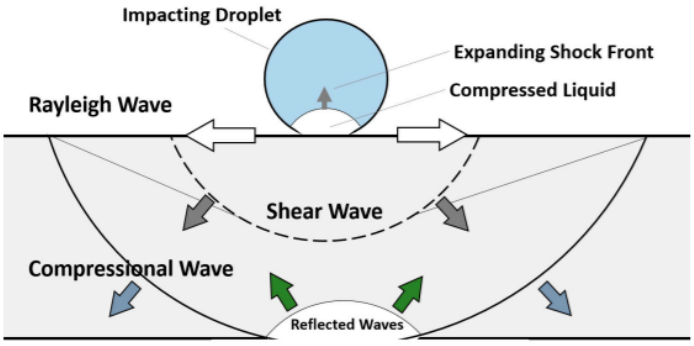

Figure 2.7: Stress waves following liquid droplet impact on a solid surface. From [14].

Furthermore, fatigue can be induced in the material following repeated impact [14].

The simplest expression for the pressure exerted on the impact material by the droplet can be expressed by the 'water hammer equation', as shown in Equation 2.20.

$$P_{hammer} = \rho_0 \cdot C_0 \cdot V_{impact} \tag{2.20}$$

Here, ρ_0 is the liquid density, C_0 equals the speed of sound in the liquid and V_i is the impact velocity. This equation has since been expanded and it was found that the maximum peak pressure was given as three times this value (Haymanns's approximation [22]) This peak pressure occurs just after impact when the lateral outflow of the liquid occurs. Furthermore, springer [39], included the pressure propagation in the droplet and solid impact material as captured by Equation 2.21:

$$P = \frac{Z_l V_{impact} cos\theta}{1 + \frac{Z_l}{Z_s}} \tag{2.21}$$

$$Z_i = \rho_i C_i \approx \sqrt{\rho E} \tag{2.22}$$

Here, Z_l and Z_s are the dynamic impedance of the liquid and solid respectively as defined in Equation 2.22 [13], v equals the impact speed and θ equals the impact angle. In Equation 2.22, ρ equals the material density, C the speed of sound in the material and E the material's modulus of elasticity. Several conclusions can be drawn from this equation. First of all, the impact pressure is maximised with perpendicular ($\theta = 0$) impact. Secondly, when the impedance of the solid is much greater than the impedance of the liquid ($Z_s >> Z_l$), the equation reduces down to the water hammer pressure equation, as proposed by Cook [5] Equation 2.20. Thus decreasing the impedance of the solid material, reduces the contact pressure experienced from liquid impact. Water at 20°C has an acoustic impedance of 1.48 MRayl while polyurethane has an impedance of 1.8 MRayl [35].

2.4.2 Erosion over time

Damage due to rain impact will most likely not induce failure after a single impact. It will accumulate over time following repeated impacts and repeated stress waves through the material. Initially proposed by Springer [39], this process has been shown to follow a set trend as visualised in Figure 2.8.

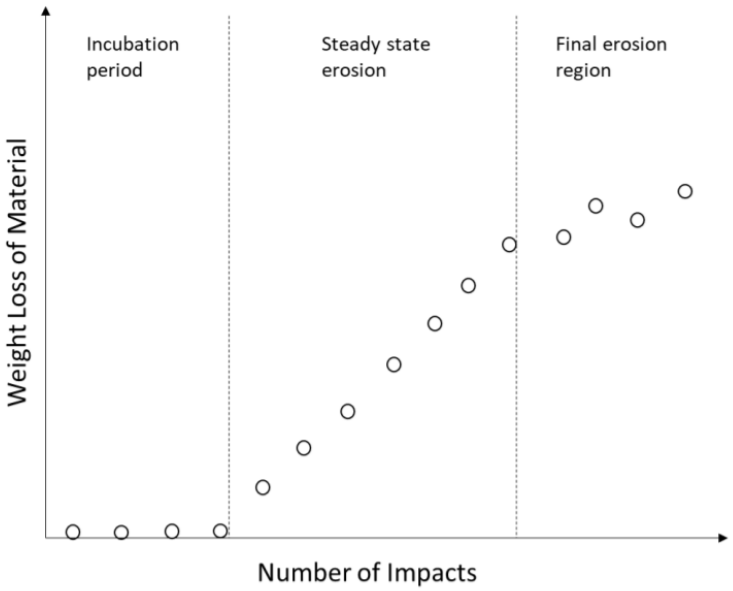

Figure 2.8: Erosion evaluation over time. From [23].

Three phases are identified; the incubation period, steady-state and final erosion regions. Analytic expressions have been formulated for quantifying the different erosion phases by Cook and further developed by Adler et al. [22, 39], however simplifying assumptions have been made in this analysis. Analysing droplet impact computationally allows for the mapping of stress histories of discrete locations within the impact material. This can subsequently be used for fatigue evaluation by applying stress history counting techniques such as rain-flow counting, level crossing, peak or range. Subsequently, Palmgren-Miner's rule can be applied to analyse the accumulated fatigue damage [44].

2.5 Rain Erosion Test (RET)

The state-of-the-art erosion evaluation method for novel coating materials consists of experimental determination of lifetime via rain erosion test (RET). The most common method of rain erosion testing is the whirling arm, in which a test specimen is rotated at high velocity through a generated rainfield. A typical RET whirling arm set-up is visualised in plot (a) of Figure 2.9. Three specimens are mounted on a rotating disc.

These specimens replicate a wind turbine leading edge, consisting of a glass fibre shell coated by the LEP. Since the specimen is rotated, a range of impact velocities can be evaluated in a single test. The rainfield is generated through a series of needle tips, which are used to control the mean rain droplet diameter of the rainfield. The limiting factor in large-scale whirling arm erosion testing is the high cost associated with the purchase and operation of whirling arm testers [27].

(a) RET whirling arm test set-up. From [1]

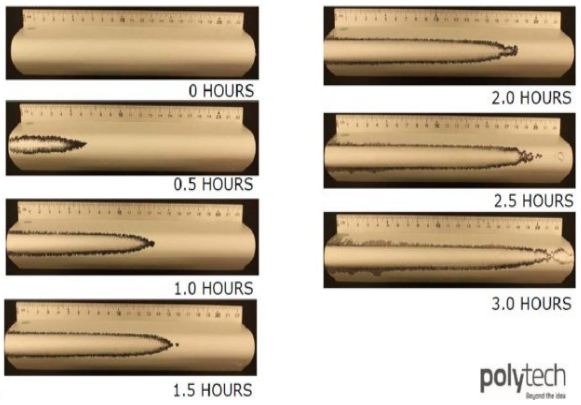

(b) RET whirling arm test progression. From [3]

Figure 2.9: RET whirling arm test set-up and typical damage progression.

The specimen is monitored at specific intervals, and the damage progression is assessed as visualised in (b) of Figure 2.9. The high-velocity side (left) of the specimen is shown to fail first and damage is seen to progress to the low-velocity side (right) of the specimen as the test progresses. Failure at these locations is recorded and a relation can be set up between impact velocity and time to failure of the coating system.

2.6 Conclusions

State-of-the-art evaluation of leading edge protection systems relies on expensive testing rain erosion testing campaigns. In order to suppress cost and evaluation time, computational evaluation is preferred. It can be stated that several evaluation methods for erosion due to liquid impact have been proposed and developed. However, due to the complexity of the phenomena, leading edge erosion and lifetime prediction of wind turbine blade protection remains an issue and further improvements in evaluation methods are required. Different leading-edge protective solutions can be investigated which aim to maximise lifetime and minimise losses associated with leading-edge erosion. Analytical models can provide rough estimations of coating lifetime however these rely on significant simplifying assumptions. Computational evaluation is therefore preferred, however, no method has yet been established that can predict lifetime to such an extent that it can be used for comparative predictions between protection systems.

CHAPTER 3

The DTU Wind Energy DURALEDGE Rain Erosion Framework

The work conducted in this thesis will be performed within the DTU Wind Energy DURALEDGE project. The focus of the work lies in the computational evaluation and numerical simulation of leading edge erosion. Here, the current state-of-the-art is described and elaborated upon.

An overview of the workflow is shown in Figure 3.1. The different steps in the workflow are identified and the tools required for the individual steps are presented. The input to the workflow consists of an experimental evaluation of the coating material under investigation. Raw DMTA frequency sweeps form the basis for the hyper and visco-elastic material models describing the material's behaviour upon impact. The material's impact fatigue performance is captured in an SN curve (Stress amplitude cycle- Number of occurrences to failure) based on Single Point Impact Fatigue Testing (SPIFT). Sections 3.1 and 3.2 provide further detail on the experimental evaluation techniques and material analysis, respectively.

The RE lifetime prediction requires the results of an explicit finite element simulation of a single liquid droplet impact for a specific droplet diameter and impact velocity. This simulation utilises pressure profiles obtained from a contact pressure model, solving for the pressure between a water droplet and a visco-elastic material. Further detail is provided in subsection 3.3.2. The simulation results are post-processed and form the basis for the rain erosion (RE) lifetime prediction. A rainfield is simulated and combined with the single droplet impact simulation results. Rain erosion test (RET) whirling arm conditions can be recreated and used as a means of validating the methodology of the RE lifetime prediction. This is further elaborated upon in subsection 3.3.3.

The workflow is discussed utilizing analysis of exemplary coating material. The material is a pure polyurethane, clear coating material and will be identified as PU269-4. This material is modelled as bulk material, assumed to have an infinite thickness in all finite element simulations. Furthermore, bulk material specimens are analysed in DMTA evaluation while SPIFT testing is performed on coated glass fibre reinforced polymer material specimens.

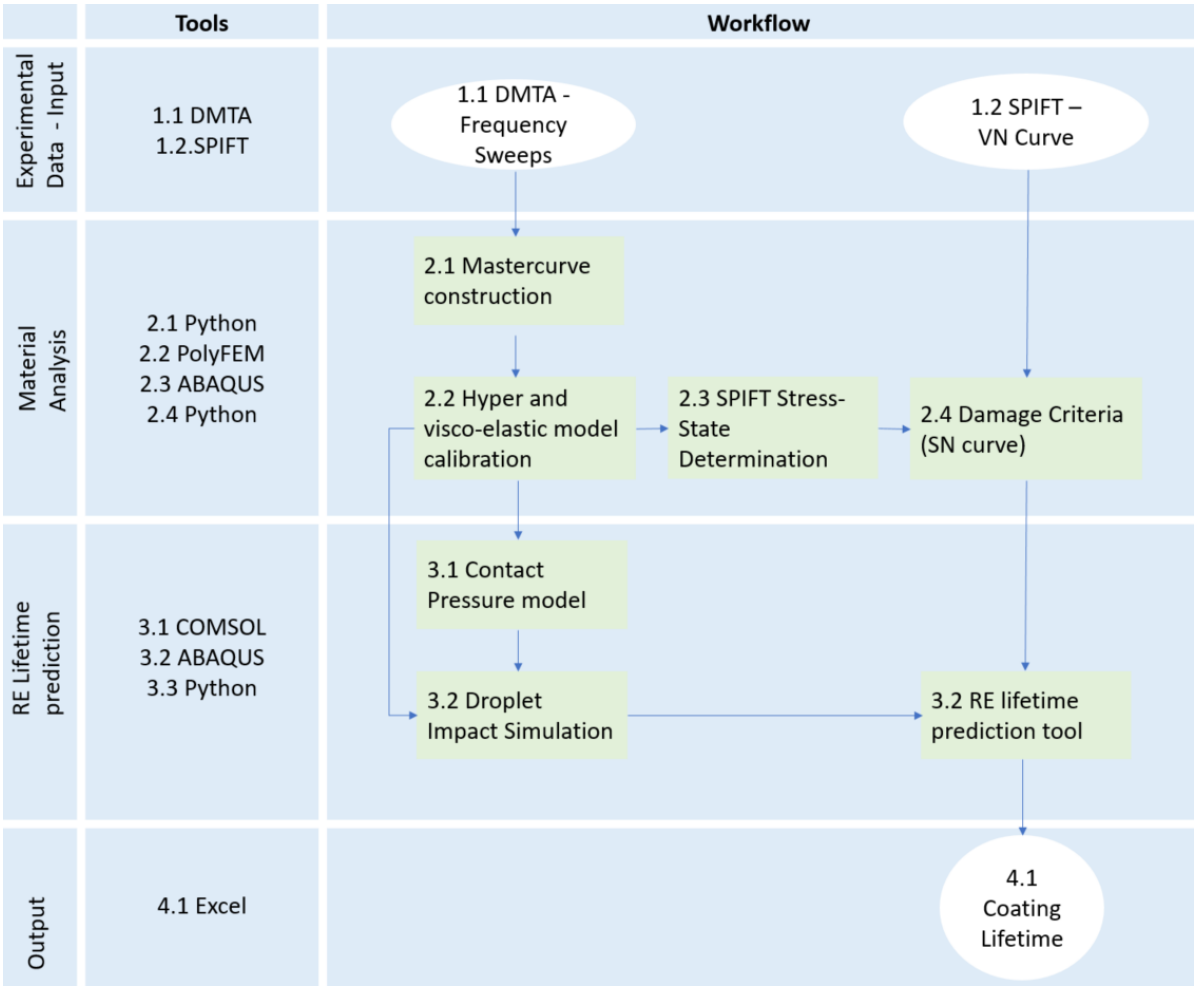

Figure 3.1: RE lifetime prediction workflow overview.

3.1 Experimental Data - Input

The input to the workflow consists of experimental evaluation of the coating material under investigation. The material's hyper and visco-elastic properties are determined using DMTA analysis. Then, SPIFT analysis provides the material's impact fatigue properties. Both are elaborated upon below.

3.1.1 Dynamic Mechanical Thermal Analysis (DMTA)

In DMTA, a dynamic, oscillatory load is applied to the material sample and its load-displacement behaviour is measured, as visualised in Figure 3.2. The load is applied under controlled load or controlled displacement conditions. In a linear visco-elastic response, a phase shift between the load and displacement is found.

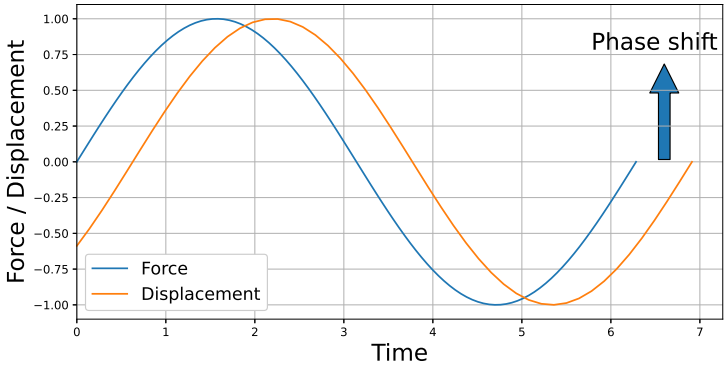

Figure 3.2: Force-displacement relation of material subjected to DMTA.

When a sinusoidal shear strain loading with frequency f is applied to the test specimen, the strain conditions of the specimen can be expressed as Equation 3.1. Here, γ_d is the applied strain amplitude and $\omega = 2\pi \cdot f$, equal to the applied radial frequency in rad/s. The measured stress amplitude can be shown to equal Equation 3.2. The complex modulus, G^*, relates the strain to a stress signal. A phase difference is seen between the stress and strain within the material, captured by the phase angle δ. With $\delta = 2\pi f \Delta t$, it shows the time delay (Δt) of the stress signal under strain loading or vise versa. Purely elastic materials will exhibit 0 phase shift, while purely viscous materials will show a phase shift of 90 degrees [45].

$$\gamma(t) = \gamma_d \sin \omega t \tag{3.1}$$

$$\tau(t) = \gamma_0 |G^*| \sin(\omega t + \delta) \tag{3.2}$$

Two components can be identified in the complex modulus, namely the storage (G') and loss (G") modulus, as per Equation 3.3.

$$\begin{aligned} G^* &= G' + iG\text{"} \text{ with:} \\ G' &= \frac{\tau_0}{\gamma_0} \cos \delta \\ G\text{"} &= \frac{\tau_o}{\gamma_0} \sin \delta \end{aligned} \tag{3.3}$$

The ratio between storage over loss modulus is known as the damping factor and defined as the tangent of the phase angle δ. It represents the relative amount of energy dissipation within the material upon loading.

$$\tan\delta = \frac{G'}{G\text{"}} \tag{3.4}$$

In this work, 3-point bending DMTA testing is performed for frequency range $[10^{-1}, 10^{3}]$ Hz and temperatures between -80 °C and 120 °C. The stress-strain behaviour under different frequency loading conditions is measured and converted to storage and loss modulus and damping ratio.

3.1.2 Single Point Impact Fatigue Tester (SPIFT)

The Single Point Impact Fatigue Tester (SPIFT) has been designed and developed by Nikolai Frønst-Jensen Johanson [27]. This test method provides a relatively low-cost analysis method for the evaluation of the impact behaviour of material systems. Schematically shown in Figure 3.4, SPIFT allows for high-speed impact fatigue testing, simulating the strain rates experienced by materials subjected to leading edge erosion. Nitrile rubber balls are shot at a test specimen at velocities up to approximately 175 m/s. Following repeated impact, damage is seen in the test specimen, captured by a digital high-speed camera. The temperature in the impact material is regulated by air cooling and monitored via infrared measurement. Further detail on the working mechanism of the SPIFT is provided below.

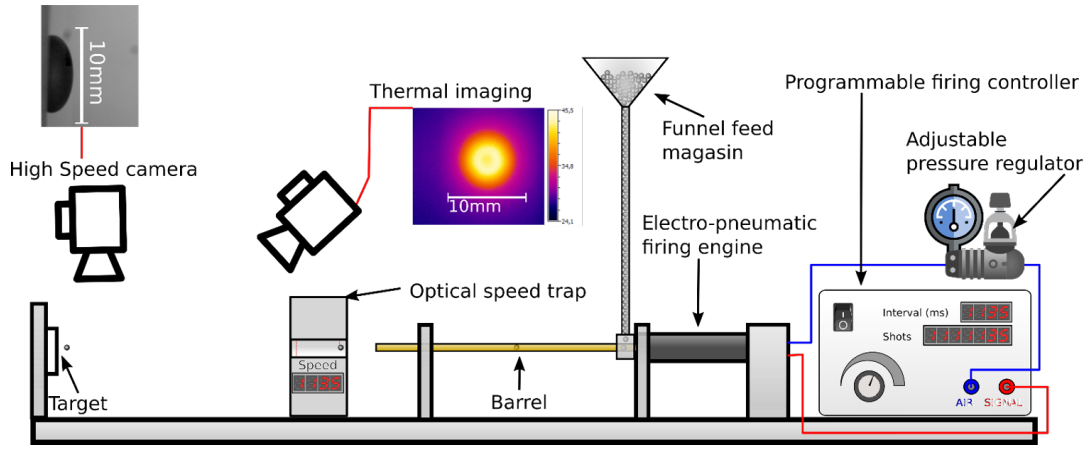

Figure 3.3: SPIFT schematic set-up. From [16].

Projectiles
For impact fatigue testing via SPIFT, nitrile rubber balls are shot at the test specimen. The balls have a diameter of 6 mm and a mass of 0.144 g. these projectiles are used since they exhibit visco-elastic deformation, similar to a liquid droplet impact.

Shooting mechanism
During SPIFT testing, the projectiles are fed through a gravity-fed vibrating funnel feed mechanism and loaded into the barrel. Here a Valkan V12 electro-pneumatic firing engine shoots the balls through an optical speed-trap (Airchrony Mk.3) onto the impact material. A range of shooting frequencies can be chosen with a maximum of 5Hz. The impact speed is regulated through air pressure in the pneumatic pump and speeds of 175 m/s can be reached. The speed trap can record 250 shots before requiring a reset.

Due to this limitation, the first 250 shots of each test at different levels of V_{impact} are recorded. From this raw data, misfires and re-bouncing ball measurements are filtered out by employing a minimum threshold of 80 % of the target velocity set on the raw data. From the remaining shot data, the mean and standard deviation are determined and assumed to be representative of the full test.

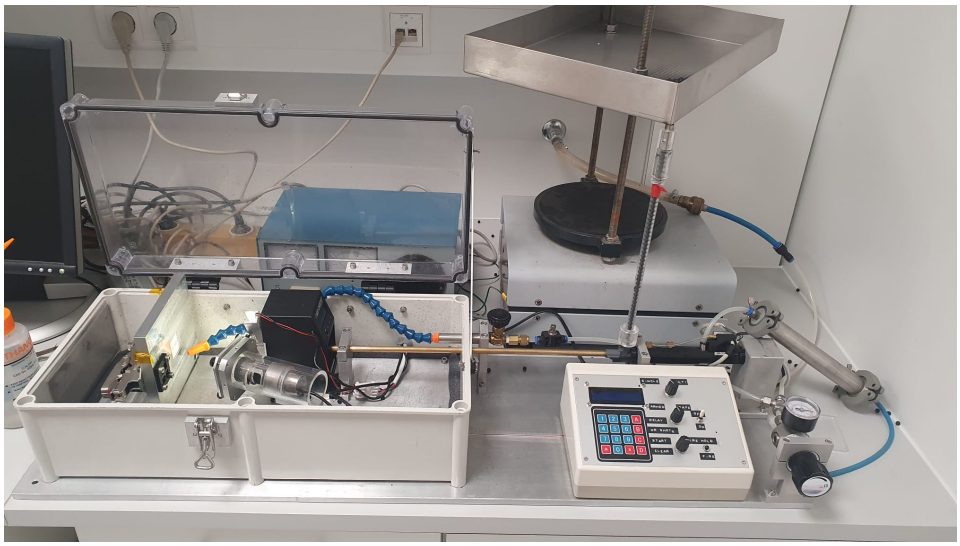

Figure 3.4: SPIFT shooting mechanism.

Damage detection
Damage detection during SPIFT testing relies on the recording of the surface of the test specimen by the high-resolution digital imaging AM7915MZTL from Dinolyte, operating at 3.1 Megapixel (2048 x 1534 @10 HZ). Visual inspection of the surface prior to impact testing is done to identify pre-existing defects in the test sample. These are to be excluded from damage detection since damage originating from these defects is not representable for the fatigue properties of the material.

Acoustic Emissions
An acoustic emission sensor is placed on the base of the SPIFT material specimen as shown in Figure 3.5. Mounting the AE sensor in this way allows for the comparison of the kinetic energy that is transferred from the rubber ball to the test specimen during SPIFT testing. Since the base is assumed to have a much greater mass than the test sample, the variation in the mass of the different test samples is assumed negligible. It must be noted that only a comparative analysis between different coating materials is possible since the kinetic energy in the base following impact is partly dissipated by the specimen base.

Infrared measurements
Part of the kinetic energy is converted into heat upon impact with the test specimen.

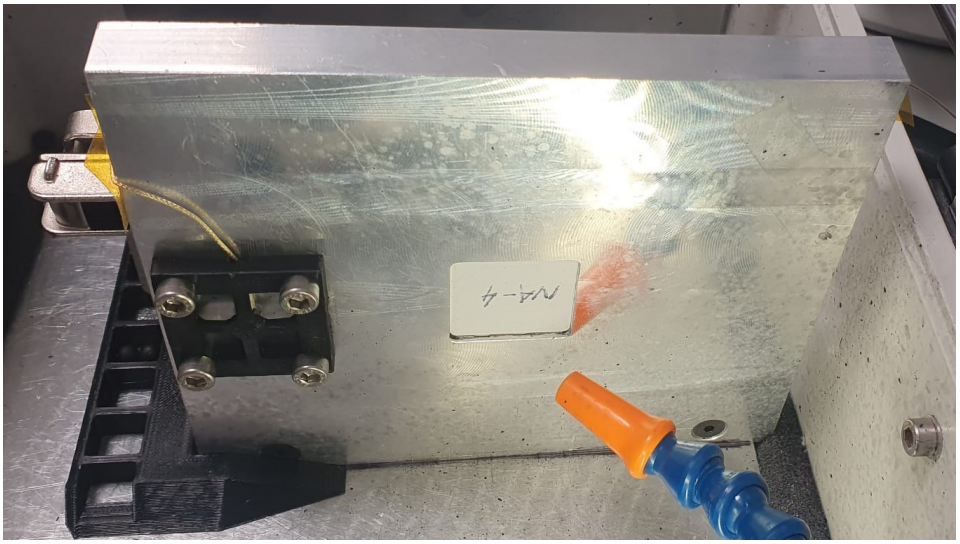

Figure 3.5: AE sensor mounted on the material sample base within the SPIFT set-up.

This generation of heat is monitored via infrared (IR) measurement of the impact surface of the test specimen. The test setup used for these measurements is visualised in Figure 5.6. The IR camera is slightly skewed with respect to the impact surface, due to space limitations within the SPIFT testing set-up. The IR camera used for measurements is the Optris Pi450, operating at 80 Hz with 0.1 °C resolution. A typical temperature profile as captured by the IR measurements is visualised in Figure 3.6, figure b. A doughnut-like temperature profile can be recognised following each impact case. From this temperature profile, the maximum value is extracted for further analysis.

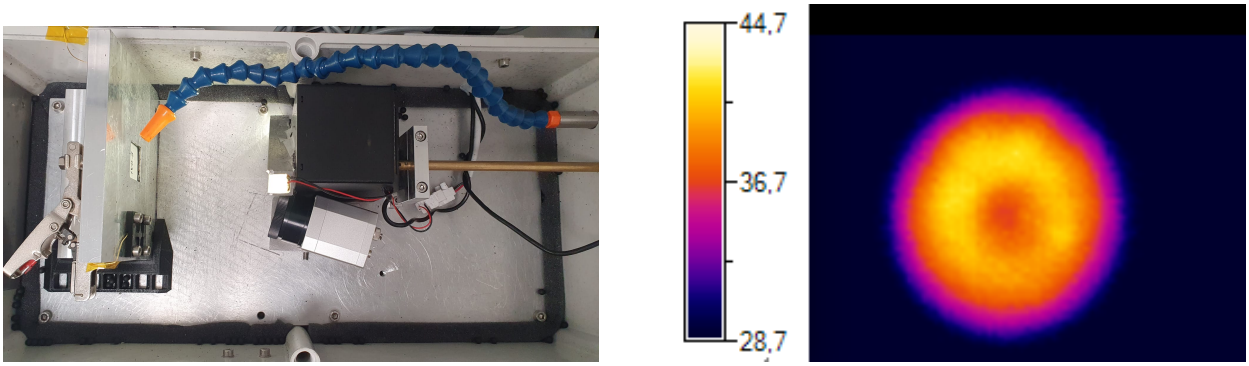

(a) IR measurement set-up

(b) Typical temperature profile following impact

Figure 3.6: SPIFT testing set-up for IR measurement of the test specimen surface (a), typical temperature profile following impact (b).

VN curve construction

Impact fatigue test performed at a range of impact velocities allows the construction of the materials V_{impact}- Number of impacts until incubation (VN) curve. For material PU269-4, this curve is visualised in Figure 3.7.

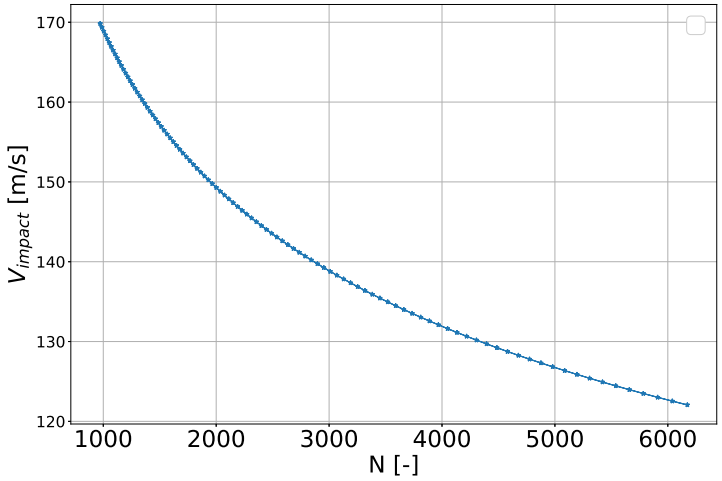

Figure 3.7: VN curve as obtained from SPIFT fatigue testing for coating material PU269-4.

3.2 Material Analysis

The experimental data is evaluated and processed in the subsequent step of the workflow. The raw DMTA data is converted into master curves, which form the basis of the hyper and visco-elastic material models used in subsequent finite element analysis. The VN curve obtained through SPIFT analysis is combined with the stress states experienced by the coating material during SPIFT testing, obtained through finite element simulation. This results in the damage criteria for the coating material expressed in a stress-based SN curve (Stress amplitude - Number of cycles until failure).

3.2.1 Master-curve construction

Following DMTA testing, the frequency sweeps for different temperature levels are combined according to the time-temperature superposition principle. This greatly increases the frequency range available in conventional DMTA testing, as required for modelling the liquid drop impact experienced by the WTB protective solutions. Impacts are observed to produce strain rates of above 10^5 Hz [27], well over the limit of the DMTA testing equipment of 10^3 Hz. Horizontal shifting is applied to the frequency sweeps of different temperature levels around one reference temperature [26]. Here, the shift factor a_T is determined via iterative process and visual inspection of the master curve. The reference

temperature frequency sweep is not shifted, leading to a_{Tref} =1. The generated master curve describes the material's viscoelastic parameters over a frequency range for $T = T_{ref}$.

Figure 3.8 shows the application of the time-temperature superposition and master curve construction for an example material system, for reference temperature T_{ref} = 20 °C. The frequency range of the DMTA testing has been expanded from [10^{-1}, 10^{3}] Hz from the original frequency sweeps, to [$10^{-}7$, 10^{7}] Hz for the final master curve.

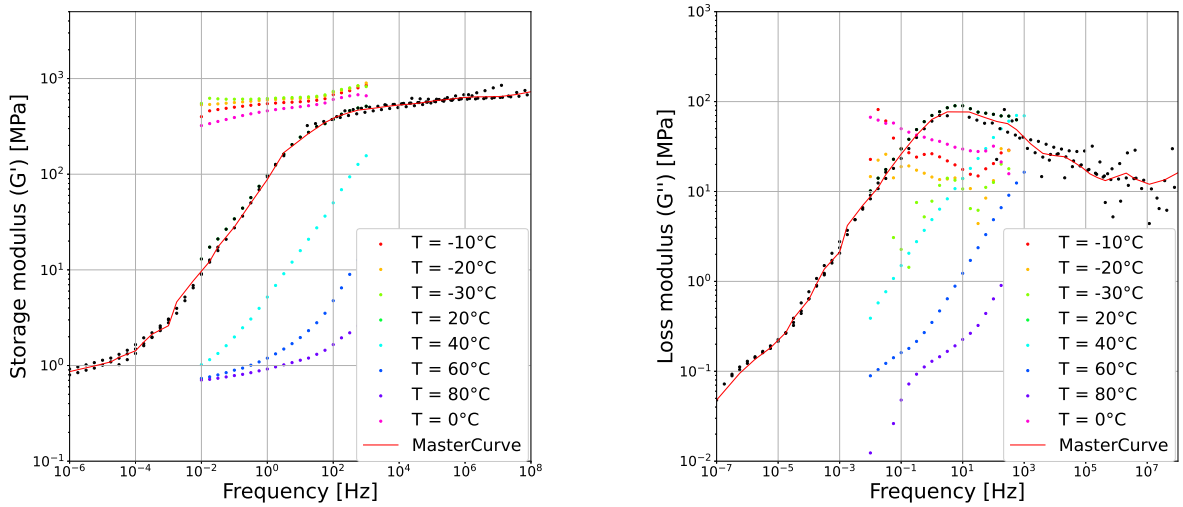

(a) Storage modulus (G')

(b) Loss modulus (G')

Figure 3.8: Master-curve construction of coating material PU269-4 before and after applying horizontal shifts to individual DMTA frequency sweeps.

3.2.2 Material Model Calibration

The master curves, as constructed with DMTA testing data, capture the material's behaviour when subjected to impact in the frequency domain for a given reference temperature. To model the material's response, hyper-and visco elastic material models need to be calibrated. The hyperelastic response is captured by Yeoh's hyperelastic material model while the visco-elastic response is modelled through prony-series expressing the generalised Maxwell's model.

The Yeoh hyperelastic model to be fitted is shown in Equation 2.19. Since DMTA testing is performed for simple shear loading conditions, the generalised maxwell prony parameters fit the shear loss and storage modulus. Converting the expressions for shear

relaxation modulus (Equation 2.11) into the frequency domain yields the pony series used for fitting the experimental master curve data [38]:

$$\begin{aligned} G'(\omega) =& G_0 \left(1 - \sum_{i=1}^{N} g_i\right) + G_0 \sum_{i=1}^{N} \frac{g_i \tau_i^2 \omega^2}{1 + \tau_i^2 \omega^2} \\ G''(\omega) =& G_0 \sum_{i=1}^{N} \frac{g_i \tau_i \omega}{1 + \tau_i^2 \omega^2} \end{aligned} \tag{3.5}$$

Calibration of the material models is done with MCCalibration by PolymerFEM [10]. For the Yeoh model, C_{10}, C_{20} and C_{30}, as well as D_1, D_2 and D_3 are calibrated while the number of prony parameters is determined from the master curve data and the respective parameters, τ_i and g_i, optimised. Calibration happens simultaneously for both models and the fit can be verified by means of the R^2 value. The experimental master curve for coating material PU269-4 is overlaid with the model fit in Figure 3.9. With the R^2 value of the fit close to 1 (0.997), the model is accepted. The corresponding prony parameters are shown in Table 3.1. The weights of the bulk moduli k_i, are set to the same values as the fitting values of the shear modulus g_i.

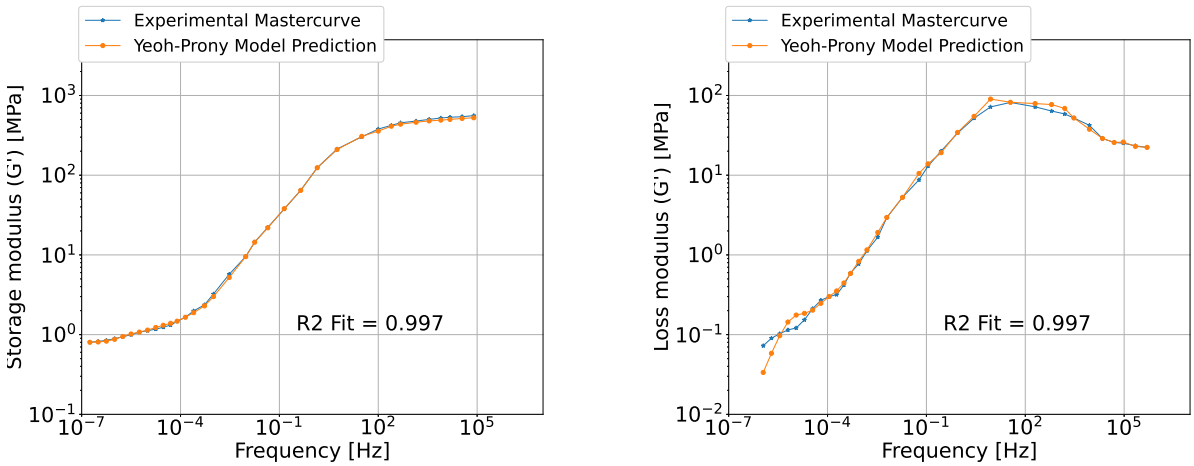

(a) Storage modulus (G')

(b) Loss modulus (G')

Figure 3.9: Material model calibration of coating material PU269-4 with Yeoh hyperelastic model and Prony series approximation to DMTA based master curve.

3.2.3 SPIFT Stress-State Determination

Combining the material's VN curve as obtained from SPIFT testing with the stress states in the coating material allows the construction of the material's stress-based SN curve. For this purpose, a 2D-axisymmetric Abaqus Explicit finite element model has

Table 3.1: Hyper-and Viscoelastic model parameters for coating material PU269-4.

Hyperelastic Model: Yeoh parameters					
	C10 [Mpa]	93.2	**D1** $[\frac{1}{Mpa}]$	0.011	
	C20 [Mpa]	0	**D2** $[\frac{1}{Mpa}]$	0	
	C30 [Mpa]	0	**D3** $[\frac{1}{Mpa}]$	0	
Viscoelastic Model: Prony Parameters					
i	g_i **[Pa]**	τ_i **[ms]**	i	g_i **[Pa]**	τ_i **[ms]**
1	0.001712	1000	**6**	0.23937	0.01
2	0.004797	100	**7**	0.254829	0.001
3	0.020311	10	**8**	0.0454107	0.0001
4	0.083832	1	**9**	0.101282	1.00E-05
5	0.230234	0.1	**10**	0.00930058	1.00E-06

been created, simulating SPIFT testing conditions of a rubber ball impact on a coating material [12]. The model geometry and boundary conditions are shown in Figure 3.10.

The model is set up with a general contact condition between the rubber ball and impact material, assuming no sliding. The bottom boundary of the impact material is constrained in the y-direction. The size of the target sample was set to 20x40 mm, deemed sufficient for mimicking an infinity large impact substrate. In the substrate, close to the surface, an element size of 0.01 mm is utilised, while a total of 1153 elements make up the rubber ball. This rubber ball is modelled as a visco-elastic material following methodology from section 3.2. The impact velocity of the rubber ball can be set as an input to the model and allows for the recreation of the full range of velocities available in SPIFT testing. Further details on the modelling of the rubber ball, mesh convergence, model validation and relevant model parameters can be found in [12].
The hyper- and viscoelastic material models (YEOH, prony) are determined as described in section 3.2 and imported into ABAQUS. The impact simulations are performed for a range of velocities. The stress field is extracted from which the maximum stress amplitude in time of the stress waves through the material is extracted in terms of the stress criteria listed below. Figure 3.11 visualises the results.

- VM: Von Mises
- SVM: Signed Von Mises
- AMPS: Absolute Maximum Principle Stress
- Max PS: Maximum Principle Stress
- Min PS: Minimum Principle Stress

The Von Mises stress criteria captures the full multi-axial fatigue stress state in a single value. However, Von Mises evaluation is not generally suitable for fatigue problems since it will always provide a positive stress state and therefore neglects any negative portion of

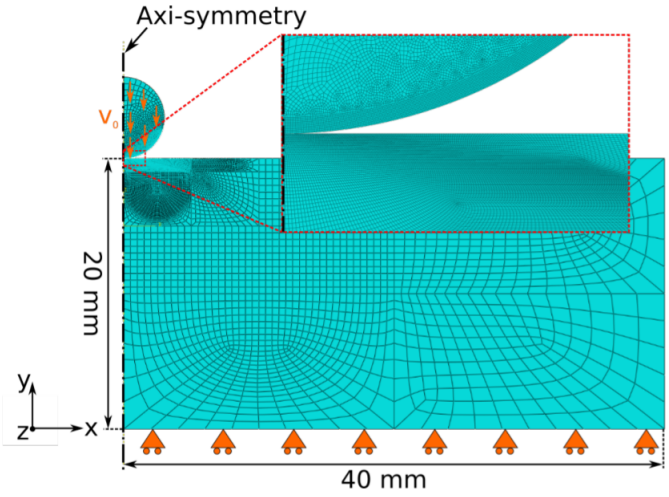

Figure 3.10: Model geometry and boundary conditions for simulating SPIFT testing conditions. The impact velocity is defined V_0, indicated on the ball just before impact [12].

the stress cycle. Signed Von Mises aims to resolve this issue by including the sign of the Absolute Maximum Principle stress to the Von Mises stress value. Principle stresses are more common in uni-axial fatigue problems however for multi-axial loading, the relevant fatigue stress range is not so easily determined.

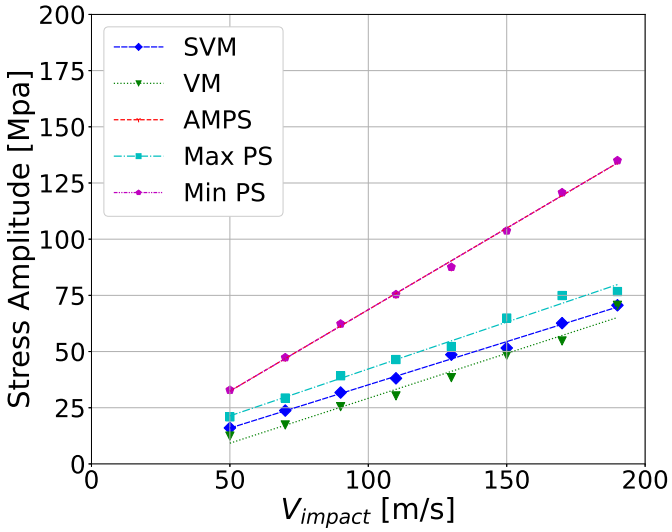

Figure 3.11: Maximum stress amplitude in time experienced by the testing specimen during SPIFT testing, as obtained from axi-symmetric FEM simulation for material PU269-4.

3.2.4 Damage Criteria - SN Curve

The results from the SPIFT testing (VN curve) and the result from the finite element simulation (σV curve), are combined to obtain the material SN curve. Equation 3.6 is fitted to the resulting curve, leading to parameters A and B, describing the impact of the material fatigue performance. This relation can be set up for different stress criteria for which the stress amplitude was extracted. The different SN curves for coating material PU269-4 are shown in Figure 3.12, with the curve parameters A and B for all stress criteria shown in Table 3.2

$$S_{max} = A \cdot \ln N + B \tag{3.6}$$

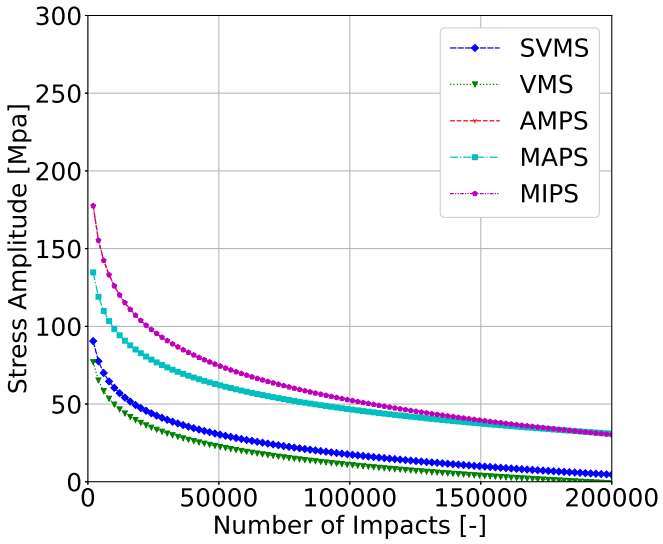

Figure 3.12: SN curve PU269-4 for stress criteria VM, SVM, AMPS, MAPS, MIPS.

Table 3.2: SN curve parameters PU269-4.

Stress Criteria	A [Mpa]	B [Mpa]
VM	-18.70	232.84
SVM	-16.95	205.93
AMPS	-32.04	421.41
MAPS	-22.57	306.47
MIPS	-32.04	421.41

3.3 Rain Erosion Lifetime Prediction

The final phase of the workflow consists of a single droplet impact simulation, of which the results are required by the rain erosion lifetime prediction tool. The simulation utilises pressure profiles representing the liquid impact event, obtained via a contact pressure model in COMSOL.

3.3.1 Contact Pressure Model

The contact pressure which represents the liquid droplet impact is obtained in collaboration with Nick Hoksbergen, PhD from Twente University (UT). It is based on a Multiphysics axisymmetric model in COMSOL, which solves for the contact pressure between a liquid droplet and a hyper- and viscoelastic material. A level-set method of multiphase flow and fluid-structure definition is used, with the right side of both the fluid and solid domain open. The thickness is such that reflections do not play a role.

The pressure profiles associated with the impact speeds defined in Table 3.3 are shown in Figure 3.13. The pressure profile can be seen to change over time, maximising at approximately t= $3 \cdot 10^{-6}$ s after the initial impact event. The pressure then spreads over the impact material while decreasing in magnitude. Higher impact velocities are associated with higher pressures for the full impact event, in line with expectations. Only pressures normal to the impact surface are included in the analysis. Shear forces acting on the roughness of the surface are not included. This simplification is accepted since the analysis focuses on finding the incubation period for the erosion event on the surface can be assumed to be smooth.

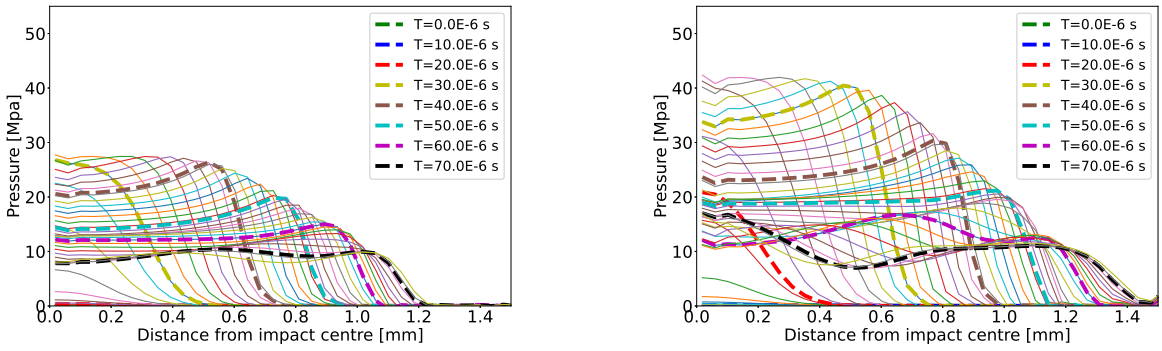

(a) V_{impact} = 100 m/s

(b) V_{impact} = 130 m/s

Figure 3.13: Pressure profiles for liquid droplet impact on coating material PU269-4 for impact velocities of 100- and 130 m/s.

3.3.2 Single Droplet Impact Simulation

A single droplet impact with a specified diameter is modelled using an ABAQUS explicit 2D axisymmetric FEM impact model. The hyper- and viscoelastic material models (YEOH, prony) are calibrated as described in section 3.2 and imported into ABAQUS. The target material is modelled as a rectangular 2.5x1 mm block, constrained in the y direction. The dimensions are chosen to assume infinite thickness and width and no noticeable effect of the bouncing of stress waves. The liquid droplet is represented by a contact pressure acting on the top surface of the material, as explained in subsection 3.3.1. The contact pressure induces stress fields in the impact material, which is extracted from discrete locations, varying in time. Through the depth of the material, several paths with equal spacing are defined. These paths follow the specimen along the x-direction, moving away from the centre of impact. All relevant simulation parameters are defined in Table 3.3, for coating material PU269-4.

Table 3.3: Droplet Impact simulation parameters PU269-4.

Parameter	**Unit**	**Value**
Material	[-]	PU269-4
Hyper-elastic model	[-]	Yeoh, as per Table 3.1
Visco-elastic model	[-]	Prony, as per Table 3.1
Density	$[\frac{kg}{m^3}]$	1100
Number of Paths	[-]	8
Depth Path N0. 1	[mm]	0.001
Path Spacing	[mm]	0.01
Path Length	[mm]	2.5
Simulation Time	[s]	5.00E-06
Sampling Interval	[s]	1.00E-07
Droplet Diameter	[mm]	2.36
Impact Velocity	[m/s]	100, 110, 120, 130

The results of the droplet impact simulations are extracted for the predefined paths along the impact material varying in-depth and in time. The results for coating material PU269-4 with simulation parameters as defined in Table 3.3, for $V_{impact} = 130$ m/s, are visualised in Figure 3.14. The signed Von Mises (SVM) stress state in the material for discrete points in time following impact initiation for discrete depths in the material. The stresses are seen to maximise at approximately t=$3 \cdot 10^{-6}$s, corresponding to the moment of maximum pressure. This occurs between 1 and 1.5 mm from the impact centre with the stress wave decreasing in magnitude when moving further from the impact centre. High-frequency fluctuations can be seen in the stress state which could be related to numerical noise as a result of the explicit finite element simulation.

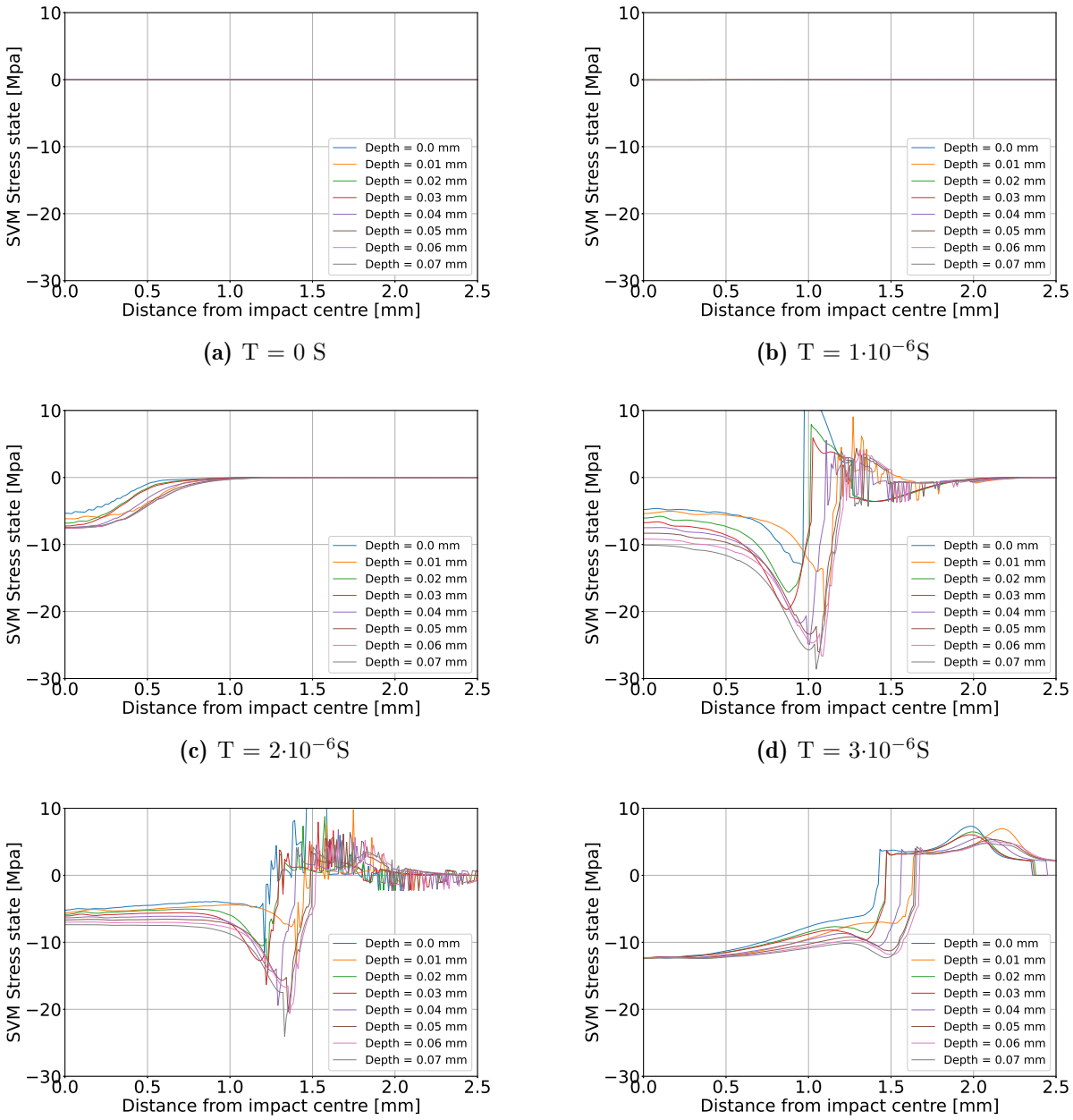

(a) T = 0 S

(b) T = $1{\cdot}10^{-6}$S

(c) T = $2{\cdot}10^{-6}$S

(d) T = $3{\cdot}10^{-6}$S

(e) T = $4{\cdot}10^{-6}$S

(f) T = $5{\cdot}10^{-6}$S

Figure 3.14: Signed Von Mises stress state in coating material PU269-4, following liquid droplet impact (d=2.36 mm) for impact velocity = 130 m/s for discrete points in time following impact initiation.

3.3.3 RE Lifetime Prediction

The final step in the framework simulates a rainfield and evaluates the coating materials' lifetime. The code can be used for evaluation of any rain erosion conditions, however, for validation purposes, RET whirling arm testing conditions are recreated. The RET lifetime is predicted for discrete impact velocities. This can then be compared with RET whirling arm test data. Figure 3.15 shows a schematic of the RE lifetime prediction code, tuned towards RET whirling arm conditions. Four main calculation blocks are identified, and further elaborated upon below.

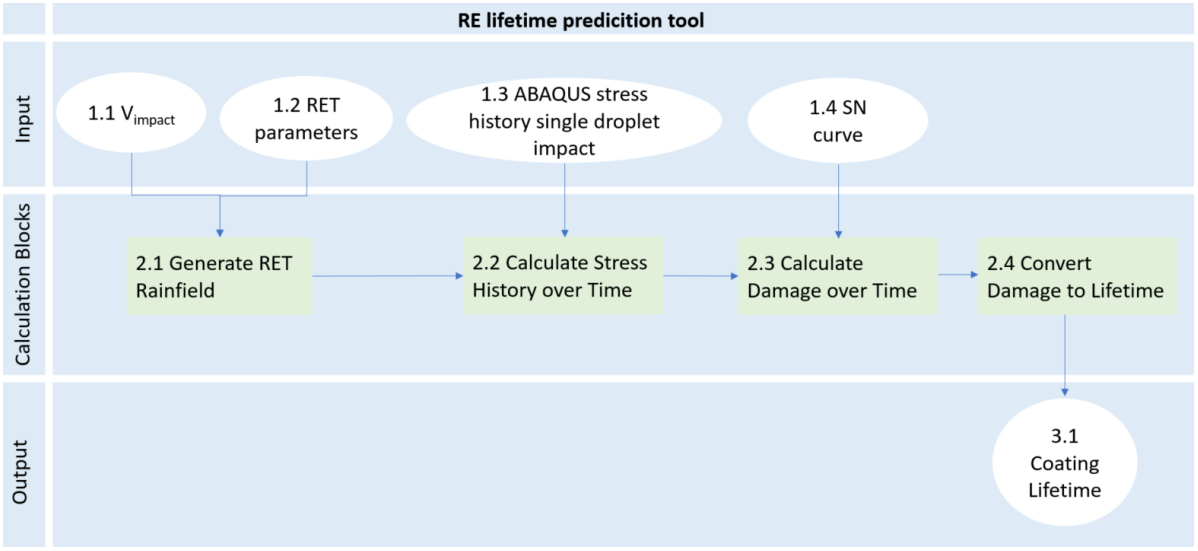

Figure 3.15: RE lifetime prediction code overview.

Generate RET rainfield
RET whirling arm testing conditions are simulated via the generation of a random rainfield. The RET rain intensity I, droplet diameter d, and impact velocity are set to recreate testing conditions. Furthermore, a simulation time t_{sim} is chosen of which the results can be extrapolated to a full damage prediction. The volume concentration, ψ, of the rainfield is then determined via Equation 3.7, with I in $\frac{m}{s}$ and v_{drop} equal to the free-falling droplet velocity at the rotor plane is $\frac{m}{s}$ [27].

$$\psi = \frac{I}{v_{drop}} \tag{3.7}$$

Dividing the volumetric concentration with the single droplet volume gives the droplet concentration q.

$$q = \frac{\psi}{V_{drop}} \tag{3.8}$$

By setting square evaluation surface with lengths L, the number of droplets can be determined as:

$$N_{drop} = q \cdot L^2 \cdot v_{\text{drop}} \cdot t_{\text{sim}} \tag{3.9}$$

The total number of droplets is calculated and equally distributed over 3D space. The XY plane is set by the evaluation area L^2 and the z position of the droplets so the impact events are equally spaced within the simulation time. Since the rainfield is a randomly generated input to the damage model, multiple runs with sufficient simulation time are required to come to a converged lifetime prediction.

Calculate Stress History
The RET rainfield causes impact cases on the investigative surface of the coating material. Stress waves propagate through the material following each impact. A single point on the surface is analysed and a droplet impact is assumed to affect this point when within the effective range of a droplet impact. The single droplet impact simulation as described in subsection 3.3.2 describes a single impact event and forms the basis for the stress history mapping. If a droplet is found to influence the point of investigation, the stress state [S_{11}, S_{22}, S_{33}, S_{12}] in cylindrical coordinates, over the full impact event in time is extracted from the single droplet impact simulation at the distance from the impact event. This stress state is converted to Cartesian coordinates so the Cauchy stress tensor can be set up as Equation 3.10. The stress state is extracted for discrete locations through the thickness of the material.

$$S_{ij} = \begin{bmatrix} S_{xx} & S_{xy} & S_{xz} \\ S_{xy} & S_{yy} & S_{yz} \\ S_{xz} & S_{yz} & S_{zz} \end{bmatrix} \tag{3.10}$$

The principle stress states of the system can now be determined by eigenvalue analysis of the stress state, as shown in Equation 3.11. Here, n_i represents the eigenvectors of the system while λ captures the eigenvalues. From this analysis, the maximum (MAPS), minimum (MIPS) and absolute maximum (AMPS) principal stresses can be extracted.

$$\begin{bmatrix} S_{xx} & S_{xy} & S_{xz} \\ S_{xy} & S_{yy} & S_{yz} \\ S_{xz} & S_{yz} & S_{zz} \end{bmatrix} \begin{bmatrix} n_1 \\ n_2 \\ n_2 \end{bmatrix} = \lambda \begin{bmatrix} n_1 \\ n_2 \\ n_2 \end{bmatrix} \tag{3.11}$$

Furthermore, the Von Mises (VM) stress is calculated as per Equation 3.12

$$\sigma_{vm} = \frac{1}{\sqrt{2}}[(S_{xx} - S_{yy})^2 + (S_{yy} + S_{zz})^2 + (S_{zz} - S_{xx})^2 + 6(S_{xy}^2 + S_{xy}^2 + S_{xy}^2)]^{\frac{1}{2}} \tag{3.12}$$

Adding the sign of the AMPS to the Von Mises stress results in the Signed Von Mises (SVM) stress criterion, leading to a total of five stress criteria for which the full stress history due to exposure to the simulated RET rain field is known, for discrete depths through the material. These individual criteria can be selected for the determination of damage in the material in the subsequent step.

Calculate Damage over Time
The repeated droplet impacts on the coating material cause fatigue and damage accumulates over time. Rainflow counting is applied to the stress history found in the material, converting the stress history over time into equivalent stress amplitude loading's S_i with the number of occurrences n_i. The total number of unique stress amplitudes found in the stress history is set to equal m. Miner's rule is applied to calculate the partial damage caused by the simulated rainfield as defined in Equation 3.13. Failure occurs when D_{total} = 1 in one of the paths throughout the thickness. Here, D_i represents the partial damage caused by the individual equivalent stress amplitude and N_i represents the maximum number of cycles until failure for the respective loading amplitude. This is determined by the materials SN curve and is calculated as per Equation 3.14

$$D_{total} = \sum D_i = \sum_{i=1}^{i=m} \frac{n_i}{N_i} \tag{3.13}$$

$$N_i = e^{\frac{S_i - B}{A}} \tag{3.14}$$

The damage calculation is done for the full length of the rainfield simulation t_{sim}. The damage parameter is then linearly extrapolated to D =1 and the lifetime in seconds can be extracted.

Damage to Lifetime
The final step in the lifetime prediction converts the estimated lifetime for the coating material from the time subjected to the simulated RET rainfield, to the number of impacts per m^2 and specific impacts. This allows comparison between RET testing set-ups under differential conditions. The number of impacts subjected to the test specimen per m^2 can be defined as Equation 3.15, with v_{drop} as the impact velocity of the droplet on the specimen.

$$N = q \cdot v_{drop} \cdot t_{test} \tag{3.15}$$

However, when using this measure, a problem arises when considering an infinitely small area. The number of droplets until failure becomes infinitely small. The area of a single droplet impact should be considered and for this reason, the specific number of impacts N_0 is defined. Firstly, the total impingement due to the simulated rainfield is calculated as:

$$H = \frac{V_{water}}{L^2} \tag{3.16}$$

Here, V_{water} equals the total volume of all the water in the rainfield and L^2 represents the evaluation surface area. The total impingement is then divided by the height of a projected cylinder with equal volume to a single droplet, h, as below. Here d represents the single droplet diameter.

$$N_0 = \frac{H}{h} = \frac{H}{\frac{2d}{3}} \tag{3.17}$$

3.4 Results

Coating material PU269-4 is analysed by the RET lifetime prediction tool according to the input parameters as per Table 3.4. The simulation time represents the length of a single simulation. Since the rainfield is distributed over 3D space, a certain uncertainty is introduced. Multiple runs are required to account for this uncertainty, as defined by the number of runs variable. The final result for each impact velocity is taken as the mean of the individual results for each run.

Table 3.4: Input parameters for the RET lifetime prediction tool for coating material PU269-4.

Parameter	Symbol	Unit	Value
Impact Velocity	V_{impact}	[m/s]	100, 110, 120, 130
Simulation Time	t_{sim}	[s]	1000
Number of runs	N_r	[-]	3
Droplet diameter	d	[mm]	2.4
RET intensity	I	[mm/h]	30
Droplet free-fall velocity	v_{drop}	[m/s]	2.5
Damage Criterion	DC	[-]	SVM, VM, AMPS, MAPS, MIPS

The results of the RET lifetime workflow are visualised in Figure 3.16, in terms of specific impacts until failure (N_0) vs impact velocity (V_{impact}). RET validation data is plotted in the same figure as the validation of the prediction. It can be concluded that the RET lifetime prediction is in the same order of magnitude as the validation data. The flaw in the prediction lies in its dependence on velocity. The prediction is showing a substantially lower dependence on impact velocity than the validation data. A positive slope can be recognised which would indicate improved material performance with higher impact velocities. This is a non-physical result since higher impact velocities are associated with higher stresses in the coating material. This implies the current workflow does not accurately capture the effects of varying impact speed on the lifetime of the coating.

The lifetime prediction has been performed for several stress criteria. It can be seen that the Von Mises and Signed Von Mises criteria provide results closest to the validation data. However, it must be noted that the prediction provides non-physical results (negative velocity dependence). Therefore, no conclusive statements can be made on what criteria are most suited for this multi-axial fatigue analysis. Further investigations on the workflow will be performed utilising the Signed Von Mises stress criteria since it captured the full multi-axial stress state of the material.

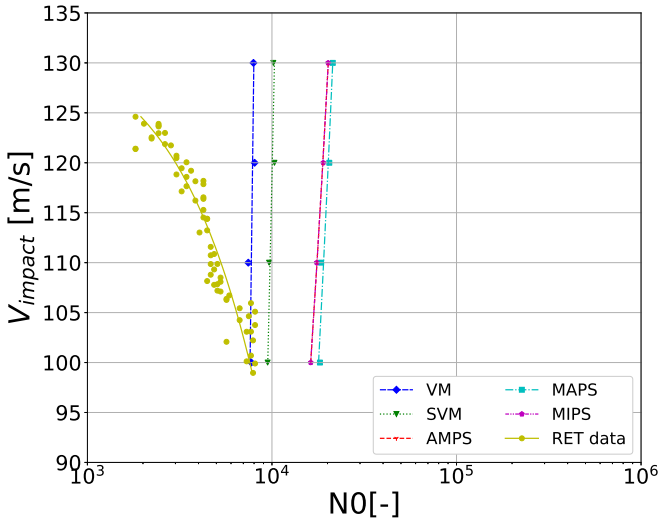

Figure 3.16: RET lifetime prediction results in terms of V_{impact} vs Specific impacts N_0 for coating material PU269-4. Overlaid with validation with RET data .

3.5 Conclusions

This chapter provides the benchmark overview of the DURALEDGE computational workflow for rain erosion. The main issue of the lifetime prediction lies in the underestimation of the velocity dependence of the coating lifetime, with respect to droplet impact velocity. Subsequent analysis of the methodology aims to resolve this issue and improve the accuracy of the material analysis and lifetime predictive capabilities of the workflow. Any subsequent analysis of novel coating materials will be based on the working mechanisms presented in this chapter.

CHAPTER 4
Methodology Evaluation

The RE lifetime prediction workflow as presented in chapter 3 represents the state-of-the-art of the RE lifetime prediction. Here, the different stages of evaluation are further discussed and reflected upon. Analysis and improvements on the workflow are presented. The material modelling and master curve construction is discussed in section 4.1. This is followed by an analysis of the methodology RE lifetime prediction tool in section 4.2. Finally, alternative evaluation methods for this tool are proposed and evaluated, as presented in section 4.3

4.1 Material Analysis

The material analysis part of the workflow is described in section 3.2 and covers the processing of DMTA data, master curve construction and hyper- and viscoelastic material model calibration. The state-of-the-art master curve construction relies on a trial and error procedure for determination of the shift factors for the construction of the final curve. This method is prone to error since no strict requirement is set on the fit of the final curve. To this end, master curve construction of the raw DMTA data has been updated to reduce this error. An algorithm has been created, automating the calculation of shifting factors for different temperature level frequency sweeps. For adjacent frequency sweeps, the shift factor is determined according to Equation 4.1 for the full overlap area. This is averaged over the overlap area to come to the final shift factor for the respective temperature frequency sweep. a_T represents the shift factor of the frequency sweep from temperate T_i, while ω_{Ti+1} and ω_{Ti} represent the frequency at which equal storage modulus is found for respective temperature levels T_{i+1} and T_i.

$$a_T = \frac{\omega_{Ti+1}}{\omega_{T_i}} \tag{4.1}$$

The shift factors apply to all visco-elastic properties of the materials and can be seen as a basic material property and can therefore be used for further material comparison. Different types of fit can be applied to the obtained shift factors, allowing comparison between materials and extrapolation to extreme temperature values. The William Landel Ferry equation (shown in Equation 4.2) can be fitted, for temperatures above glass transition (T_g) while the Arrhenius model is used below T_g. a_T represents the shift factor of temperature level T, T_{ref} represents the reference temperature at which the master curve has been constructed and C1 (in [C]) and C2 (dimensionless) are WLF equation parameters, determined via least square fit on the master curve . For the Arrhenius model, T and T_{ref} are expressed in [K], R represents the gas constant (R =

8.314 [J/mol/K]) and H the activation energy in [J/m], which is found via least squares fit on the master curve.

$$\log_{10}(a_T) = \frac{C_1 \cdot (T - T_{ref})}{C_2 + (T - T_{ref})}, T > T_g \tag{4.2}$$

$$\log_{10}(a_t) = \frac{-H}{2.303 \cdot R}\left(\frac{1}{T} - \frac{1}{T_{ref}}\right), T < T_g \tag{4.3}$$

Figure 4.1 visualises the shift factors applied to the respective frequency sweeps for the construction of the master curve of coating material PU269-4. The WLF and Arrhenius fit are shown for temperatures above and below T_g respectively. The glass transition temperature is obtained from 1 Hz DMTA experimental data as the peak of the tan δ curve over temperature. All relevant material data for material PU269-4 is summarised in Table 4.1

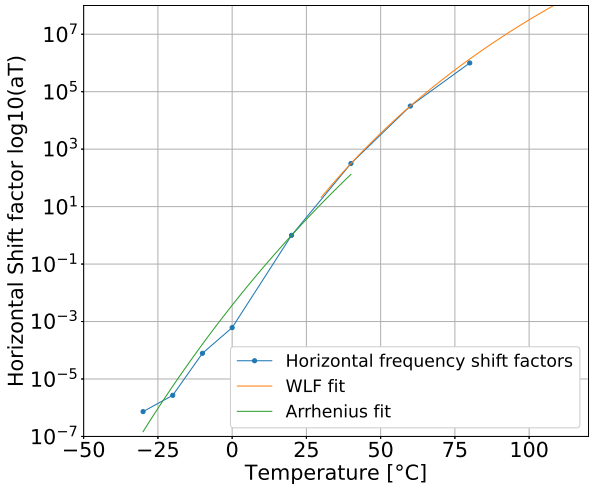

Figure 4.1: Horizontal shift factor applied to respective temperatures frequency sweeps including WLH and Arrhenius model fit for coating material PU269-4.

Table 4.1: Coating material PU269-4 shifting factor parameters and relevant temperature values. .

Material	C_1[C]	C_2[-]	**H** [kJ/Mol]	T_{g1Hz}^{DMA} [°C]
PU 269-4	22.5	160	-186524	40

The reference temperature around which the master curve is constructed has been found to affect the final curve. Higher reference temperatures are associated with the peak in the loss factor shifting to higher frequencies, indicating maximum energy dissipation in the material at a higher loading frequency. This becomes important when conducting SPIFT and RET experimental work and comparing these results with material models

calibrated at a certain reference temperature. The experimental and numerical evaluation should be conducted at similar temperature levels. Finally, it can be noted that increasing or decreasing the temperature of the material beyond the glass transition region, means its behaviour becomes increasingly unpredictable. The scatter in DMTA data is increased for these temperature frequency sweeps, increasing uncertainty in this region of the master curve .

4.2 RE Lifetime Prediction

The current state of the RE lifetime prediction tool does not capture the influence of impact speed on RET lifetime as seen in the RET test validation data. For this reason, the current state-of-the-art of the rain erosion tool workflow as described in subsection 3.3.3, is subjected to further analysis. The focus here lies on the effects of the single droplet impact simulation on the final lifetime prediction. Unless stated, the simulation parameters as in Table 3.3 and Table 3.4 are used for the liquid droplet impact model and RET lifetime prediction tool, respectively.

Firstly, the benchmark evaluation method, described in subsection 3.3.3 is subjected to further investigation aimed to discover the origin of the negative velocity dependence of the lifetime prediction. Then, two alternative evaluation methods are proposed and analysed which aim to improve this issue.

4.2.1 Benchmark case - Full Stress History

The benchmark RET lifetime evaluation as described in subsection 3.3.3 relies on the full stress history following liquid impact as obtained by the 2D-axisymmetric ABAQUS Explicit impact model, described in subsection 3.3.2. This means every time step extracted from the simulation is considered in the damage calculation. The total number of time steps extracted from the simulation is determined by the simulation time and sampling interval of the stress field. Furthermore, the stress states are only extracted for pre-defined paths along the coating material. The effect of these parameters is investigated.

Path Definition
The path definition defines the depth at which data is extracted from the simulation. A sufficient number of paths is to be chosen to that the full effect of the stress wave is captured in the analysis. The path number is increased from 8 to 50 while keeping the path spacing constant. Figure 4.2 visualises the result in terms of the SVM stress state within the coating material for discrete points in time, varying in depth of the coating material. The stress wave amplitude is shown to maximise between $3{\cdot}10^{-6}$ and $4{\cdot}10^{-6}$s following impact initiation, at a distance of 1 mm from the impact centre, similar to the droplet radius. Finally, it must be noted that throughout the thickness, high frequency and low amplitude stress fluctuations can be seen.

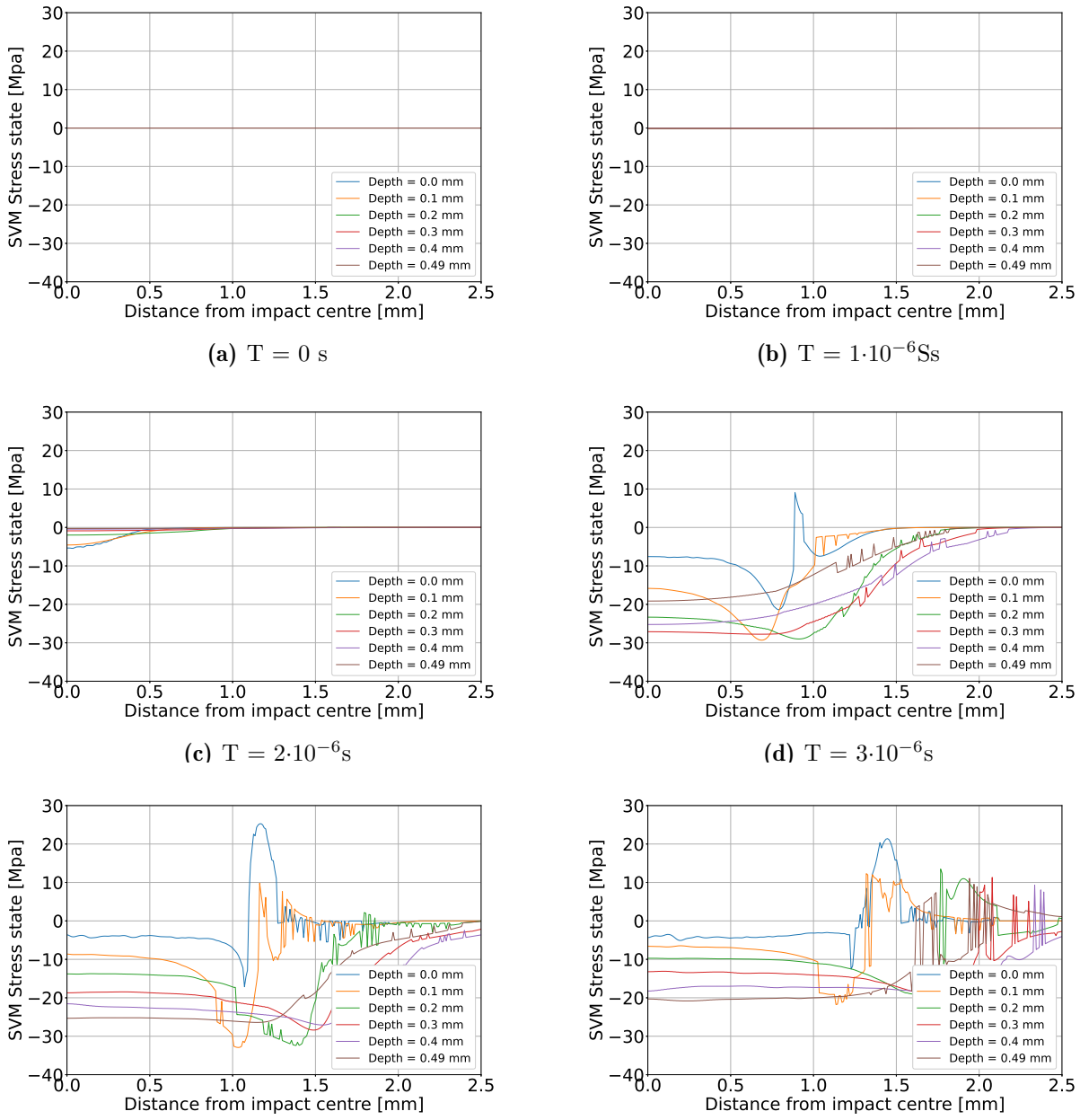

(a) T = 0 s

(b) T = $1{\cdot}10^{-6}$Ss

(c) T = $2{\cdot}10^{-6}$s

(d) T = $3{\cdot}10^{-6}$s

(e) T = $4{\cdot}10^{-6}$s

(f) T = $5{\cdot}10^{-6}$s

Figure 4.2: Signed Von Mises stress state in coating material PU269-4, following liquid droplet impact for V_{impact} = 130 m/s. Visualised for discrete points in time following impact initiation for depth 0-0.5 mm.

The RET lifetime prediction is performed using data from the single impact simulation described above. Damage is evaluated for a depth between 0 and 0.5 mm. Figure 4.3 visualises the distribution of this parameter along the depth of the material at the moment damage occurs, ie when D = 1 is reached in one of the paths. It can be seen that damage occurs within 0.1 mm of the surface, at a depth of about 0.05 mm. This value is prone to variation due to the randomness of the rainfield or when evaluated at a different impact velocity. Therefore a margin should always be taken to make sure the maximum damage occurs within the analysis region. However, according to this RET evaluation method, it can be concluded that damage is most likely to occur in the top 0.1 mm of the coating material. The path spacing of 0.01mm with 10 paths is deemed sufficient for this evaluation method.

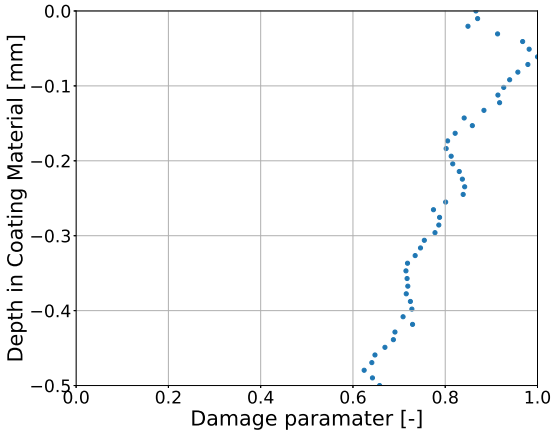

Figure 4.3: Damage formation distribution through thickness of coating material PU269-4 as obtained by the RET prediction tool for V_{impact} = 130 m/s.

Simulation Time
The effect of the simulation time of the 2D-axisymmetric ABAQUS Explicit FE liquid impact simulation, described in subsection 3.3.2, is analysed in terms of the RET prediction results. It should be sufficiently large to capture the full effect of the impact case and provide converged results in terms of the RET lifetime prediction. The pressure profiles simulating the effect of the liquid droplet on the coating material are time-dependent and last $7.24{\cdot}10^{-6}$ s. This means the state-of-the-art simulation time of $5{\cdot}10^{-6}$s is insufficient to capture the full impact event.

Figure 4.4 visualises the RET lifetime prediction for multiple simulation time cases for coating material PU269-4. On the left, the RET prediction in terms of specific impacts vs impact velocity (N_0 vs V_{impact}) shows a decrease in predicted performance for increasing simulation time. This is further shown in the convergence plot on the right, showing similar behaviour for all impact velocities. No convergence in the re-

sult can be seen for the analysed simulation times, which do capture the full impact event.

This non-converging behaviour can be explained by realising that increasing the simulation time increases the numerical noise included in the analysis. This noise dominates the damage calculations of the RET predictions. It is therefore not possible to set a suitable simulation time for this method of analysis.

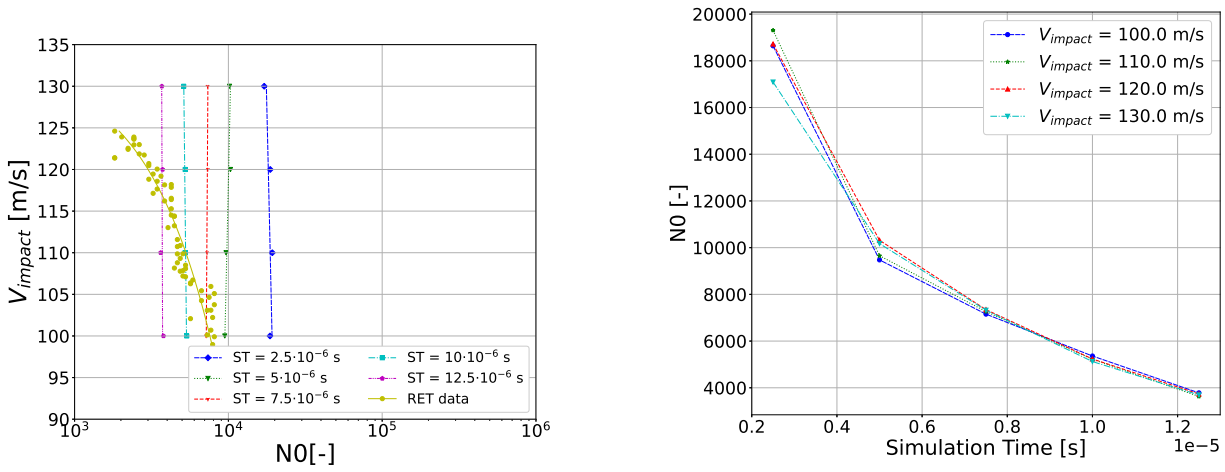

(a) Specific impact vs impact velocity for multiple simulation time (ST) cases

(b) Convergence of RET lifetime prediction with increasing simulation time

Figure 4.4: Investigation to the effect of the simulation time of the 2D-Axisymmetric liquid impact finite element model in terms of RET prediction performance for coating system PU269-4.

Sampling Interval
The sampling interval as defined in the 2D-axisymmetric liquid impact simulation, described in subsection 3.3.2 is investigated in terms of its effect on the RET prediction tool for coating systems PU269-4. The sampling interval is defined as the time between 2 adjacent timestamps extracted from the analysis. This means decreasing this value, increases the number of time steps extracted from the simulation.

Figure 4.5 visualises the RET prediction of PU269-4 for several sampling interval cases. No convergence of the results can be seen. This indicates the decrease in sampling interval does not improve the accuracy of the results. The number of non-physical stress fluctuations is increased and is included in the rainflow counting-based damage calculations. This is expected to keep increasing with decreasing sampling intervals, making it impossible to set a suitable value for sampling intervals for this analysis method.

Conclusion
The main issue with the current state-of-the-art of the RE lifetime prediction tool lies in the numerical noise which is included in the results of the single droplet impact 2D

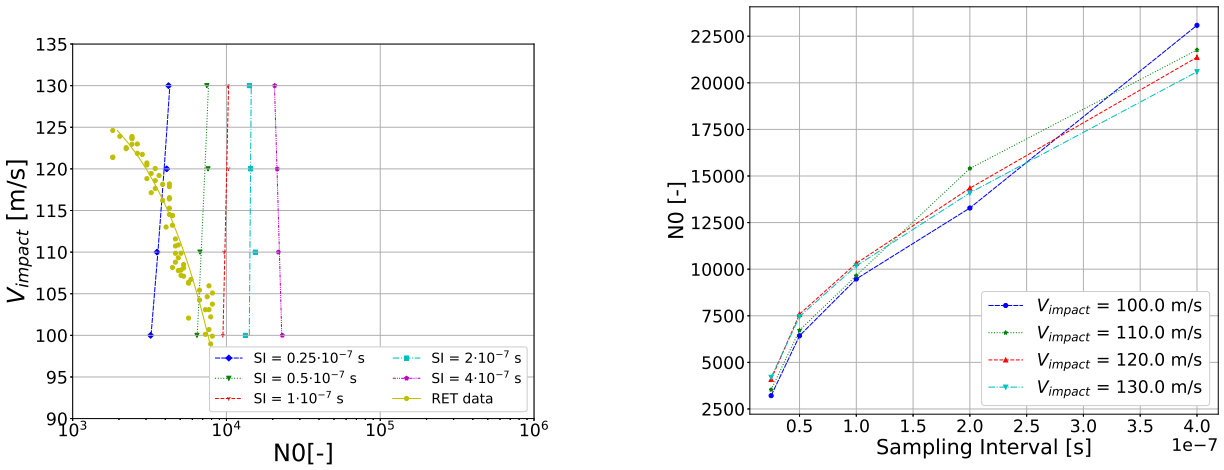

(a) Specific impact vs impact Velocity for multiple Sampling Interval (SI) cases

(b) Convergence of RET lifetime prediction with decreasing Sampling Interval

Figure 4.5: Investigation to the effect of the sampling interval of the 2D-Axisymmetric liquid impact finite element model in terms of RET prediction performance for coating system PU269-4.

axisymmetric explicit finite element simulation. This type of simulation is prone to unrealistic fluctuations in the stress field which influence the rainflow counting-based damage evaluation as utilised in the RE lifetime prediction tool. These non-physical stress fluctuations dominate the damage calculation and therefore little influence is found due to the increased maximum stress found for increasing impact velocity.

This behaviour is recognised in the RET lifetime prediction and its dependence on the number of time-frames extracted from the droplet impact simulation. A higher number of frames, as obtained by a longer simulation or decrease in sampling interval, results in decreased lifetime predictions, with no converged results found. This is a non-physical result and can only be explained by numerical errors as introduced by the explicit finite element simulation.

4.3 Alternative Evaluation Methods

To solve the issues with the current state-of-the-art of the RE lifetime prediction tool, two alternative solution methods are proposed, aimed to reduce the effects of numerical noise in the lifetime calculation. First, a minimum threshold is applied which aims to filter out unrealistic stress fluctuations from the stress history of a single droplet impact. Secondly, the full stress history is converted to a single stress wave of which the amplitude is determined from the extreme stress values over the full impact case.

4.3.1 Minimum stress amplitude threshold

A threshold of minimum stress amplitude is set in the rainflow counting algorithm, prior to the damage calculation. This will ensure the final prediction is a function of the higher amplitude stress waves of which the magnitude is dependent on impact velocity. The challenge here lies in setting the value of this threshold.

An investigation is performed analysing the effect of the magnitude of this threshold of which the results are visualised in Figure 4.6. As can be seen in plot (a), both the absolute value of the prediction as well as its dependence on impact velocity are shown to be highly dependent on the value of minimum stress amplitude to be taken into consideration. Furthermore, plot (b) shows the resulting values for N_0 show converging behaviour when decreasing the minimum stress amplitude threshold. A jump is seen when eliminating the threshold for the benchmark case, indicating the effect of having no stress threshold.

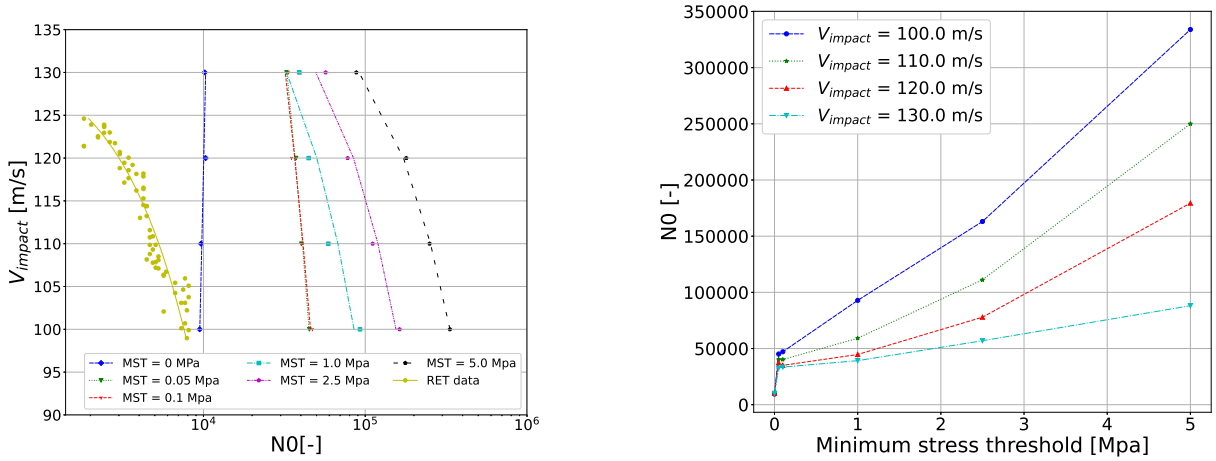

(a) Specific impacts vs impact velocity for different levels of minimum stress threshold (MST)

(b) Convergence of RET lifetime prediction with decreasing minimum stress threshold (MST)

Figure 4.6: RET lifetime prediction in terms of N_0 vs V_{impact} for different levels of minimum stress amplitude for coating PU269-4 (a) and a convergence plot of RET lifetime prediction vs minimum stress threshold level (b).

Comparing the different levels of minimum stress threshold, it can be concluded that the lower value of stress amplitude provides results most consistent with the RET validation data. For the higher stress amplitude values, the absolute error becomes larger and the velocity dependence of the prediction is overestimated. This is in line with expectations since the goal of this threshold is to take out all stress fluctuations due to numerical noise. Higher amplitude stress waves have a physical basis in the impact case and are thus to be considered in the analysis. Convergence is seen for a minimum stress amplitude limit

of 0.1 MPa, with lower values (ie. 0.05 Mpa) providing similar results.

Path Definition
Utilising the same methodology as the full stress history analysis method, the RET prediction is performed for a depth of 0-0.5mm, while applying a 0.1 Mpa filter on the rainflow counter prior to the damage calculation. The analysis is performed for coating material PU269-4 with 50 paths using an equal spacing of 0.01mm. Figure 4.7 visualises the distribution of damage at the moment of damage initiation (D = 1 in one of the paths).

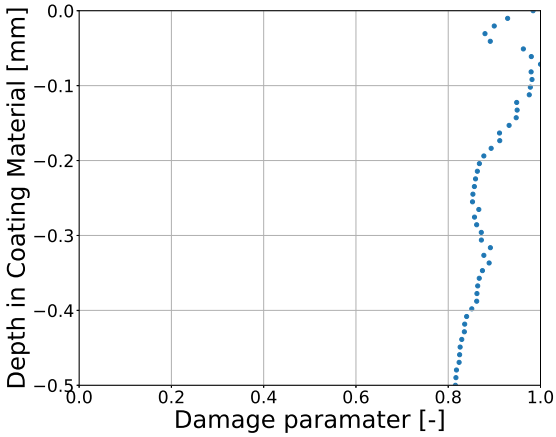

Figure 4.7: Damage distribution through the thickness of coating material PU269-4 as obtained by the RET prediction tool as analysed with a minimum stress threshold of 0.1 Mpa on the stress history for V_{impact} = 130 m/s.

Damage is shown to occur just below the surface, at about 0.07 mm. This means that for subsequent analysis, 10 paths with a spacing of 0.01 can be expected to extract the critical damage cases in the coating material. Furthermore, it can be noted that compared to the full stress history case, substantially less variation in the damage parameter can be seen when looking deeper into the material.

Simulation Time
For a minimum stress amplitude of 0.1 Mpa, a convergence study is performed to the effect of simulation time of the 2D-axisymmetric liquid impact finite element model, described in subsection 3.3.2, on RET lifetime prediction in terms of specific impacts until incubation. Figure 4.8 visualises the results in terms of the full lifetime prediction for various impact speeds (a) and terms of a convergence plot of RET lifetime in terms of specific impacts vs simulation time (b). The absolute error of the RET prediction with the validation data is shown to decrease with increasing simulation time. Furthermore, the linear fit, indicating the velocity dependence of the prediction, is shown to be affected by the simulation time. Converging behaviour can be seen for increasing simulation time,

with convergence at a simulation time of $12.5{\cdot}10^{-6}$ s. This value will therefore be taken for subsequent analysis using this method of RET lifetime prediction.

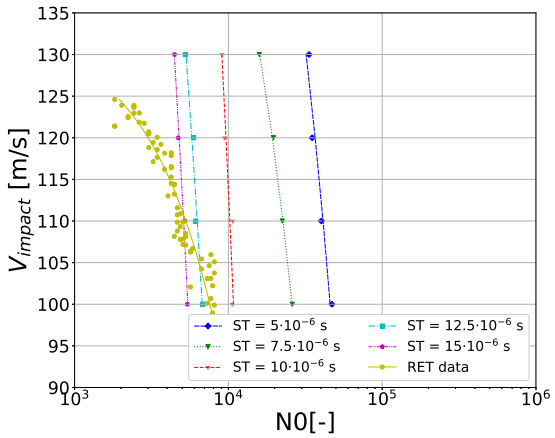

(a) Specific impact vs impact velocity for multiple simulation time (ST) cases

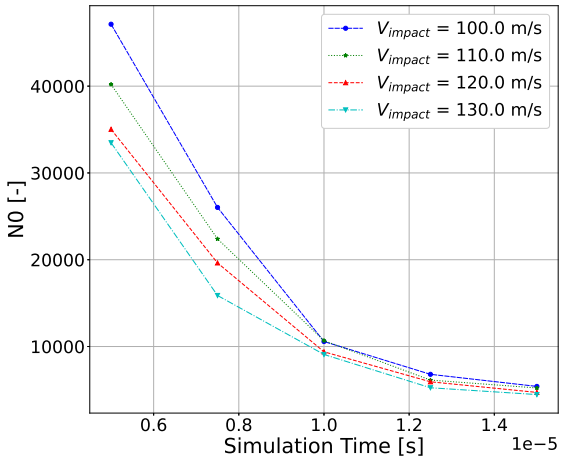

(b) Convergence of RET lifetime prediction with increasing simulation time

Figure 4.8: Investigation to the effect of the simulation time of the 2D-axisymmetric liquid impact finite element model in terms of RET prediction performance using a minimum stress amplitude threshold of 0.1 Mpa, for coating material PU269-4.

Sampling Interval
The effect of the sampling interval of the liquid impact model is investigated in terms of RET lifetime prediction when applying a minimum stress amplitude threshold on the stress history. Figure 4.9 visualises the results. Converging behaviour can be seen with decreasing sampling intervals up to $1{\cdot}10^{-7}$ s. This can be explained by the high-frequency fluctuations which are found in the explicit finite element impact model. The effects of further decreasing the sampling interval thus do not add additional accuracy to the results. A sampling interval of $1{\cdot}10^{-7}$ s is taken as the converged result and will be used for subsequent analysis using this analysis method.

4.3.2 Stress Amplitude Conversion

An alternative evaluation method is proposed which converts the full stress history from a single droplet impact with a single stress wave of which the amplitude is determined by the maximum and minimum stress experienced by the material, over the full time of the impact case. Equation 4.4 is applied for each droplet generated for the simulated RET rainfield, where σ_{max} and σ_{min} are a function of the distance of the droplet impact to the evaluation point. This is similar to how the stress states are determined for SPIFT testing conditions. The SN curve construction is based on the maximum stress amplitude

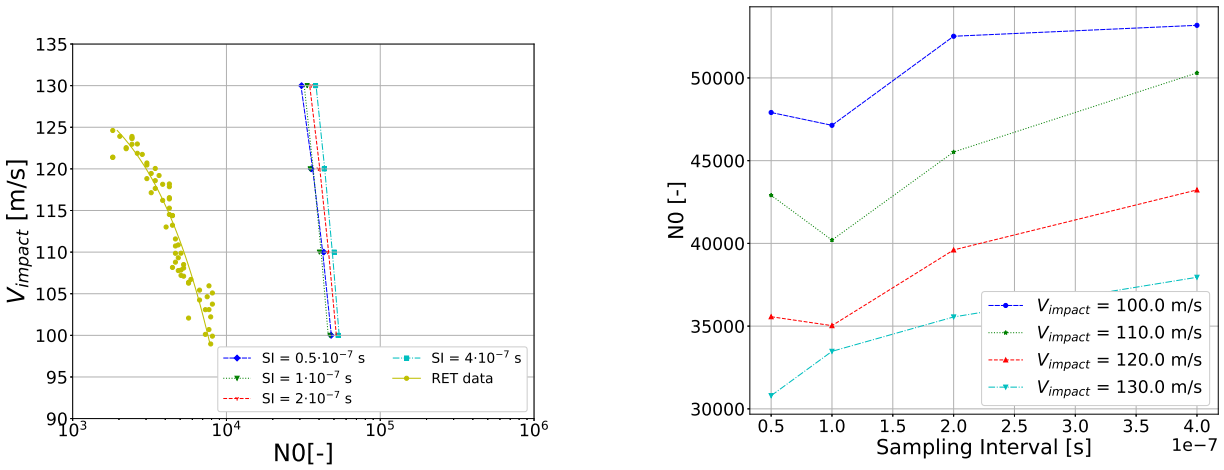

(a) N0 vs V_{impact} for multiple sampling interval (SI) cases

(b) Convergence study of RET lifetime prediction with decreasing sampling interval

Figure 4.9: Investigation to the effect of the sampling interval of the 2D-Axisymmetric liquid impact finite element model in terms of RET prediction performance using a minimum stress amplitude threshold of 0.1 Mpa, for coating material PU269-4.

experienced during SPIFT testing as evaluated by the SPIFT finite element impact model. By also applying this method to the droplet impact model, similar techniques are used for the determination of the damage limit (SN curve) and loading conditions (droplet impact) of the coating material.

$$\sigma_{drop} = \frac{\sigma_{drop_{max}} - \sigma_{drop_{min}}}{2} \tag{4.4}$$

This method of evaluation is expected to reduce the effect of numerical noise as generated in the impact simulation on the RET lifetime prediction. Furthermore, the computational effort required for the RET lifetime prediction is expected to be reduced by this method of evaluation, as fewer points in the stress history are considered in the damage calculation. Further specification of the simulation parameters defining the 2D-axisymmetric model is done to refine this analysis method.

Path Definition

Utilising the same methodology as for the full stress history case, the RET prediction is performed for a depth of 0-0.5mm into the coating material, for material PU269-4. Figure 4.10 shows the distribution of the damage parameter along the thickness of the coating material at the point damage is reached. It can be seen that damage is expected to occur deeper in the coating material when utilising this method. This behaviour can be explained that this method captures the depth at which maximum stresses occur, which will correspond to the point of the maximum damage. The apparent random variation due to the numerical noise is eliminated. This observation means the number of

paths defined in the analysis should be increased. The maximum depth to be considered is set to 0.3 mm, to account for any variation due to the rainfield of the material system. The path spacing is increased to minimise the increased computational requirements.

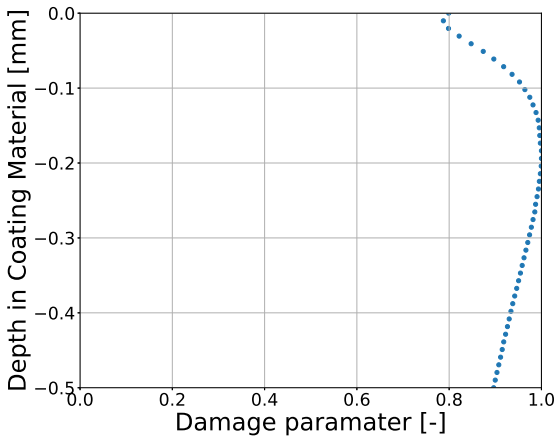

Figure 4.10: Damage formation distribution through the thickness of coating material PU269-4 as obtained by the RET prediction tool as analysed by the stress amplitude conversion method for $V_{impact} = 130$ m/s.

Simulation Time
The RET prediction tool for the stress amplitude conversion method is analysed in terms of the simulation time of the 2D-axisymmetric liquid impact model. Figure 4.11 shows the RET lifetime prediction in terms of N_0 vs V_{impact} for different simulation time cases (a) and in the form of a convergence plot for lifetime prediction as function of simulation time (b). An insufficiently high simulation time cuts the impact case short and might thus result in an underestimation of the extreme stress cases due to the impact event. The results are shown to converge at a simulation time of $1.25{\cdot}10^{-5}$ s.

Sampling Interval
A similar study is performed on the sampling interval for the stress amplitude conversion method. Figure 4.12 shows the results. It can be seen that, for all impact velocities, little variation is found in terms of RET lifetime prediction when varying the sampling interval of the liquid impact model. Already at relatively high values for sampling interval ($2{\cdot}10^{-7}$), converged results can be seen. This indicates the extreme stresses of as experienced by the coating material in the liquid impact simulation, can already be estimated accurately for high values of sampling interval. Lowering the sampling interval could be a way of decreasing the computation requirements of this RET prediction evaluation type.

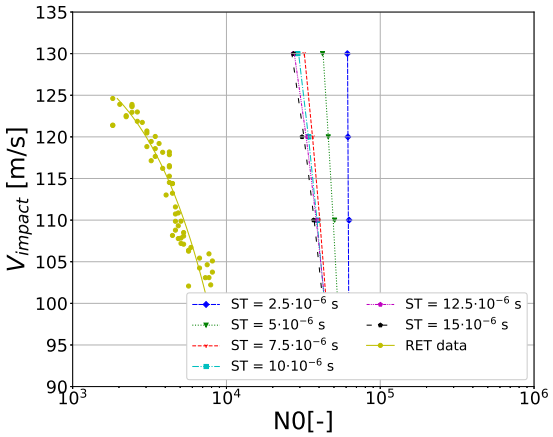

(a) Specific impact vs impact velocity for multiple simulation time (ST) cases

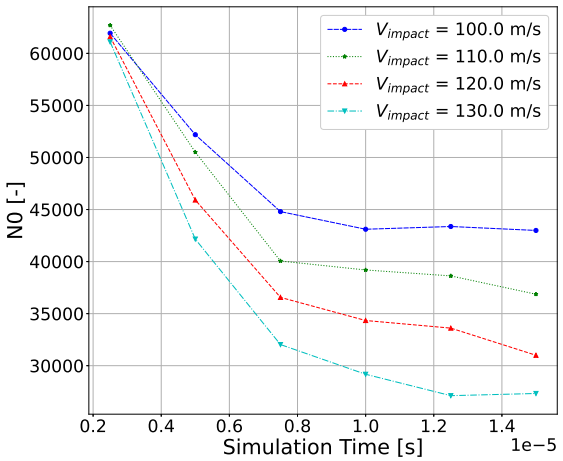

(b) Convergence of RET lifetime prediction with increasing simulation time

Figure 4.11: Investigation to the effect of the simulation time of the 2D-Axisymmetric liquid impact finite element model in terms of RET prediction performance, for coating material PU269-4, for the stress amplitude conversion method.

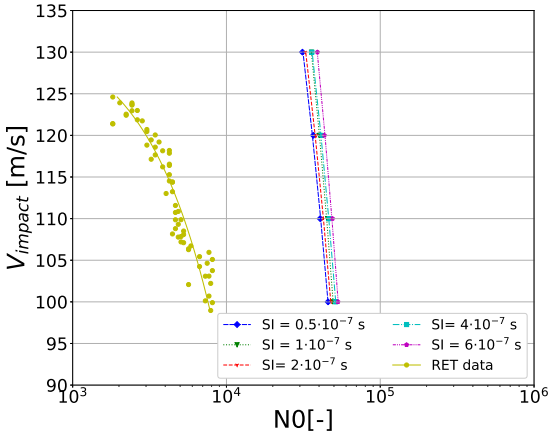

(a) Specific impact vs impact velocity for multiple Sampling interval (SI) cases

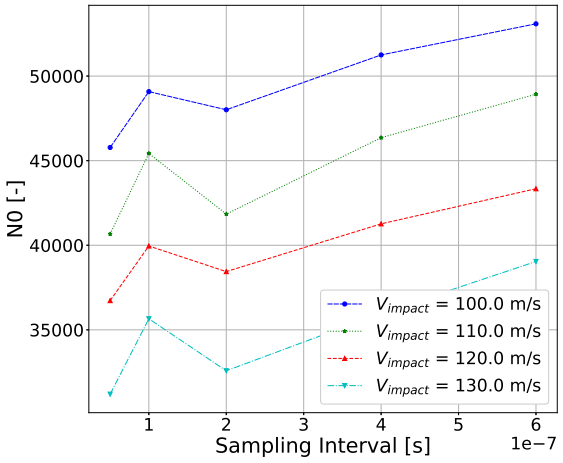

(b) Convergence of RET lifetime prediction with decreasing sampling interval

Figure 4.12: Investigation to the effect of the sampling interval of the 2D-Axisymmetric liquid impact finite element model in terms of RET prediction performance for coating system PU269-4 for the stress amplitude conversion method.

4.3.3 Result Comparison

Three evaluation methods for the RE lifetime prediction tool have been presented and analysed. Convergence studies have been performed on the effect of the simulation parameters of the liquid impact model which forms the basis of the lifetime prediction. The optimal simulation parameters for the individual evaluation methods are presented in Table 4.2.

Table 4.2: Simulation parameters for individual evaluation methods.

	Unit	Full Stress History	Stress amplitude threshold	Stress amplitude conversion
Number of Paths	[-]	10	15	15
Path Spacing	[mm]	0.01	0.01	0.02
Path length	[mm]	2.5	2.5	2.5
Simulation Time	[s]	$5.0{\cdot}10^{-6}$	$1.25{\cdot}10^{-5}$	$1.25{\cdot}10^{-5}$
Sampling Interval	[s]	$1.0{\cdot}10^{-7}$	$1.0{\cdot}10^{-7}$	$1.0{\cdot}10^{-7}$

The RET lifetime prediction is performed for all three analysis methods for coating material PU269-4. The results are captured in Figure 4.13. The raw data of the results of the predictions are captured in Table 4.3, in terms of the absolute value of the lifetime prediction and slope of the linear fit applied to the analysed impact velocities.

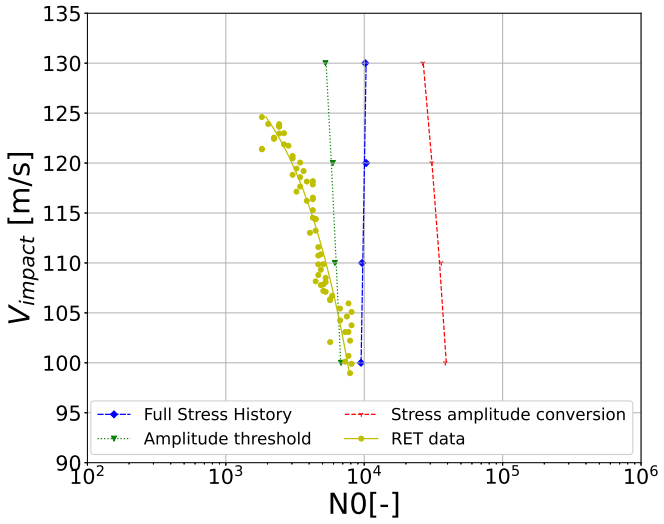

Figure 4.13: RET lifetime prediction comparison for coating material PU269-4 in terms of velocity vs N0 for different analysis methods. Overlaid with RET validation data..

Both alternative evaluation methods improve in terms of the velocity dependence of the RET lifetime prediction of the full stress history evaluation method. When utilising the stress amplitude threshold method of analysis, the velocity dependence of the presented

Table 4.3: Raw data of N_0 RET lifetime prediction analysis method comparison for coating material PU269-4, as visualised in Figure 4.13.

	V_{impact}				**Slope** ($\frac{dV}{d0}$)
	100	**110**	**120**	**130**	
RET Validation	7580	5292	3004	717	-228
Full stress history	94775	9654	10316	10173	28
Stress amplitude limit	6796	6132	5935	5247	-48
Stress amplitude conversion	38519	36040	30664	26482	-414

RET prediction is still underestimated when compared to the RET validation data. This can be solved by choosing a higher threshold for minimum stress amplitude in the rainflow counting algorithm. However, this is also where the biggest issue of this analysis method lies. Since no physical basis is found for the magnitude of this threshold, it will always be subject to tuning to validation data of the material system under investigation. This defeats the purpose of this workflow, namely to be able to analyse different coating systems numerically and thereby alleviate the need for RET testing.

The stress amplitude conversion method does have a physical basis and is, therefore, the preferred method. The performance of the coating material is overestimated however its velocity dependence on the lifetime prediction is captured. Converting the individual impact cases to a single stress wave case underestimates the effect of each impact and therefore an overestimation of the coating material's performance is expected. Furthermore, this method utilises a similar approach as the SN curve construction for which the maximum stress state following SPIFT testing is extracted from the finite element analysis of the SPIFT testing conditions. For these reasons, this method is accepted.

4.4 Conclusions

The benchmark DURALEDGE computational workflow for rain erosion has been subjected to analysis and alternative evaluation methods have been proposed. The master curve construction has been automated, reducing user-introduced subjectivity in the master curves. Furthermore, the cause of the underestimated velocity dependence of the lifetime prediction has been tracked to numerical noise originating from the single droplet impact ABAQUS explicit FE simulation. Two alternative evaluation methods have been proposed of which the stress amplitude conversion method (SAC) has been accepted and implemented into the workflow. These renewed evaluation techniques will be used for the subsequent analysis of the novel coating materials.

CHAPTER 5
Material Analysis

The framework as described in chapter 3 and analysed in chapter 4 will be used for the evaluation of four novel leading-edge coating material systems. The following chapter covers the material description and analysis for all materials under investigation. Details on the material composition are provided in section 5.1. Then, the materials are analysed and their relevant visco-elastic material properties determined, as described in section 5.2. Furthermore, the materials systems are subjected to SPIFT analysis as described in section 5.3. Then, section 5.4 describes the finite element analysis of the SPIFT testing conditions and the stress states in the material systems during SPIFT analysis are discussed. Finally, the coating materials' impact fatigue properties are captured in stress-based SN curves, as described in section 5.5.

5.1 Materials Description

The material systems under investigation are polyurethane-based materials, consisting of a resin system and binder material with varying filler parameters. These include filler type, filler size and filler volume fraction. The binder type and filler volume fraction are varied while the filler size and type are kept constant, leading to a total of four material systems to be investigated. The relevant parameters of the material systems are shown in Table 5.1. The material ID is based on the binder type (Bxxx) and filler volume fraction (FVyy) of the respective material systems. This ID will be used for further identification of the material systems.

Table 5.1: Coating material formulation.

Material ID	Resin	Binder	Filler Type	Filler size	Filler volume fraction
B357-FV30	Desmophen NH1420	LSSUT-357	Al_2O_3	2 μm	30%
B357-FV15	Desmophen NH1420	LSSUT-357	Al_2O_3	2 μm	15%
B368-FV30	Desmophen NH1420	LSSUT-368	Al_2O_3	2 μm	30%
B368-FV15	Desmophen NH1420	LSSUT-368	Al_2O_3	2 μm	15%

5.2 Material Properties

The coating materials under investigation are subjected to DMTA analysis and processed following the methodology as described in section 4.1. The master curves are constructed

via the automated master curve construction tool. The Yeoh-prony hyper-and viscoelastic model is calibrated for each material system.

5.2.1 DMTA Analysis and master curve s

The coating systems are subjected to DMTA analysis, extracting the storage and loss modulus for excitation frequencies [10^{-1},10^{3}] Hz, at temperature levels in the range of [-80, 100] °C. The raw data is visualised for an excitation frequency of 1 Hz, as shown in Figure 5.1. The glass transition temperature (T_g) is taken as the temperature where tanδ maximises. This reveals binder 368 to have a relatively higher T_g, compared to binder 357.

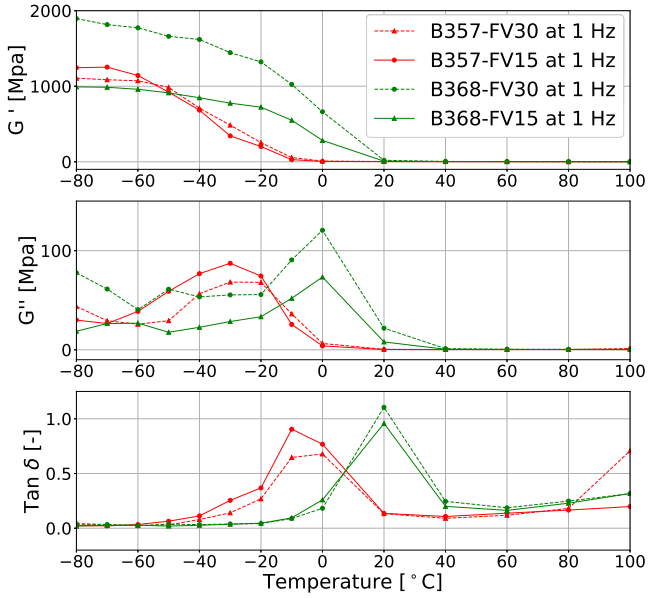

Figure 5.1: Storage modulus (top), loss modulus (middle) and loss factor (bottom) master curve s in temperature domain for excitation frequency $f = 1$ Hz, for coating material B357-FV30, B357-FV15, B368-FV30 and B368-FV15.

The DMTA data is converted to the frequency domain by applying the time-temperature superposition principle. The automated master curve construction tool is used following the methodology elaborated in section 4.1. A reference temperature (T_{ref}) of 20 °C is assumed for all material systems. Further detail on master curve construction is found in Appendix A, Figures A.1, A.4, A.7 and A.10. Here, DMTA frequency sweeps for different temperature levels before and after applying horizontal shifting are shown for the respective materials. The final master curve for the storage modulus, loss modulus and tan δ is extracted from this analysis, as visualised and compared in Figure 5.2.

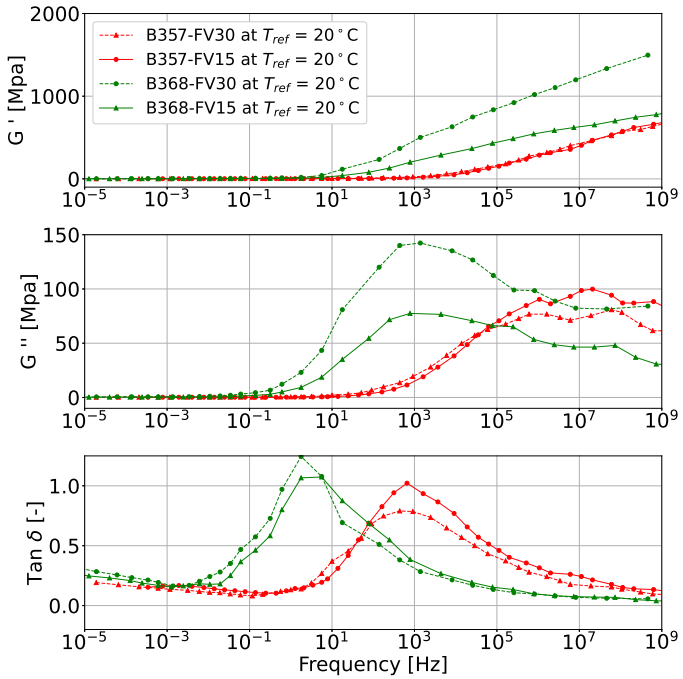

Figure 5.2: Storage modulus (top), loss modulus (middle) and loss factor (bottom) master curve in frequency domain constructed at reference temperature T_{ref} = 20 °C, for coating material B357-FV30, B357-FV15, B368-FV30 and B368-FV15.

When comparing the master curves for the different binder systems, several conclusions can be drawn. Firstly, the loss modulus and loss factor maximise at a lower frequency for binder system 368 when compared to binder system 357, This leads to relatively lower values of tanδ at high excitation frequencies (>10^3 Hz) for this binder type. This indicates lower relative energy absorption and a more elastic response when loaded in this range of excitation frequency. Secondly, the differences due to filler volume fraction are shown to be less significant than the differences due to the binder type. When comparing the high excitation frequency regions, a slight decrease in tanδ can be seen for the high filler volume fraction case of both binder types. This indicates an increase in filler volume could decrease the relative absorption energy for these excitation frequencies. However, the uncertainty introduced by the master curve construction procedure must be considered, especially in this frequency range.

The shift factors used for the master curve construction of the respective materials systems are subjected to WLF and Arrhenius model fit for temperatures above and below Tg respectively. The resulting model parameters and additional relevant material data are summarised in Table 5.2. Furthermore, a comparison of the shift factors applied to the respective material systems is visualised in Figure 5.3. The curves intersect at [T = 20°C, SF = 1] since this point corresponds to the reference temperature at which all

master curve s are constructed. Binder 368 is shown to require more extreme shift factors when compared to binder system 357, indicating a greater influence of temperature on the behaviour of the material. Differences due to the filler volume fraction are harder to identify, with smaller differences seen and no real trend for different temperature levels.

Table 5.2: Coating material shifting factor model parameters and relevant temperature values.

Material ID	$C_1[°C]$	C_2[-]	**H** [kJ/Mol]	T_{g1Hz}^{DMA} [$°C$]
B357-FV30	8.19	106.88	-204589.94	0
B357-FV15	5.39	75.90	-188827.65	-10
B368-FV30	8.68	66.67	-251127.46	20
B368-FV15	8.67	65.32	-248481.06	20

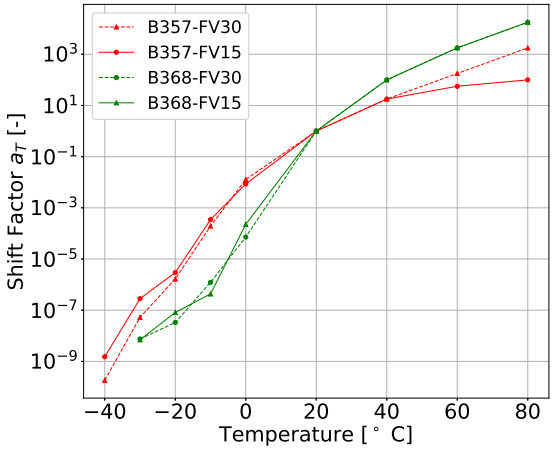

Figure 5.3: Master curve construction shift factor comparison for coating material B357-FV30, B357-FV15, B368-FV30 and B368-FV15.

5.2.2 Hyper- and Viscoelastic Model Calibration

The coating material master curve s are captured in Yeoh-Prony hyper-and viscoelastic model, following methodology elaborated in section 3.2. An acceptable fit level is found for all material systems with the R^2 value at a minimum of 0.99 for all materials. The final fit to the experimental DMTA data is shown in Appendix A, Figures A.3, A.6, A.9 and A.12, for coating materials,B357-FV30, B357-FV15, B368-FV30 and B368-FV15 respectively. Furthermore, the model parameters corresponding to the individual coating materials are presented in Tables A.1 to A.4.

5.3 SPIFT Analysis

The material systems are subjected to SPIFT experimental analysis to obtain their respective impact fatigue life material parameters. The SPIFT working mechanisms and data recording techniques are elaborated upon in subsection 3.1.2. A preliminary investigation is conducted into the materials systems in which the acoustic emissions and temperature profiles of the impact surface are recorded. These investigations are used for comparison and evaluation of the impact behaviour of the individual material systems. Furthermore, the minimum shooting frequency for the subsequent impact fatigue test can be determined. It must be noted that the 'shooting frequency' relates to the frequency of individual impact cases during SPIFT testing, while 'excitation frequency' as used in the master curves relates to the strain rates experienced by the test specimen in a single impact case. For the impact fatigue analysis, the number of impacts until failure is recorded for a range of impact velocities and, when possible, a VN curve is constructed.

5.3.1 Test Specimen

The coating material has been cast onto a 3 mm glass-fibre reinforced polymer plate of dimensions 200x400 mm. From this, 16 test specimens have been cut out with individual dimensions of 39x39 mm. The coating thickness varies from 4-6 mm for the individual specimen. The thickness miss-match is assumed to have minimum effect on the results since all specimens show high thickness values (>3mm) and a further increase is known to have minimal effect on stress propagation. Figure 5.4 visualises an example test specimen for each material system. The label visible on the surface of the specimen relates to the in-house label of the individual material systems (A to D) and the specimen number of said material system (16).

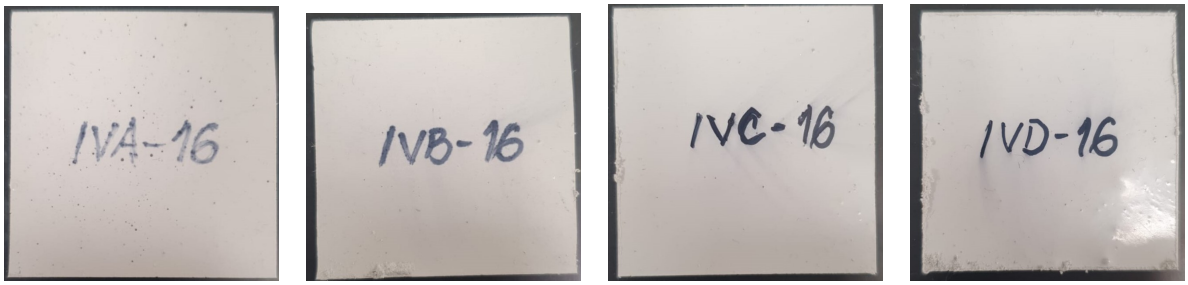

(a) B357-FV30 **(b)** B357-FV15 **(c)** B68-FV30 **(d)** B368-FV15

Figure 5.4: SPIFT test specimen for coating material B357-FV30, B357-FV15, B368-FV30 and B368-FV15.

Visual inspection of the test specimen reveals defects visible on the surface of the specimens. Air bubbles, small cracks and general impurities can be identified on the surface and sides of several specimens. Impurities visible directly at the surface are to be identified before the test and damage originating from these impurities are to be disregarded. Finally, the labelling of the individual specimen is done on the impact

surface of the test specimen, due to miscommunication in the production phase. This slightly obstructs the damage detection of the test specimen. The permanent marker is not erasable with non-corrosive solvents. All specimens are cleaned with Ethanol, prior to any SPIFT test.

5.3.2 AE and IR investigation

The material systems described in Table 5.1 are impacted with a rubber ball with V_{impact} increasing from 130 to 175 m/s. A shooting interval of 15 seconds is used, which is assumed to be sufficient for the impact cases to be independent of each other. The specimen is constantly air-cooled during testing. The impact surface is recorded by IR measurement and the surface temperature is tracked throughout the test. Furthermore, AE data is recorded.

Acoustic Emissions
Figure 5.5 visualises the absorption energy (a) and hit duration (b) as experienced by the AE sensor. Little difference can be recognised between the materials in terms of hit duration. However, it can be seen that binder system 368 has a relatively higher energy absorption than binder system 357, for both magnitudes of filler volume fraction. This indicates that for this binder system, a relative higher fraction of the kinetic energy of the rubber ball is transferred to the test specimen in the form of kinetic energy. The binder system provides a more elastic response to the impact. This can be related to the material's visco-elastic properties, expressed by the $tan\delta$ as a function of excitation frequency as shown in the bottom plot of Figure 5.2. The impact of the rubber ball has been proven to provide exiting frequencies within the coating material above 10^5 Hz. In this range, binder 368 shows lower values of $tan\delta$, indicating relatively lower energy dissipation.

Comparison of the filler volume fraction of the respective binder systems shows somewhat unexpected results. In the $tan\delta$ master curve shown in Figure 5.2, a lower value of $tan\delta$ is found for the higher filler volume fraction case (30%), for both binder systems. This would indicate a higher energy absorption perceived by the AE sensor over the full range of impact velocities. This trend is recognised in binder 368, however, for binder 357, an opposite trend is found. This difference could be explained by the uncertainty in the master curve for high-frequency loading. Furthermore, these tests are conducted at an ambient surface temperature of about 28 $°C$, while the master curves shown in Figure 5.2 utilise a reference temperature of 20 $°C$. Finally, impurities and differences in thickness in the SPIFT test specimen could affect the results.

Temperature generation
The maximum surface temperature of the test specimen is tracked for the full duration of the test. The time-temperature profiles as measured by the IR camera are extracted and visualised in Appendix B, Figure B.1. From these raw temperature profiles, two parameters are determined: the surface temperature increase following an impact case and

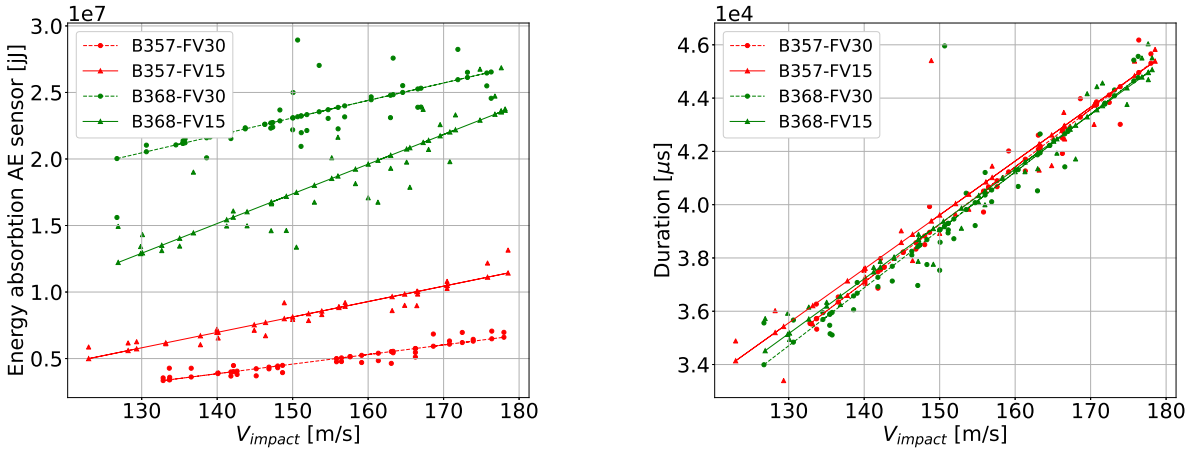

(a) AE absorption energy vs V_{impact}

(b) AE Duration vs V_{impact}

Figure 5.5: Comparison of absorption energy and hit duration as captured by the AE sensor in SPIFT analysis for coating material B357-FV30, B357-FV15, B368-FV30 and B368-FV15.

the time until the surface temperature reaches its steady-state value. The steady-state temperature is defined as the point where the temperature falls within 0.2 °C (2x the resolution of the IR camera) of the temperature just before the impact event.

Figure 5.6 visualised the surface temperature increase (a) and time to steady state temperature (b) for the material systems under investigation, including a linear fit to the raw data. Binder system 357 is shown to reach higher surface temperatures than binder system 368, for the full range of impact velocities. This can be related to the relative higher $tan\delta$ for binder system 357, for excitation frequencies above 10^5 Hz. This is also seen in the AE measurements, where the relative lower absorption energy is seen by the AE sensor for binder system 357. It can thus be concluded that a relatively greater amount of kinetic energy of the rubber ball before impact is converted into heat for binder system 357, compared to binder system 368. In terms of filler volume fraction, smaller differences can be seen. For binder system 357, a higher filler volume fraction shows a greater increase in surface temperature. Binder system 368 shows an opposite behaviour with a high filler volume fraction showing lower temperature increase following impact. This behaviour is in line with behaviour seen in the AE absorption energy.

The time to steady-state graph (b in Figure 5.6) is used for the determination of the maximum shooting frequency for impact fatigue testing. The respective material systems are to be kept at ambient temperature levels (approximately 28 $°C$ surface temperature) since the material properties are a function of temperature. The linear fit represents the minimum interval between 2 impact cases that should be applied to ensure that the

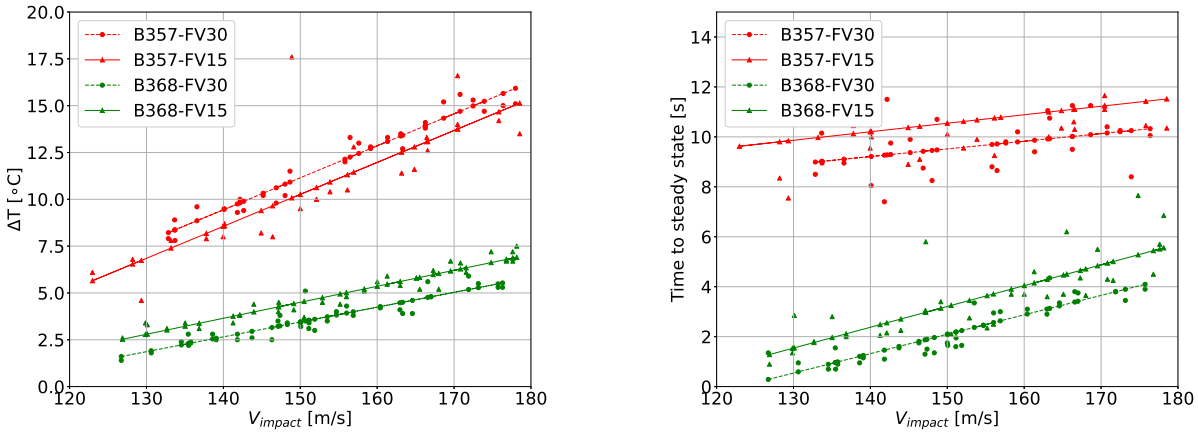

(a) Temperature increase vs V_{impact}

(b) Time to steady state vs V_{impact}

Figure 5.6: Surface temperature increase and time to steady state following rubber ball impact in SPIFT testing, coating material B357-FV30, B357-FV15, B368-FV30 and B368-FV15.

full fatigue test is carried out at ambient temperature levels. It can be seen that binder system 357 shows a longer recovery time to steady-state temperature compared to binder system 368. For both binder systems, a higher filler volume fraction shows a faster return to steady-state temperature.

5.3.3 Impact Fatigue Test

The material systems are subjected to impact fatigue testing, for a range of impact velocities. The number of impacts until failure is recorded and a velocity - number of impacts until the failure curve is fitted to the data points. Each material system is discussed and the test results are presented. When possible, the obtained VN relation is presented. Table B.1 in Appendix B provides URL links to the raw data files of the surface recording for all individual tests.

For all material systems, high impact velocities (>150 m/s) have been analysed to reduce testing times. The impact speed mean and standard deviation are based on the first 250 shots of the test and assumed representable for the full test period, due to limitations of the recording equipment. The shot interval, defined as the time between 2 shots, has been set so the surface temperature returns to its steady-state value before firing the next shot. The total number of shots fired in the test has been derived from AE measurements of the number of hits recorded over the full duration of the test.

Failure is determined via visual inspection of the impact surface, as further elaborated upon in subsection 3.1.2. Distinction between failure due to pre-existing defects, such

as air bubbles, and damage due to repeated stress cycles is made. Further details on the determination of the number of shots until incubation, and interpretation of the individual test results, are provided in the individual material descriptions. Here, yellow indications in the figures relate to failure due to pre-existing defects and are not considered in the determination of incubation. The red markers show the incubation point.

B357-FV30
The test data for the fatigue test performed for material system B357-FV30 is visualised in Table 5.3. The high damping of impact energy of this material leads to relatively high temperature increases following impact. The time to steady-state temperature restricts the shooting frequency leading to prolonged testing times.

Table 5.3: Coating material B357-FV30 impact fatigue test data.

Test number [-]	V_{impact} **mean [m/s]**	V_{impact} **std [m/s]**	**Shot interval [ms]**	**Cooling [y/n]**	**Nshots incubation [-]**	**Total Nshots [-]**
A-1	174.54	2.63	11000	y	35	1579
A-2	165.01	3.37	10000	y	26	2065

Determination of incubation time proves to be difficult for this material system. Following a low number of impacts (N_i<50), defects begin to visualise at the surface of the test specimen. These defects evolve and grow over the full length of the test. This type of failure is assumed to originate from pre-existing impurities in the test specimen. Both tests performed show similar behaviour. Figures 5.7 and 5.8 show the initial state, incubation point and final point in the test. The defects revealed in the incubation point show progress over the full duration of the test. The damage is restricted to pitting and no crack formation is seen in either test. Furthermore, the rubber ball is shown to heavily secrete on the test specimen, making visual damage detection more challenging.

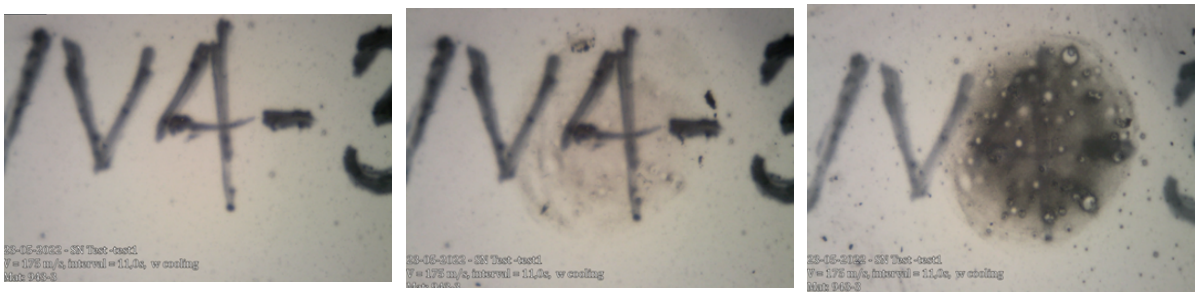

(a) $N_{impact} = 0$ **(b)** $N_{impact} = N_{imcubation}$ **(c)** $N_{impact} = N_{test}$

Figure 5.7: SPIFT test damage detection for material B357-FV30, Test A-1 (V_{impact} = 175.54 m/s).

Defect-driven damage seems to dominate this material when subjected to SPIFT analysis. This leads to the failure of this material to follow a more stochastic pattern, rather than

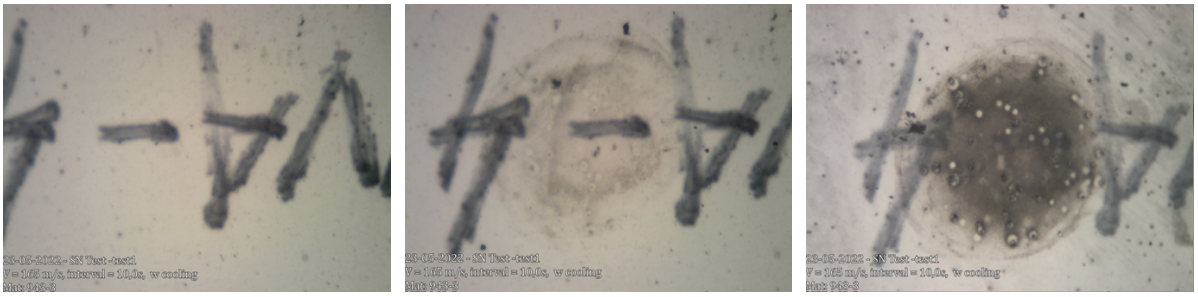

(a) $N_{impact} = 0$ **(b)** $N_{impact} = N_{imcubation}$ **(c)** $N_{impact} = N_{test}$

Figure 5.8: SPIFT test damage detection for material B357-FV30, Test A-2 (V_{impact} = 165.01 m/s).

velocity-dependent behaviour. Damage forms around impurities in the material, causing stress concentrations. This effect dominates the failure behaviour and therefore little velocity dependence is found, implying a VN curve might not capture this materials impact fatigue behaviour. This observation leads to the conclusion that the construction of a relevant VN curve is not feasible for this material system.

B357-FV15
The test data for the fatigue test performed for material system B357-FV15 is visualised in Table 5.4. Similar heating effects are seen for this material as for material system B357-FV30, resulting in relatively high shooting intervals.

Table 5.4: Coating material B357-FV15 impact fatigue test data.

Test number [-]	V_{impact} **mean [m/s]**	V_{impact} **std [m/s]**	**Shot interval [ms]**	**Cooling [y/n]**	**Nshots incubation [-]**	**Total Nshots [-]**
B-1	171.45	2.05	12000	y	-	2137
B-2	167.36	2.08	11000	y	-	2501

Figures 5.9 and 5.10 visualise the progression of the test for test B-1 and B-2, respectively. Three stages are shown, the start of the test, the midpoint of the test and the final state of the test specimen. The rubber ball is shown to heavily secrete on the test specimen, obscuring vision. Different shades of grey could indicate some forms of damage, however detailed inspection of the specimen shows no relevant failure in terms of pitting, crack formation or material loss. The test was ended due to the prolonged testing times (>8 hours) for both tests B-1 and B-2. No incubation time can be determined for the tested impact velocities and utilised testing times. Since lowering the impact velocity is expected to prolong the time to incubation, unrealistically long testing periods will be required. For this reason, the construction of a valid VN curve is deemed unfeasible for this material system.

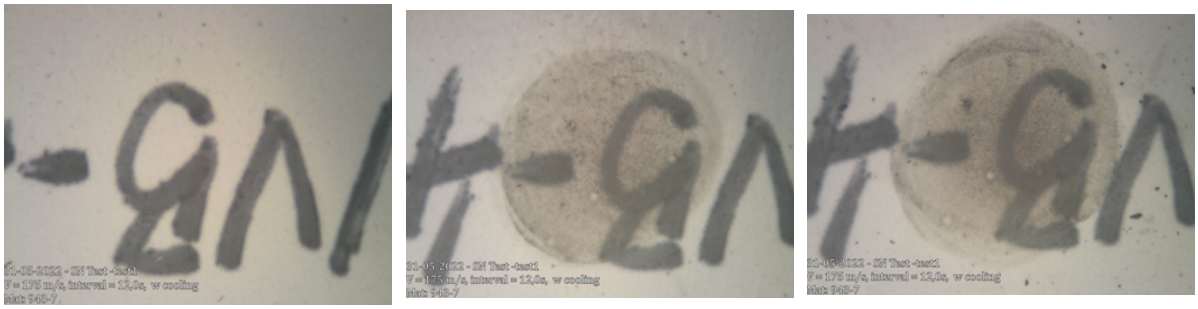

(a) $N_{impact} = 0$ **(b)** $N_{impact} = \frac{1}{2}N_{test}$ **(c)** $N_{impact} = N_{test}$

Figure 5.9: SPIFT test damage detection for material B357-FV15, Test B-1 (V_{impact} = 171.45 m/s).

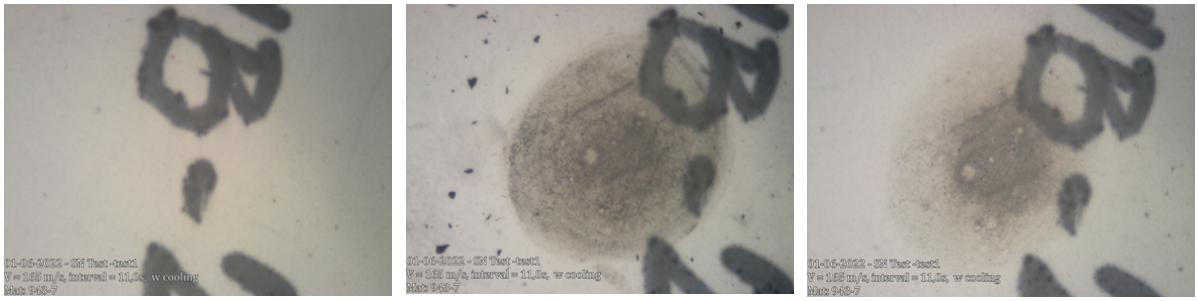

(a) $N_{impact} = 0$ **(b)** $N_{impact} = \frac{1}{2}N_{test}$ **(c)** $N_{impact} = N_{test}$

Figure 5.10: SPIFT test damage detection for material B357-FV15, Test B-2 (V_{impact} = 167.36 m/s).

B368-FV30

The test data for the fatigue test performed for material system B368-FV30 is visualised in Table 5.5. This binder system shows relatively lower damping and heat generation upon impact in SPIFT analysis and thus relatively higher shooting frequencies are allowed.

Table 5.5: Coating material B368-FV30 impact fatigue test data.

Test number [-]	V_{impact} **mean [m/s]**	V_{impact} **std [m/s]**	**Shot interval [ms]**	**Cooling [y/n]**	**Nshots incubation [-]**	**Total Nshots [-]**
C-1	176.41	1.96	5000	y	148	1255
C-2	170.51	2.07	5000	y	618	2034
C-3	164.79	3.44	4000	y	1791	6188
C-4	158.86	1.93	4500	y	1488	2205
C-5	156.44	1.33	3000	y	3173	4909

Figure 5.11 visualises the progression of test C-1 ($V_{impact} = 176.41$ m/s). At the point of incubation, a large number of impurities are seen on the specimen. Incubation is determined when crack formation initiates, originating in one of the defects. The final image of the test ($N_{impact} = N_{test}$) shows the progression of the crack from incubation to the final point of the test.

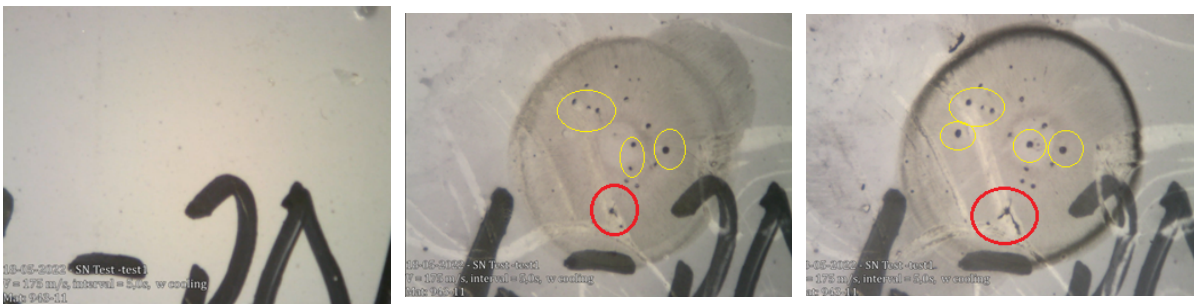

(a) $N_{impact} = 0$ **(b)** $N_{impact} = N_{imcubation}$ **(c)** $N_{impact} = N_{test}$

Figure 5.11: SPIFT test damage detection for material B368-FV30, Test C-1 ($V_{impact} = 176.41$ m/s).

The impact speed is slightly lowered and test C-2 ($V_{impact} = 170.51$ m/s) is conducted. Figure 5.12 visualises the results. Three clear damages due to impurities are seen. Furthermore, in the centre of the specimen, circular crack formation is recognised. The initiation of this crack is taken as the point of incubation.

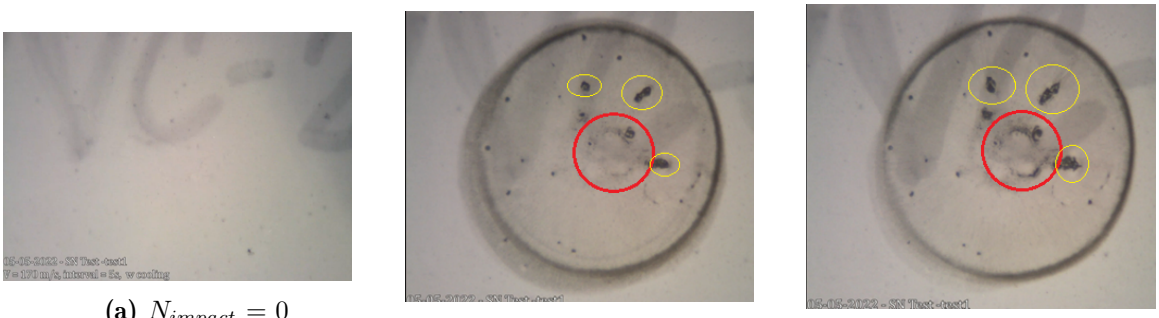

(a) $N_{impact} = 0$ **(b)** $N_{impact} = N_{imcubation}$ **(c)** $N_{impact} = N_{test}$

Figure 5.12: SPIFT test damage detection for material B368-FV30, Test C-2 ($V_{impact} = 170.51$ m/s).

The impact velocity is lowered further and test C-3 ($V_{impact} = 164.79$ m/s) is performed of which the damage progression is visualised in Figure 5.13. Incubation is seen at two locations marked in the figures. Both points are exposed and crack formation is shown to initiate at the point of incubation.

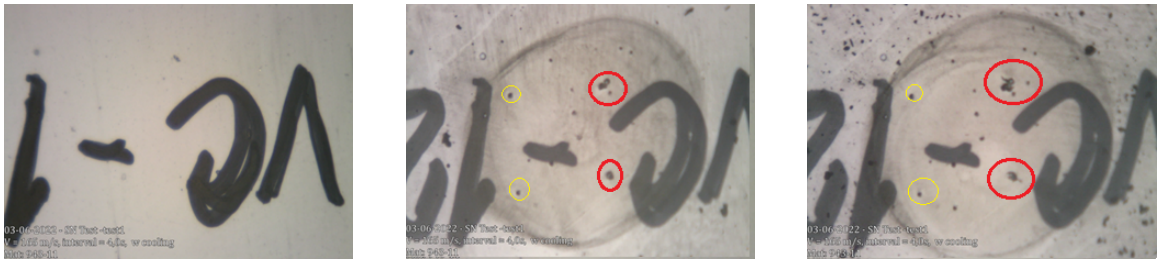

(a) $N_{impact} = 0$ **(b)** $N_{impact} = N_{imcubation}$ **(c)** $N_{impact} = N_{test}$

Figure 5.13: SPIFT test damage detection for material B368-FV30, Test C-3 (V_{impact} = 164.79 m/s).

Figure 5.14 visualises the results of test C-4 (V_{impact} = 158.86 m/s). Pre-existing defects are seen on the surface of the specimen. The markers of the figure $N_{impact} = 0$ show the relevant locations. Incubation is seen in the centre of the specimen in the form of radial cracking, followed by material loss.

(a) $N_{impact} = 0$ **(b)** $N_{impact} = N_{imcubation}$ **(c)** $N_{impact} = N_{test}$

Figure 5.14: SPIFT test damage detection for material B368-FV30, Test C-4 (V_{impact} = 158.86 m/s).

Figure 5.15 visualised the progression of test C-5 (V_{impact} = 156.44 m/s). Defects are observed in an early stage of the test and propagate throughout the test. Two defects join together and a crack is formed from the edge of this failure. The joining of the two defects is marked as the incubation point.

The results of the impact fatigue test of material B368-FV30, as summarised in Table 5.5, are combined in the materials VN curve. Figure 5.16 visualises this result. The individual raw data points, corresponding to the incubation point, of the individual impact velocities are shown, as well as the final curve fit. A substantial scatter can be seen between the final curve fit and the data points, indicating a large uncertainty in the final result. This will be discussed further in the discussion section.

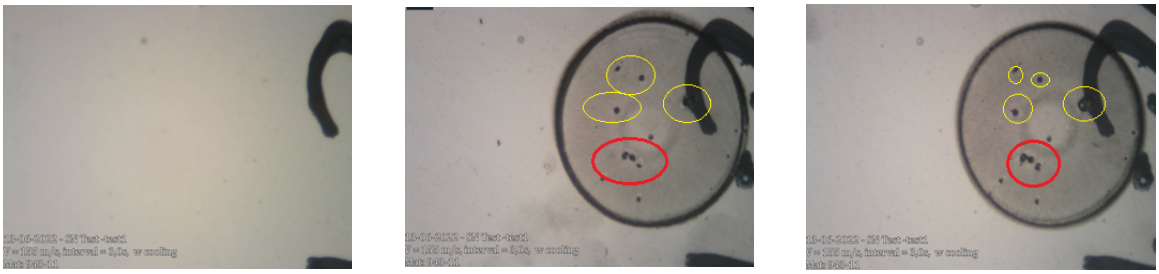

(a) $N_{impact} = 0$ **(b)** $N_{impact} = N_{imcubation}$ **(c)** $N_{impact} = N_{test}$

Figure 5.15: SPIFT test damage detection for material B368-FV30, Test C-5 (V_{impact} = 156.44 m/s).

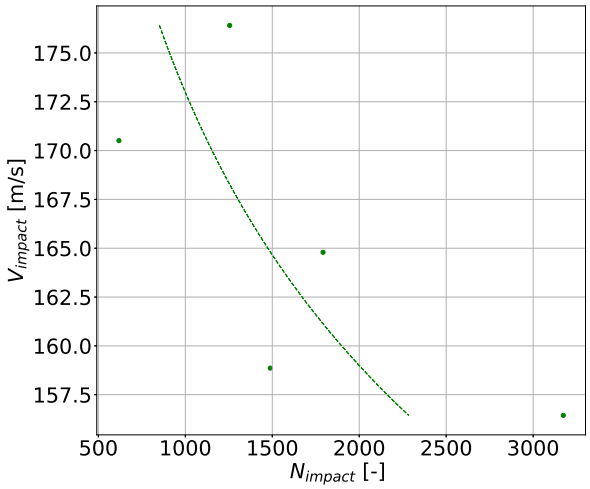

Figure 5.16: VN curve based on SPIFT analysis for material B368-FV30, overlaid with raw data.

B368-FV15

The test data for the fatigue test performed for material system B368-FV15 is visualised in Table 5.6. A relatively longer shooting interval is required compared to the higher filler volume case.

Table 5.6: Coating material B368-FV15 impact fatigue test data.

Test number [-]	V_{impact} **mean [m/s]**	V_{impact} **std [m/s]**	**Shot interval [ms]**	**Cooling [y/n]**	**Nshots incubation [-]**	**Total Nshots [-]**
D-1	175.19	2.82	6000	y	203	2945
D-2	170.41	1.5	5000	y	377	1696
D-3	166.75	3.22	5000	y	279	722
D-4	162.74	2.67	4000	y	2111	2754
D-5	155.77	1.78	4000	y	775	5719

In test D-1 (V_{impact} = 175.19 m/s), circular crack formation was seen followed by material loss and exposure of an air bubble below the surface. Figure 5.17 visualises the progression of damage. It can be noted that around the perimeter of the impact surface, similar stress levels are found following impact. However, the only notable failure was found at one specific location, even after the number of impacts was increased far beyond incubation at the point of failure. This indicates a defect-driven failure originating from an air bubble just below the surface of the test specimen.

(a) $N_{impact} = 0$ **(b)** $N_{impact} = N_{imcubation}$ **(c)** $N_{impact} = N_{test}$

Figure 5.17: SPIFT test damage detection for material B368-FV15, Test D-1 (V_{impact} = 175.19 m/s).

A similar behaviour is found in test D-2 (V_{impact} = 170.41 m/s), as visualised in Figure 5.18. Damage formed just outside the impact centre. Circular cracking is followed by material loss.

(a) $N_{impact} = 0$ **(b)** $N_{impact} = N_{imcubation}$ **(c)** $N_{impact} = N_{test}$

Figure 5.18: SPIFT test damage detection for material B368-FV15, Test D-2 (V_{impact} = 170.41 m/s).

The results of test D-3 (V_{impact} = 166.75 m/s) are visualised in Figure 5.18. Local damage formation initiated in the form of circular crack growth, similar to test D-1. Crack initiation was followed by material loss and the exposure of an air bubble below the surface.

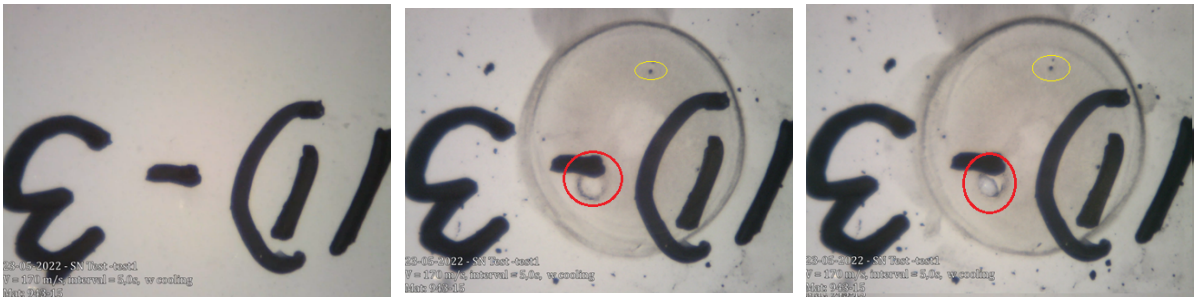

(a) $N_{impact} = 0$ **(b)** $N_{impact} = N_{imcubation}$ **(c)** $N_{impact} = N_{test}$

Figure 5.19: SPIFT test damage detection for material B368-FV15, Test D-3 (V_{impact} = 166.75 m/s).

For test D-4 the impact speed was lowered further (V_{impact} = 162.74 m/s) and the incubation period was significantly longer. Circular and local crack formation can be seen, followed by material loss and the exposure of holes. Figure 5.19 visualises the progression of damage and as can be seen in the figures, the damage was smaller in area when compared to damage found in tests number 1 and 2.

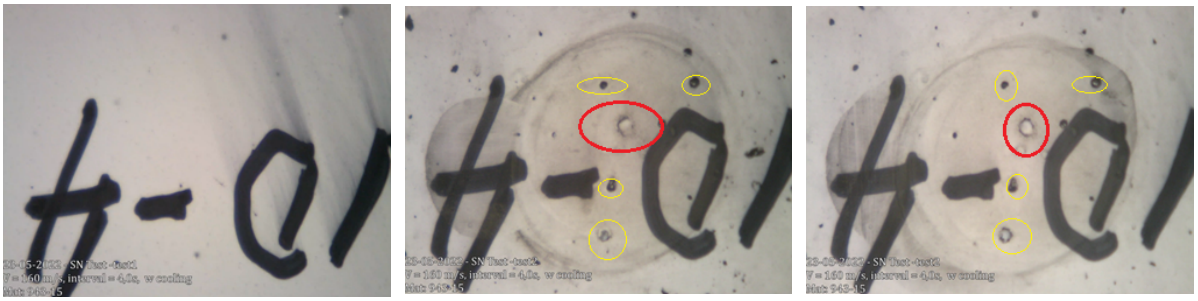

(a) $N_{impact} = 0$ **(b)** $N_{impact} = N_{imcubation}$ **(c)** $N_{impact} = N_{test}$

Figure 5.20: SPIFT test damage detection for material B368-FV15, Test D-4 (V_{impact} = 162.74 m/s).

Finally, test D-5 corresponds to the lowest impact speed (V_{impact} = 155.77 m/s). The damage progression is visualised in Figure 5.20. Failure was found around the perimeter of the impact surface, both on the left and right sides of the impact. Crack formation was seen, originating from small holes. The incubation point is taken as the point of crack initiation. Following initiation, the cracks increase steadily in size, following the perimeter of the impact surface.

The VN curve of material B368-FV15 is based on the point of incubation and is visualised in Figure 5.22. Similar to material B368-FV30, a substantial scatter can be seen between the final VN curve fit and the raw data points. Further discussion is provided below.

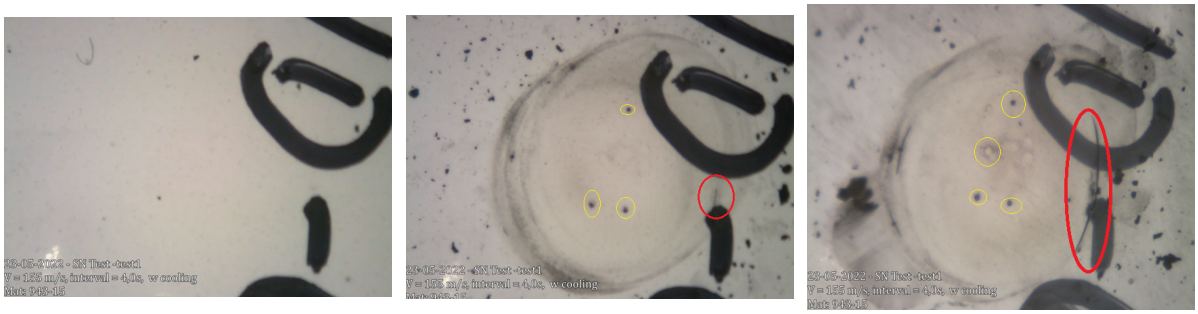

(a) $N_{impact} = 0$ **(b)** $N_{impact} = N_{imcubation}$ **(c)** $N_{impact} = N_{test}$

Figure 5.21: SPIFT test damage detection for material B368-FV15, Test D-5 (V_{impact} = 155.77 m/s).

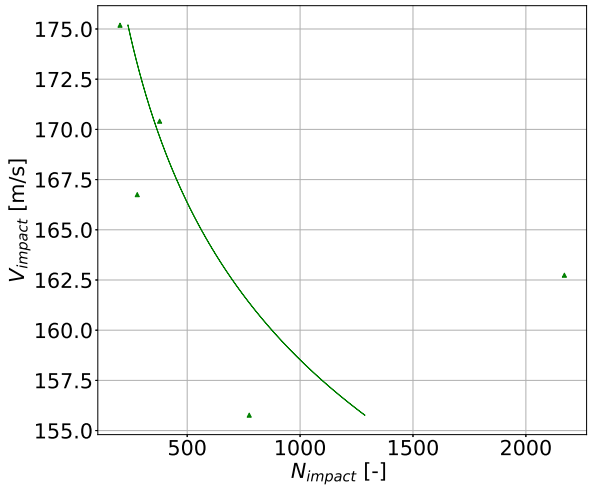

Figure 5.22: VN curve based on SPIFT analysis for material B368-FV15, overlaid with raw data.

5.3.4 Results of fatigue testing

Following the SPIFT fatigue testing campaign, a comparison can be made between material B368-FV30 and B368-FV15. Figure 5.23 visualises the final VN fit of both material systems, overlaid with raw data obtained from SPIFT testing. The R^2 value of the fit to the raw SPIFT data is presented. A similar slope in is seen for both curves, while material system B368-FV30 is shown to have a higher lifetime in SPIFT testing. However, due to a large spread in the data, combined with the low number of data points, a substantial uncertainty is expected in these results.

5.3.5 Conclusions and Recommendations for SPIFT testing

The preliminary AE and IR investigations provided insights into the impact behaviour of the different material systems. Binder system 357 shows relatively higher energy

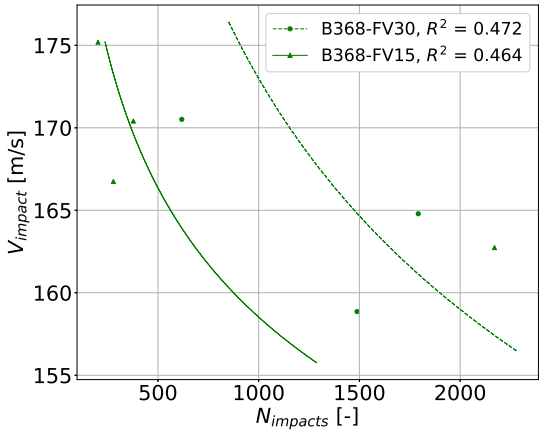

Figure 5.23: VN curve based on SPIFT fatigue testing for coating material B368-FV30 and B368-FV15, overlaid with raw SPIFT data.

dissipation when compared to binder system 368, which shows a more elastic response to impact. When comparing the filler volume fraction cases, opposite results were found. Binder 357 shows increased energy dissipation and heat generation upon impact for the high filler volume fraction case, while binder 368 shows the opposite behaviour.

The fatigue testing proved challenging. For binder system 357, a long return time to steady-state temperature following impact was found. This translated into high shooting intervals and long testing times. The high filler volume fraction case is characterised by defect-driven failure while the low filler volume case did not show any signs of damage. This difference in behaviour could be due to poor mixing of the filler material and clustering of the fillers in the high filler volume case. These clusters could be the cause of stress concentrations and the early exposure of defects as found in the test. For these reasons, The construction of a valid VN curve for binder system 357 is deemed unfeasible within the scope of this work.

Binder 368 showed a relatively faster return to the steady-state temperature of the test specimen, allowing for lower shooting intervals. Different types of failure were found and a distinction was made between defect-driven failure and failure due to repeated stress cycles. Fast exposure of air bubbles or impurities in the test specimen was disregarded in the determination of the incubation point. For both cases of filler volume fraction, the construction of a VN curve was possible, based on 5 individual data points. A comparison of the VN curves of the material systems shows the high filler volume fraction case to have a higher lifetime in SPIFT testing. Similar velocity dependence is found for both cases of filler volume fraction. It must be noted that the quality of the fit is low, with a substantial scatter between the individual data points and the final curve fit. The quality of the test specimens resulted in primarily defect-driven damage, complicating the comparison

between different test results. Furthermore, the damage detection method is prone to subjectivity, further increasing the uncertainty of the results. For these reasons, several recommendations can be made which aim to improve the reliability of the damage criteria.

Firstly, a higher standard should be set on the quality of the tested specimen. Air bubbles, cracks and impurities induced early failure in almost all tests. This obscured the visual damage detection method and caused inconsistency in the assessment of the individual tests. Furthermore, inconsistency in thickness was found between different specimens as well as within a single test specimen. The quality of the samples could be improved by improved mixing of the filler material in the coating system, application of vacuum post-casting or changing the production method from casting to spray application.

Secondly, the damage detection method could be reconsidered. The recording of the impact surface does allow for inspection of the impact surface over the full duration of the test. However, a certain subjectivity is included when manually assessing the damage. Research could be done in AI-based image analysis of the test result. This could improve the consistency and decrease manual labour requirements of the result interpretation. Furthermore, an initial investigation has been performed into the AE measurements of the full fatigue tests. The hypothesis was that damage in the specimen might change the signals picked up by the AE sensor. However, no pattern was discovered in the data, even after the application of a moving average filter. Further investigation can be done.

Thirdly, the automation of the SPIFT testing set-up can be improved which would allow for longer testing times. At the current state of the testing setup, human interference is required to keep the test running and gather all relevant data from the tests. Improved automation would allow for, for example, overnight testing which would greatly reduce the required time for material evaluation. This proved to be a limiting factor in this work. Increasing the number of tests for each impact velocity helps reduce the uncertainty of the final curve fit.

Finally, the SPIFT operates under the premise that there is a clear and well-defined relationship between impact velocity and the number of impacts until failure (VN). Physically this is a valid assumption with higher impact velocities corresponding to higher stresses in the material. This translates to decreased fatigue lifetimes. However, the material systems analysed showed more stochastic failure patterns with pre-existing defects causing the failure. This realisation leads to reconsideration of the current stress-based SN curve as damage criteria. However, additional material systems would need to be analysed to confirm this type of failure behaviour.

5.4 Stress Extraction

The SPIFT impact finite element model, described in subsection 3.2.3, is used for evaluation of the material systems described in Table 5.1. The visco-elastic properties as per

Tables A.1 to A.4 are used as input to the model for the respective material systems. The model is run for a range of V_{impact} of the rubber ball on the test specimen of [50,170] m/s and a linear fit is used on the data. The maximum stress amplitude experienced by the material is extracted from the analysis. Figure 5.24 visualises the results in terms of the signed Von Mises and Von Mises stress criteria.

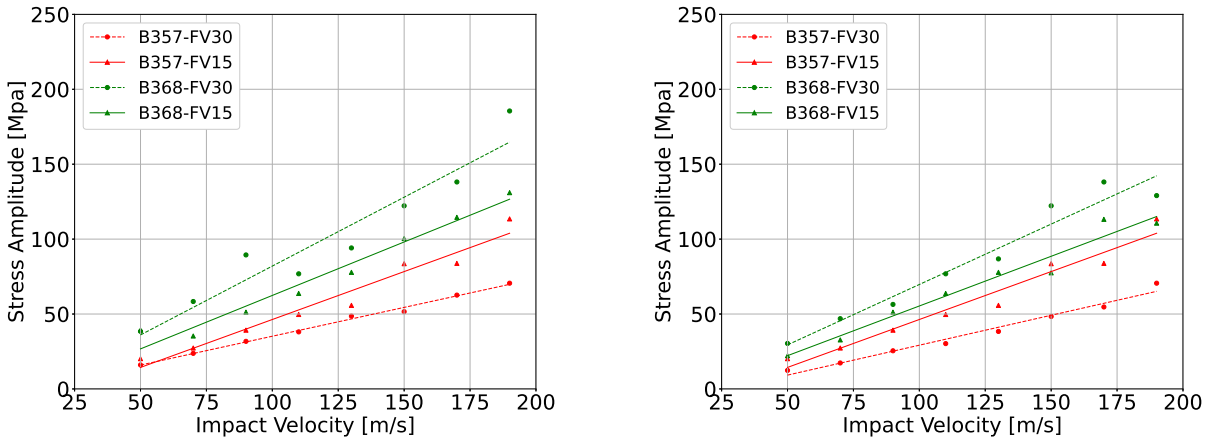

(a) Stress criteria: SVM

(b) Stress criteria: VM

Figure 5.24: Maximum stress amplitude for coating material B357-FV30, B357-FV15, B368-FV30 and B368-FV15, in terms of stress criteria SVM and VM, following FE simulation of SPIFT testing conditions (model described in subsection 3.2.3) for impact velocity [50-190] m/s.

It can be seen that binder system 368 experiences relatively higher stresses upon impact when compared to binder systems 357. This can be related to the differences seen in the $tan\delta$ master curve for high excitation frequencies (bottom plot of Figure 5.2) and previous observations made in the AE and IR preliminary analysis (Figures 5.5 and 5.6) . It could be concluded that binder system 368 shows a more elastic response to impact, with a smaller portion of the kinetic energy in the rubber ball being converted into heat. This difference translates into higher stresses for this binder system. The filler volume fraction shows opposite results between the binder systems, with a high filler volume fraction showing relatively higher stresses for binder 368 and relatively lower stresses for binder system 357. This is consistent with observations made by the AE and IR measurements.

5.5 SN curve

The coating material fatigue parameters are captured in terms of their respective SN curves, following methodology as in subsection 3.2.4. Combining the VN curves with the

stress states allows for the construction of the material's stress-based impact fatigue SN curve. Since no valid VN curve could be constructed for binder system 357, no SN curve can be set up for this binder system. The SN curve for binder system 368 is visualised in Figure 5.25. The fatigue parameters defining the SN curve for the different stress criteria A and B, are summarised in Tables 5.7 and 5.8 for coating system B368-FV30 and B358-FV15, respectively.

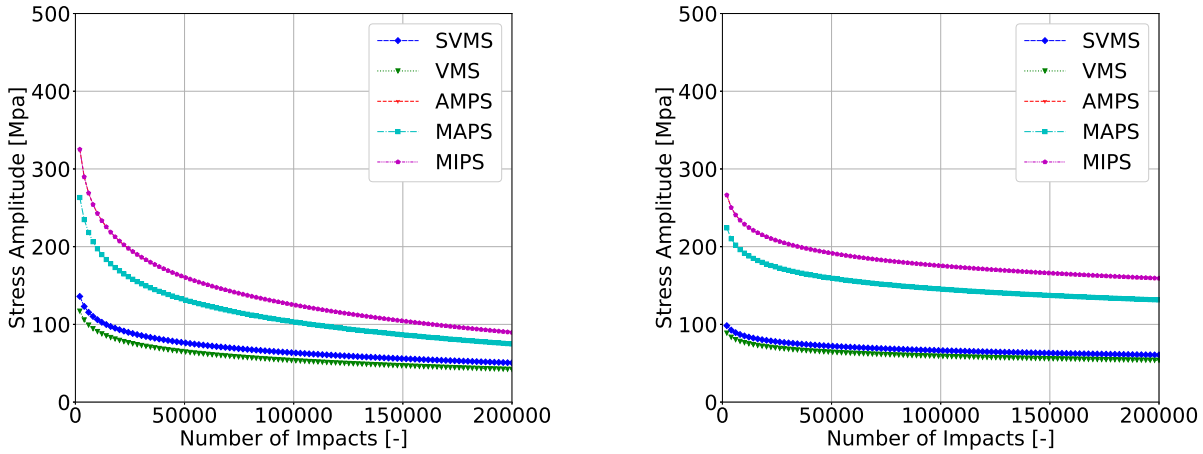

(a) B368-FV30 **(b)** B368-FV15

Figure 5.25: SN curve coating material B357-FV30, B357-FV15, B368-FV30 and B368-FV15.

Fatigue parameters A and B define the SN relationship for the respective material systems. A defines the slope of the respective curves, while B defines the intersection point with the y axis. Material B368-FV30 is shown to have generally more negative values for the slope (A) and higher values for B when compared to material B368-FV30. This means that for the stress limit for the low number of impacts material B368-FV15 has lower damage criteria compared to B368-FV30. This is the region of the SN curve where the raw SPIFT data is found. However, due to the difference in slope, there is an intersection point for which this flips and the damage criteria for material B368-FV30 becomes stricter.

The difference between the SN curves of the individual stress criteria originates from the differences in the magnitude of the different stress criteria, obtained in the SPIFT FE simulation (section 5.4). The principle stresses are generally higher in magnitude than the Von Mises stress options. When choosing one of these options for the lifetime prediction, the loading conditions utilise the same stress criteria.

Table 5.7: SN curve parameters B368-FV30.

Stress Criteria	A [Mpa]	B [Mpa]
VM	-18.60	277.51
SVM	-16.31	241.19
AMPS	-51.26	715.36
MAPS	-41.01	575.34
MIPS	-51.26	715.34

Table 5.8: SN curve parameters B368-FV15.

Stress Criteria	A [Mpa]	B [Mpa]
VM	-7.48	155.76
SVM	-6.96	142.14
AMPS	-21.25	429.35
MAPS	-18.38	365.13
MIPS	-21.25	429.35

5.6 Conclusions

The analysis of the materials master curves reveals the differences in the visco-elastic properties of the individual material systems. The binder type is shown to dominate the visco-elastic behaviour of the coating materials. Binder system 357 is shown to have larger visco-elastic damping for the high-frequency range ($>10^5$ Hz), relevant for impact analysis. This difference is confirmed in the AE and IR SPIFT analysis of the material systems, with binder 357 showing increased heat generation and less elastic response upon impact, when compared to binder system 368. This resulted in relatively lower stresses in the material when subjected to SPIFT.

As for the comparison of the filler volume fraction, relatively lower differences are seen in the visco-elastic properties. In the high-frequency range, the high filler volume fraction case shows relatively lower damping for both binder systems. However, in the IR and AE analysis during SPIFT testing, opposite behaviour is found between the binder systems. For binder system 368, the high filler volume fraction case shows relatively lower heat generation and a more elastic response, in line with the observations made in the master curves. However, for binder system 357, an opposite trend is seen. This could be explained by the uncertainty of the extremes of the master curve s, introduced by the shifting of raw DMTA data. This uncertainty means that the differences observed due to the filler volume fraction are due to inaccuracies in the shifting of the raw data, rather than capturing the actual material's behaviour. Furthermore, the SPIFT test could be repeated with different material specimens, reducing the uncertainty of the test results.

In impact fatigue testing, it was concluded that the construction of a valid VN curve is not feasible within this work for both filler volume cases of binder 357. A valid damage criterion has been set up for both cases of filler volume fraction for binder 368. The high filler volume case is shown to provide the highest lifetime over the full range of tested impact velocities in SPIFT. Combining this result with the stress states experienced during SPIFT analysis allows for the construction of the stress-based SN curve damage criteria, which will be used in subsequent rain erosion performance evaluation.

CHAPTER 6
RET Prediction and Validation

The RE lifetime tool described in subsection 3.3.3 and analysed in Sections 4.2 and 4.3 is tuned towards recreating RET whirling arm conditions and utilised for the evaluation of the materials systems described in chapter 5. The RET lifetime of the material systems is predicted and validated with RET whirling arm experimental data.

The single droplet impact case is evaluated and compared for all material systems as discussed in section 6.1. This is followed by the full RET lifetime prediction presented in section 6.2. The whirling arm experimental validation data is presented in section 6.3 and compared to the lifetime prediction in section 6.4. Finally, the differences between the material systems will be discussed in section 6.5 and linked to their respective material properties. When possible, concluding remarks on desirable material properties, in terms of RET lifetime will be made.

6.1 Single Droplet Impact

The droplet impact is simulated for the respective material systems using the simulation parameters defined in Table 6.1. Furthermore, for each material system, the Yeoh-prony parameters defining the visco-elastic material properties as defined in Tables A.1 to A.4 are used for the material specification. Using pressure profiles representing the droplet impact input, the stress field along the pre-defined paths is obtained and will be used in the subsequent RE lifetime prediction tool. As a means of comparison between the material systems, both the pressure profiles and stress field are further analysed.

Table 6.1: Droplet impact simulation parameters.

Parameter	Unit	Value
Density	$[\frac{kg}{m^3}]$	1100
Number of Paths	[-]	15
Depth Path N0. 1	[mm]	0.001
Path Spacing	[mm]	0.02
Path length	[mm]	2.5
Simulation Time	[s]	$1.25{\cdot}10^{-5}$
Sampling Interval	[s]	$1.0{\cdot}10^{-7}$
Droplet Diameter	[mm]	2.36
Impact Velocity	[m/s]	100, 110, 120, 130

6.1.1 Pressure profile comparison

The 2D-axisymmetric explicit finite element model as discussed in subsection 3.3.2 is used for the evaluation of a single droplet impact on the coating materials. The input to this model are the pressure profiles representing the droplet impact event and are visualised in Appendix C, Figures C.1 to C.4 for the material systems under investigation. The pressure profiles are a function of their respective visco-elastic properties. The maximum pressure is extracted for the individual material systems and compared. Figure 6.2 visualises the results.

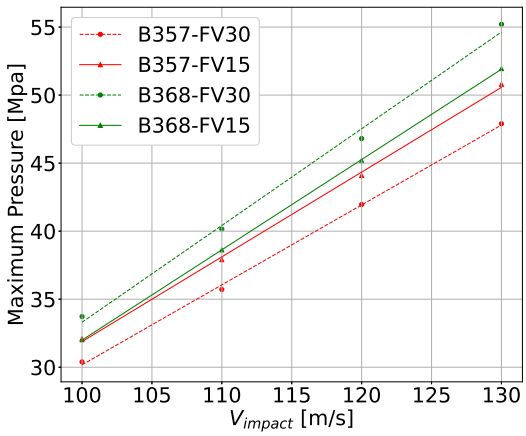

Figure 6.1: Pressure profile comparison in terms of maximum pressure for coating material B357-FV30, B357-FV15, B368-FV30 and B368-FV15 for V_{impact} = [100-130] m/s.

Binder system 368 shows higher maximum pressure values when compared to binder system 357. This can be related to the lower $tan\delta$ values for high strain rate loading cases. Lower values of $tan\delta$ indicate a more elastic response which can be translated into higher pressures upon impact for droplet impact cases. Analysis of the filler volume fraction shows opposite results between the binder systems. For binder system 357, a higher filler volume fraction shows lower values of maximum pressure, while for binder system 368 an opposite trend is seen. This behaviour is in line with previous observations made in SPIFT AE and IR analysis, described in subsection 5.3.2.

6.1.2 Maximum Stress Amplitude

The stress field as obtained from the impact simulation is analysed and the absolute maximum stress amplitude experienced by the material is extracted for each impact velocity and material system. For all points along the individual paths, the maximum stress amplitude in terms of the chosen stress criteria is calculated by Equation 6.1. This provides the maximum stress amplitude experienced by each analysis point. The absolute

maximum value of this analysis is then extracted for comparison between the material systems.

$$\sigma_{ampl} = \frac{\sigma_{max} - \sigma_{min}}{2} \tag{6.1}$$

Figure 6.2 visualises the maximum stress amplitude as experienced by the individual materials systems, overlaid with a linear fit to the data points. In terms of the Von Mises stress criteria, higher stresses are experienced by the materials with binder system 368, compared to binder system 357. For the signed Von Mises stress criteria, varying results are found. The stress states are a function of the pressure profiles, varying in time and space, as well as the visco-elastic material properties. The stress states experienced during SPIFT testing conditions, described in section 5.4, are more suitable for comparison since all materials are subjected to equal loading conditions. Here, the variation in pressure profile shape and magnitude is included.

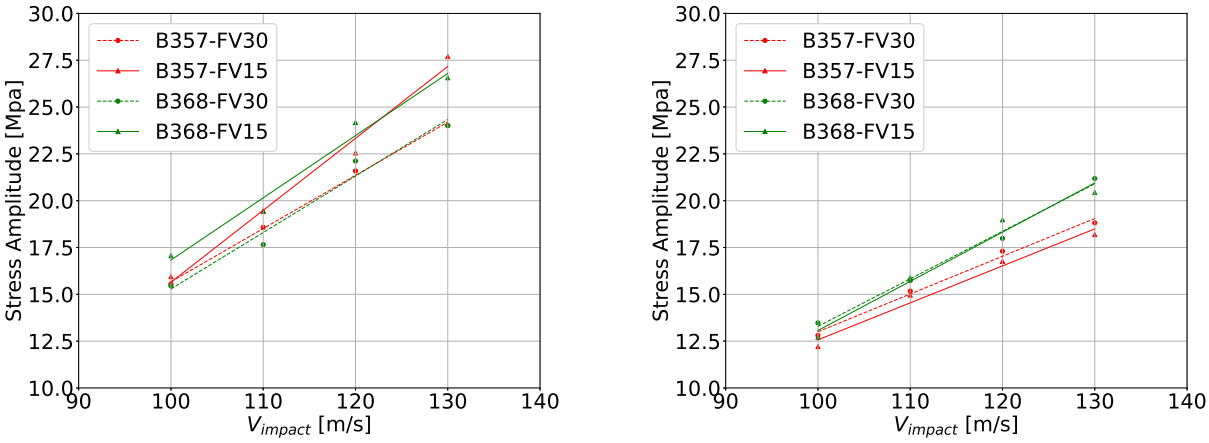

(a) Stress criteria: SVMS

(b) Stress criteria: VM

Figure 6.2: Maximum stress amplitude for coating material B357-FV30, B357-FV15, B368-FV30 and B368-FV15, in terms of stress criteria SVMS and VM, following droplet impact for impact velocities [100-130] m/s.

6.2 RET Lifetime Prediction

The RE lifetime prediction code, described in subsection 3.3.3, is used for the prediction of RET performance of coating materials B368-FV30 and B368-FV15. The parameters as defined in Table 6.2 are used in the model. The droplet impact simulation as described in section 6.1 is used for the determination of the stress states in the material. Furthermore, the stress amplitude conversion method, described in subsection 4.3.2 is applied.

Table 6.2: Input parameters for the RE lifetime prediction tool for coating material B368-FV30 and B368-FV15.

Parameter	Symbol	Unit	Value
Impact Velocity	V_{impact}	[m/s]	100, 110, 120, 130
Simulation Time	t_{sim}	[s]	1000
Number of runs	N_r	[-]	3
Droplet diameter	D_d	[mm]	2.4
RET intensity	I	[mm/h]	30
Droplet free-fall velocity	v_{drop}	[m/s]	2.5
Damage Criterion	DC	[-]	SVM

Figure 6.3 visualises the RET lifetime prediction for material B368-FV30 and B368-FV15 in terms of specific impacts until failure vs impact velocity. As can be seen, material B368-FV15 is predicted to have a higher lifetime compared to material B368-FV30. This prediction is contradicting results seen in the SPIFT test, where material B368-FV30 is shown to have a higher lifetime.

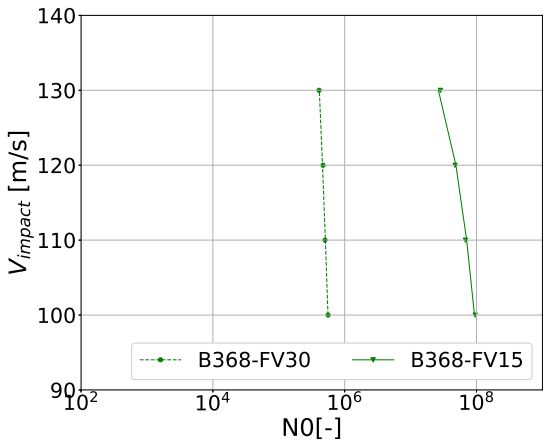

Figure 6.3: RET lifetime prediction for coating material B368-FV30 and B368-FV15, in terms of specific impact N_0 vs impact velocity V_{impact}.

This contradicting result can be explained by analysing the damage criteria of both material systems, for which Figure 6.4 can be used. As already discussed in section 5.5, material B368-FV15 is found to have lower values for both A and B, compared to material B368-FV30. This results in the region where the SPIFT test is performed (low number of impacts until failure), the damage criteria for material B368-FV15 are lower than for material B368-FV30. This is shown in plot (a) of Figure 6.4, where the SN curve of the signed Von Mises stress criteria is visualised for both B368-FV30 and B368-FV15. The

curves are shown to intersect at a stress level of about 80 Mpa. Furthermore, the data points originating from the VN curve on which the final fit is based are visualised in the figure.

Plot (b) of Figure 6.4 visualises a histogram of a typical stress distribution experienced by the coating material when analysed by the RE lifetime prediction tool when used for RET lifetime prediction. From this stress distribution, it can be concluded that damage is evaluated in the low stress, high number of impact regions of the SN curve. A substantial extrapolation of the damage criteria is required. The difference in slope of the SN curve means that the damage criteria of B368-FV30 are stricter in this region, and thus a relatively lower lifetime is found.

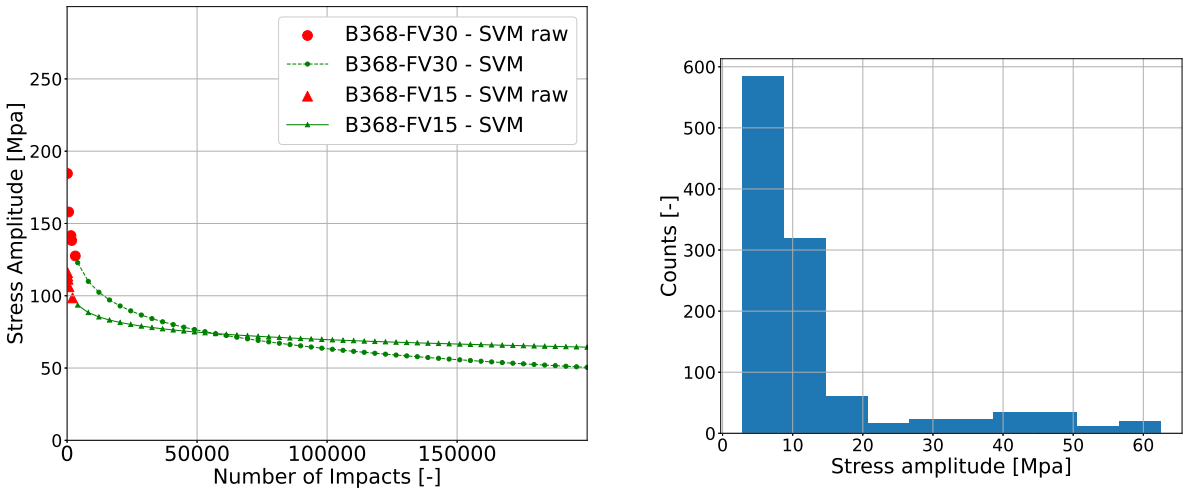

(a) SN curve comparison B368-FV30 vs B368-FV15

(b) Typical stress history (SVM) experienced in the RET lifetime prediction

Figure 6.4: Stress criteria analysis for the RE lifetime prediction tool.

This result leads to the conclusion that the current damage criteria might not be relevant for the lifetime predictions in their current form. In the SPIFT test, high-velocity impacts, corresponding to relatively high stresses are analysed. In the lifetime prediction, lower stress values are experienced and thus extrapolation of the damage criteria is required, introducing a great deal of uncertainty. This means the damage criteria used in the RE lifetime tool might not capture the material's fatigue behaviour realistically. In the current work, this conclusion translates into a mismatch between the SPIFT results and the final lifetime prediction of the material systems.

SPIFT testing could be conducted at lower impact velocities, bringing the stress levels closer to those experienced in the lifetime prediction. However, as discussed in chapter 5, this is not feasible with the current SPIFT testing set-up. Therefore, alternative testing methods could be explored.

6.3 RET whirling arm results

The material systems are subjected to RET whirling arm analysis of which the results are used for validating the presented work. The analysis has been performed by Nicolai Frost-Jensen Johansen, development engineer at DTU Wind Energy. Figure 6.5 visualises the raw whirling arm data in terms of specific impact vs impact velocity, overlaid with a linear fit. The results for each material system are presented, including the R^2 value of the final fit to the raw whirling arm data.

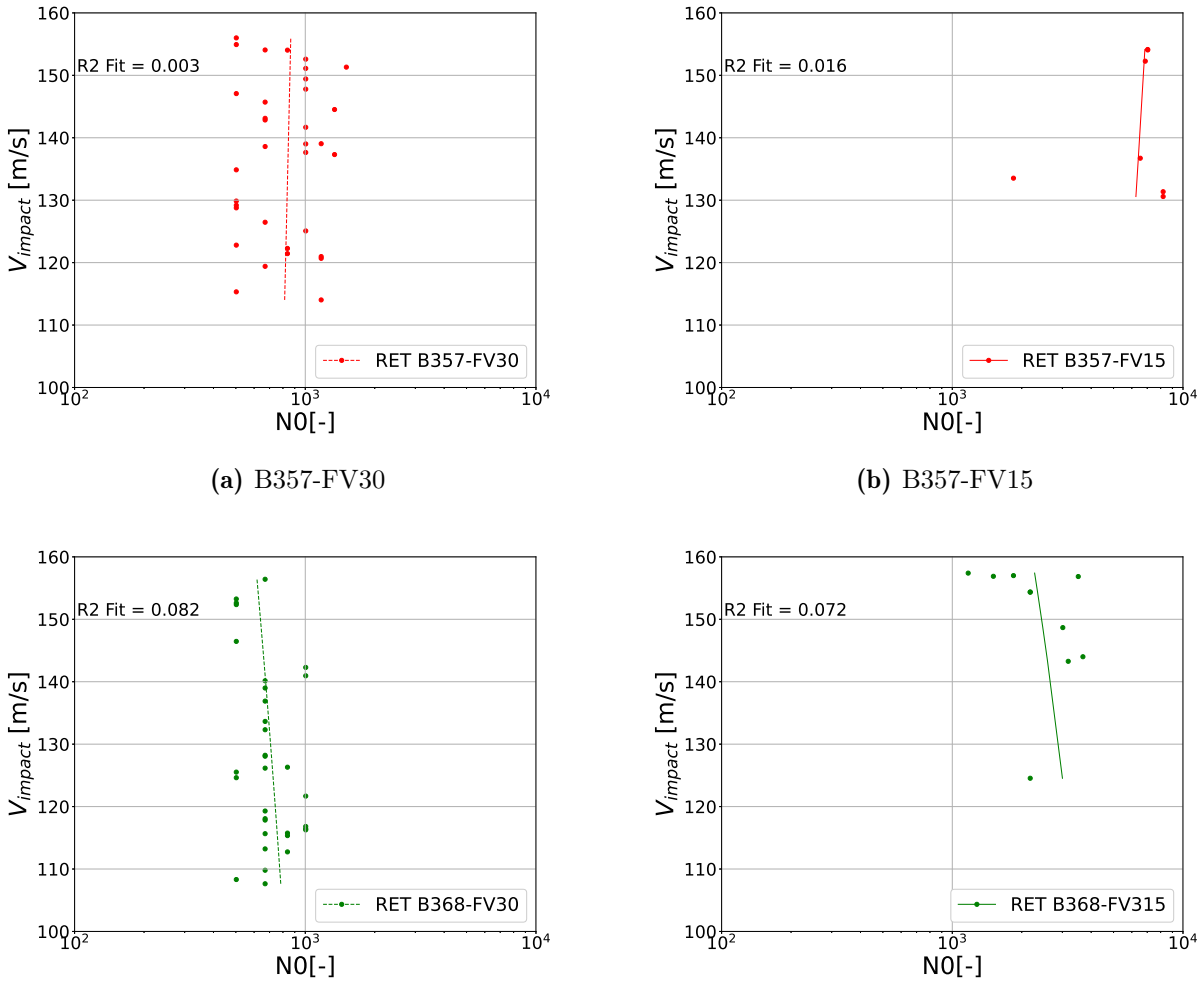

(a) B357-FV30

(b) B357-FV15

(c) B368-FV30

(d) B368-FV15

Figure 6.5: RET whirling arm data for coating materials B357-FV30, B357-FV15, B368-FV30 and B368-FV15.

The linear fit to the individual material systems is characterised by a low R^2 value (<0.1),

indicating a substantial scatter in the data. This scatter originates from defect-driven failure when subjected to the RET. This type of behaviour can especially be recognised in binder system 357 where a negative slope is found for the linear fit to the RET data, for both cases of filler volume fraction. This indicates fully defect-driven failure of the coating systems. The materials lifetime shows more of a stochastic pattern, rather than velocity dependence. The R^2 indicates a substantial uncertainty in the final fit and has to be considered in further analysis. Finally, the data of materials B357-FV30 and B368-FV30 are characterised by a low number of data points. The whirling arm test was cut short and no relevant failure was found in this region of impact velocity, for these material systems. This further decreases the confidence in the final result for these material systems.

Figure 6.6 visualises the comparison of the individual material systems. The largest difference can be seen due to the filler volume fraction. The low filler volume fraction case shows a higher lifetime for both binder systems. This is noteworthy since the binder system dominates the material's visco-elastic behaviour. This translates into the binder system having the largest effect on the behaviour of the material upon impact and subsequent stress states in the material. This further indicates defect-driven failure in the RET test. Clustering of the fillers can cause stress concentrations, initiating failure. This is more likely for the high filler volume fraction case.

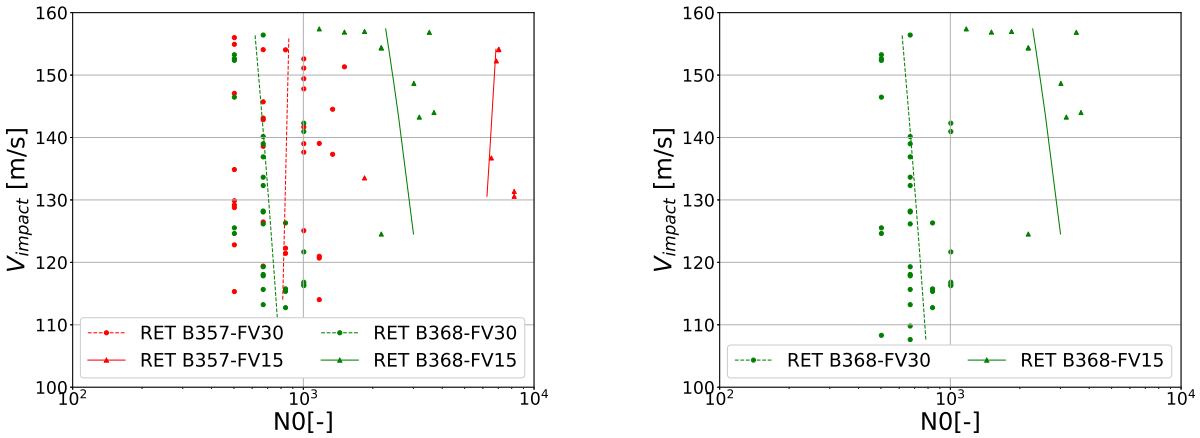

(a) Material comparison

(b) Binder 368

Figure 6.6: RET whirling arm data for binder system 357 and 368, in terms of specific impacts vs impact velocity.

Comparison of the binder systems shows that binder 357 exhibits improved lifetime, compared to binder system 368. However, it must be noted here that the data points for the individual material systems overlap. This observation, combined with the low R^2 value

of the individual material fits, does not allow for a confident conclusion when comparing both binder systems. The statistical uncertainty has to be considered. Zooming in on binder system 368, plot (b) of Figure 6.6, a higher lifetime can be seen for the low filler volume fraction case in the final fit to the data.

It must be noted that the low filler volume material systems (B357-FV15 and B368-FV15) have been tested with with three layers of the material system, while for the high filler volume case (B357-FV15 and B368-FV15), only one layer is applied. This is due to a last-minute direction change within the DURALEDGE project over which the student had no influence. This is expected to effect the results, decreasing confidence in the conclusions made on relative material performance.

6.4 Result validation

The RET whirling arm data is used for validation of the lifetime predictions of coating systems B368-FV30 and B368-FV15. Figure 6.7 visualises the comparison.

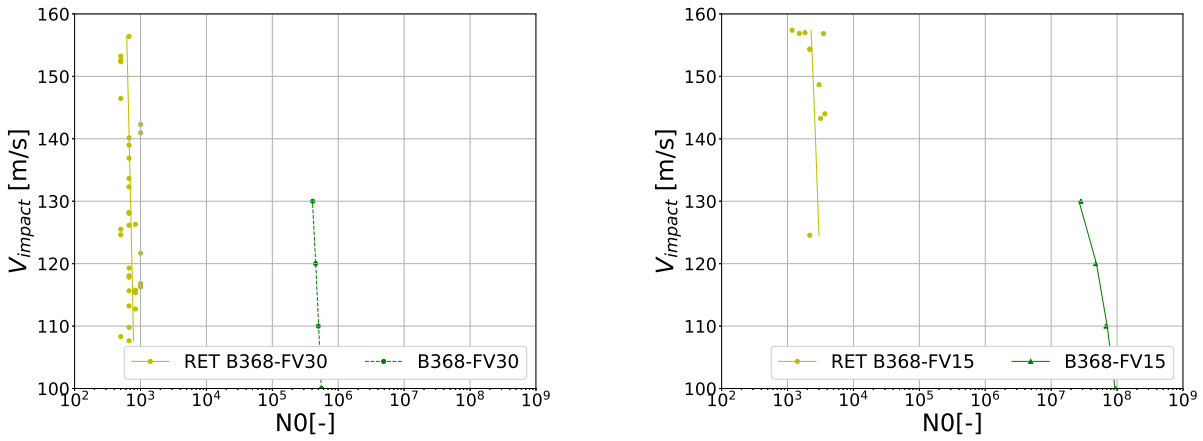

(a) B368-FV30

(b) B368-FV15

Figure 6.7: Validation of RET lifetime prediction with RET whirling arm data for coating material B368-FV30 and B368-FV15, in terms of specific impacts vs impact velocity.

It can be noted that the validation data and lifetime prediction are not fully in the same range of impact velocities. The RET whirling arm test velocity range equals approximately [100,160] m/s, while the lifetime prediction has been performed for velocities between [100,130] m/s. For material B368-FV30, the majority of the data points are clustered around V_{impact} = [100,130] m/s, corresponding to the impact velocities of the lifetime prediction. However, for material B368-FV15 no data points are found in this

range of impact velocities.

For both material systems, the velocity dependence of the lifetime prediction is shown to correspond fairly well with the validation data. However, a large absolute error is found for the full range of impact velocities investigated. The lifetime prediction is shown to severely overestimate the coating's lifetime. Further discussion is provided below.

6.5 Conclusions

A RET lifetime prediction has been performed for material systems B368-FV30 and B368-FV15 and this result has been validated with RET whirling arm data. For material systems B357-FV30 and B357-FV15, a full lifetime prediction was not performed due to issues with the determination of valid damage criteria during SPIFT fatigue testing. However, the RET whirling arm data has been analysed and various analyses leading up to the full lifetime prediction have been performed for these material systems.

The binder type has been shown to dominate the visco-elastic behaviour of the coating materials. Binder system 357 is shown to have larger visco-elastic damping for the high-frequency range ($>10^5$ Hz), relevant for impact analysis. This results in the maximum pressure experiences during a droplet impact being relatively lower for binder system 357 and subsequently, lower stresses. Furthermore, the RET whirling arm data reveals that binder 357 shows a slightly higher lifetime for both cases of filler volume fraction.

As for the comparison of the filler volume fraction, relatively lower differences are seen in the visco-elastic properties. In the high-frequency range, the high filler volume fraction case shows relatively lower damping for both binder systems. A comparison of the RET whirling arm data reveals the filler volume fraction to have a larger effect on the coating lifetime, compared to the binder system. The high filler volume fraction case is shown to have a relatively lower lifetime, compared to the low filler volume fraction case. This indicates possible clustering of the fillers in the coating material, causing stress concentrations and defect-driven failure.

A full RET lifetime prediction has been performed for both filler volume levels of binder system 368. During SPIFT impact fatigue analysis, B368-FV30 shows a lower lifetime over the full range of tested impact velocities, compared to material B368-FV15. This comparison is captured in the VN curve of both material systems. Translating this to the lifetime prediction, an opposite result is found: B368-FV15 is predicted to have the highest lifetime. This difference originates from the damage criteria of both materials, expressed in the SN curve. The stress range the coating material is subjected to in the RET lifetime prediction tool is substantially lower than the stresses experienced during SPIFT analysis. This means a substantial extrapolation is required of the SN curve. Due to the difference in slopes of the two material systems, the SN curve intersects and the damage criteria of B368-FV30 become stricter, and the material is therefore expected to

fail before material B368-FV15.

During the validation of the lifetime prediction, it is revealed that the relative lifetime of coating systems B368-FV30 and B368-FV15 is captured. However, the difference in the RET whirling arm data originates from defect-driven failure in the high filler volume fraction case. This difference is not captured by the models. The relative difference in the lifetime prediction rather comes from an extreme extrapolation of the damage criteria leading to inconsistent results with the SPIFT VN curve. Therefore the lifetime prediction model cannot be assumed to accurately predict the relative performance of the two coating systems. A solution could be proposed by forcing an equal slope in the determination of the SN curve. However, it should be considered to what extent this is a realistic solution. The lifetime prediction would become consistent with the SPIFT VN curve, however, inconsistency would still be seen when comparing the relative lifetime to the RET validation data.

CHAPTER 7

Conclusions and Recommendations

7.1 Conclusions

This work presented an analysis of the pre-established rain erosion framework, developed within the DURALEDGE research project of DTU Wind Energy. Furthermore, it has been used for the evaluation of four novel leading-edge coating systems. The research evolved around the following research objective:

To investigate potential wind turbine blade leading edge protective solutions by utilising the existing DTU Wind Energy DURALEDGE framework and put forth improvements for the computational evaluation of leading-edge erosion.

To meet the above research objective, several research goals were set out. These are listed and reflected upon below.

RG 1 - To investigate the current state-of-the-art of the DTU Wind Energy DURALEDGE framework, by analysing a novel coating material using the existing workflow.
This work provides an overview of the lifetime prediction workflow for novel leading-edge coating systems, as presented in chapter 3. This analysis provided the student with an introduction to the working mechanisms of the workflow and subsequently allowed for evaluation of the methodology.

RG 2 - To put forth improvements to the existing workflow by critically analysing and evaluating the individual segments of the workflow.
Several analysis methods have been reflected upon spanning the full workflow. Firstly, the processing of DMTA data to master curves, expressing the visco-elastic properties of the coating systems has been automated. This to reduce user-introduced subjectivity in the final curve and reduce construction time. Furthermore, analysis has been performed on the damage criteria based on SPIFT testing. A difference in stress levels between SPIFT analyses and the subsequent RE lifetime tool is found. This results in an extreme extrapolation of the damage criteria, which introduces inaccuracies in the workflow. Recommendations are made for updating the damage criteria in the RE lifetime tool which aim to reduce these uncertainties. Finally, the RE lifetime tool is investigated which is further elaborated upon in RG-3.

RG 3 - To investigate the velocity dependence of the current state-of-the-art lifetime prediction obtained by the DTU Wind Energy DURALEDGE framework.
The velocity dependence of the state-of-the-art lifetime prediction was underestimated, at the start of this work. This behaviour is tracked to numerical noise, originating from the single droplet impact simulation, dominating the damage calculation in the RE lifetime prediction tool. Two alternative solutions methods have been proposed and investigated, which aim to solve this issue. The minimum stress amplitude method (MSA) filters out any unrealistic stress fluctuations before the damage calculations, however, no physical basis is found for the magnitude of the stress filter. The stress amplitude conversion (SAC) method reduces each impact case to a single stress wave of which the amplitude is determined by the extremes of the stress experienced over the full length of the impact. This is similar to mythology used in the determination of the stress criteria and represents the accepted renewed evaluation method. By utilising this renewed method, the velocity dependence of the lifetime prediction is shown to have improved and brought closer to the trend seen in the validation data.

RG 4 - To investigate the effect of binder type and micro-filters in novel leading-edge coating materials, by performing a lifetime analysis of different types of novel coating material systems
Four coating systems have been analysed, utilising two different binder systems (357 and 368) and two levels of filler volume fraction (15% and 30%). The binder system is found to dominate the visco-elastic properties of the materials. Relatively higher damping values in the relevant excitation frequency domain ($>10^5$ Hz) are found in binder system 357. This results in greater heat generation upon impact and less elastic response for this binder system. A greater portion of the impact energy is absorbed by the material. This translates in lower pressures experienced during a droplet impact and subsequently, lower stresses through the material. In the RET whirling arm validation data, indications are seen that this high damping system shows improved performance compared to the low damping system (binder 368).

Both binder systems show opposite behaviour with respect to the filler loading. For binder system 357 (high damping), an increased filler loading results in higher damping. For binder system 368 (low damping), an opposite trend is seen. In terms of RET performance, the low filler volume case shows an improved lifetime for both binder systems as seen in the RET whirling arm validation data. This can be traced to defect-driven failure during RET testing. Clustering of the filler particles leads to stress concentration and failure. The relative performance of both filler volume cases for binder 368, is captured by the computational workflow. However, it must be noted here that this is opposite to the lifetime found in SPIFT analysis.

All in all, indications are seen that, for these material systems, higher damping combined with a low filler volume provides the highest rain erosion resistance.

7.2 Recommendations

Reflection on the research goals reveals the research objective of this work has been met. The pre-established workflow has been analysed and improved and four novel coating systems have been analysed utilising this workflow. However, several assumptions and simplifications are made throughout this work and within the rain erosion computational workflow. Here, some of these are reflected upon and recommendations for further work are made.

Reduce uncertainty in the high-frequency range of the master curve.
The extreme frequency range (relevant for impact) of the coating materials master curve is prone to the uncertainty introduced by extrapolation of the experimental DMTA data, based on the time-temperature superposition principle. This uncertainty is further increased in the subsequent model calibration. This was recognised in discrepancies between the material's master curve tanδ values and observations made in SPIFT analysis with IR and AE measurements. Ideally, the DMTA test would be performed at the relevant frequency temperature values however this is beyond the capability of state-of-the-art DMTA equipment.

Evaluate the impact fatigue properties at similar stress levels as experienced in rain erosion cases.
The largest source of uncertainty in the workflow lies in the damage criteria based on SPIFT analysis. Due to limitations of the current SPIFT testing set-up, all tests have been performed at relatively high impact speeds, corresponding to high stresses in the impact material. These stresses are substantially higher than the stresses experienced by the coating material when subjected to the RE lifetime prediction tool, as used for the RET lifetime prediction. This leads to an extreme extrapolation of the damage criteria, introducing uncertainty in the lifetime prediction. In future work, alternative impact fatigue testing could be explored such as the water jet tester.

Improve the robustness of the workflow
The full lifetime prediction could only be performed for two out of four material systems. This means the robustness of the workflow, and especially the damage criteria, should be improved. This could be done by updating the current SPIFT set-up and reduce the required human-interference during impact fatigue testing. Furthermore alternative impact fatigue test methods can be explored, which utilise a higher technology readiness level (TRL) than the SPIFT.

Improve the modelling of a single droplet impact case by including realistic boundary's in the model.
In the single droplet impact simulation, the coating material is currently modelled as an infinitely thick material and the effect of stress wave bouncing is disregarded. Including the putty and glass fibre structure, typically found below a leading-edge coating material, will allow for more realistic stress propagation.

Include lateral jetting in the damage evaluation of the RE lifetime prediction tool.
The current state-of-the-art only considers the normal forces which are applied to the coating material due to the impact event. However, in RET whirling arm testing, the shear forces associated with lateral jetting are a known source of damage, which for now are disregarded.

Consider material defects in the modelling of novel coating materials.
In the RET whirling arm validation data as well as the SPIFT analysis, defect-driven damage was found to be the primary source of damage. For now, this is only included in the workflow through the VN curve expressing the SPIFT lifetime, which includes defect-driven damage data points. In the stress state determination and subsequent damage evaluation, homogeneous material is assumed. Inclusion of defects in the FE models would allow for the assessment of the effect of defects on the stress state and subsequently, damage formation within the material.

APPENDIX A

Appendix A - Materials

A.1 B357-FV30

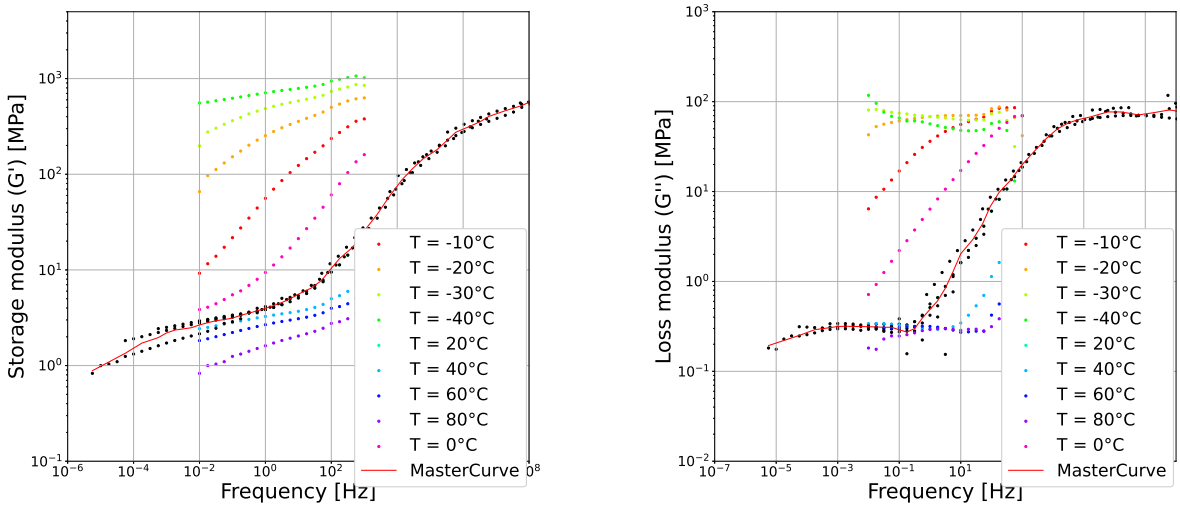

(a) Storage modulus (G')

(b) Loss modulus (G")

Figure A.1: Master-curve construction of coating material B357-FV30 before and after applying horizontal shifts to individual DMTA frequency sweeps.

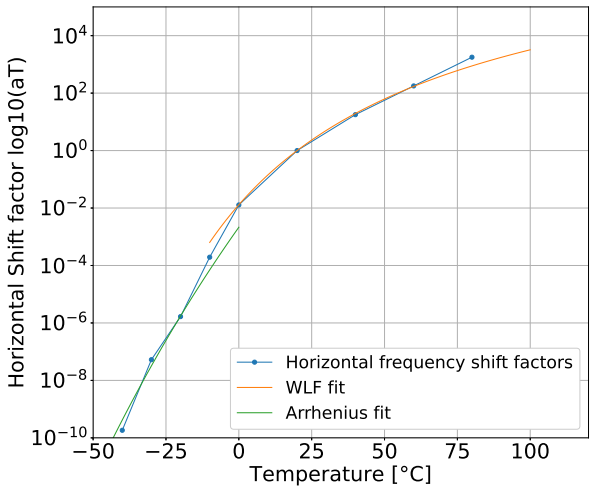

Figure A.2: Coating material B357-FV30 raw shift factor data, overlaid with WLF and Arhenius fit .

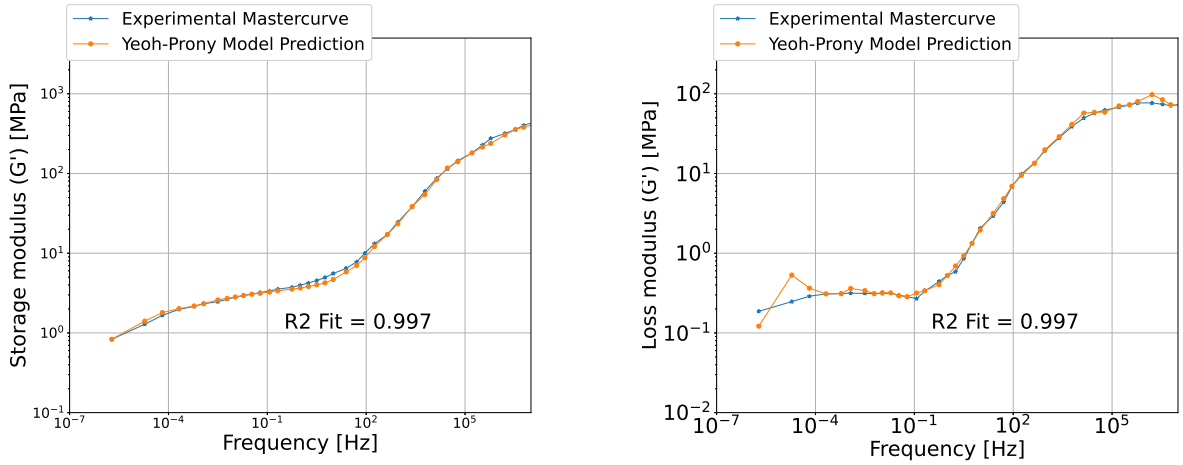

(a) Storage modulus (G')

(b) Loss modulus (G')

Figure A.3: Material model calibration of coating material B357-FV30 with Yeoh hyperelastic model and Prony series approximation to DMTA based mastercurve.

Table A.1: Yeoh hyperelastic model and Prony series approximation model parameters for coating B357-FV30.

Hyperelastic Model: Yeoh parameters			
C10 [Mpa]	3.72E+08	**D1** $[\frac{1}{Mpa}]$	2.68e-10
C20 [Mpa]	0	**D2** $[\frac{1}{Mpa}]$	0
C30 [Mpa]	0	**D3** $[\frac{1}{Mpa}]$	0

Viscoelastic Model: Prony Parameters					
i	g_i **[Pa]**	τ_i **[ms]**	**i**	g_i **[Pa]**	τ_i **[ms]**
1	0.00133088	10000	**9**	0.038321	0.0001
2	0.00042964	1000	**10**	0.121444	1.00E-05
3	0.00076076	100	**11**	0.119772	1.00E-06
4	0.00057657	10	**12**	0.211537	1.00E-07
5	0.00052704	1	**13**	0.104085	1.00E-08
6	0.00068287	0.1	**14**	0.194178	1.00E-09
7	0.00297113	0.01	**15**	0.09655	1.00E-10
8	0.0135046	0.001	**16**	0.092229	1.00E-11

A.2 B357-FV15

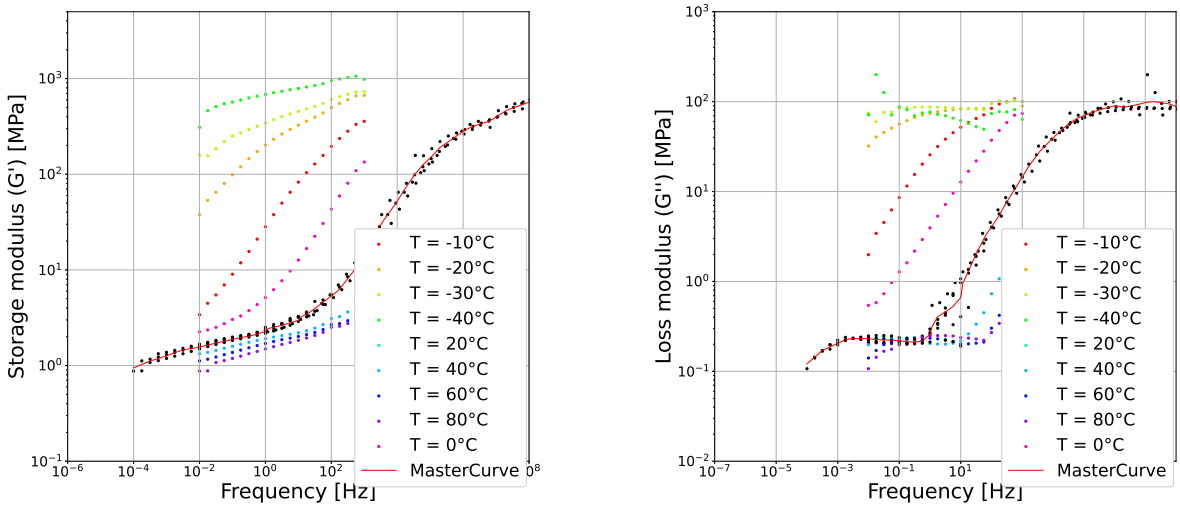

(a) Storage modulus (G')

(b) Loss modulus (G")

Figure A.4: Master-curve construction of coating material B357-FV15 before and after applying horizontal shifts to individual DMTA frequency sweeps.

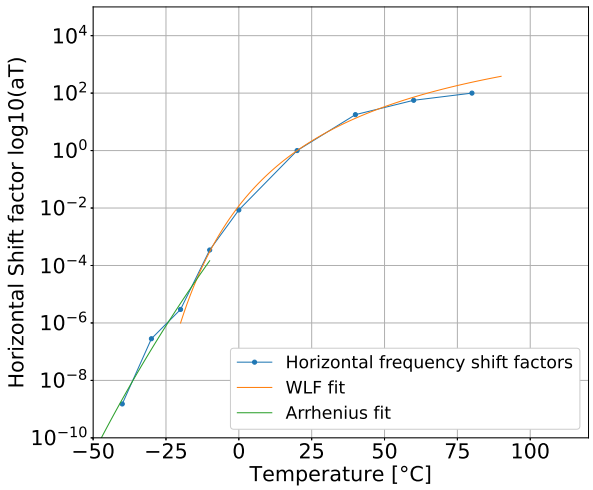

Figure A.5: Coating material B357-FV15 raw shift factor data, overlaid with WLF and Arhenius fit .

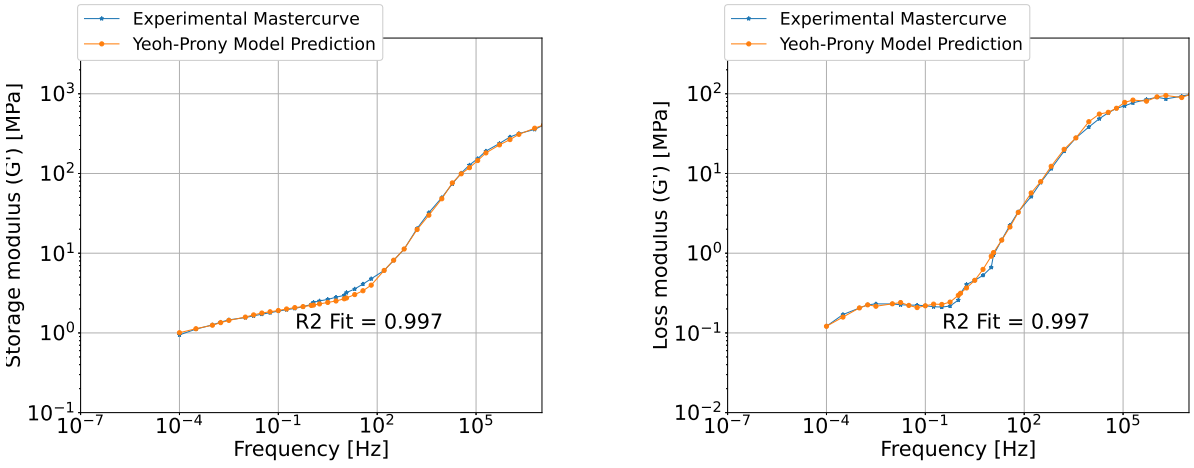

(a) Storage modulus (G')

(b) Loss modulus (G')

Figure A.6: Material model calibration of coating material B357-FV15 with Yeoh hyperelastic model and Prony series approximation to DMTA based mastercurve.

Table A.2: Yeoh hyperelastic model and Prony series approximation model parameters for coating B357-FV15 .

Hyperelastic Model: Yeoh parameters			
C10 [Mpa]	4.42E+08	**D1** $[\frac{1}{Mpa}]$	2.71e-10
C20 [Mpa]	0	**D2** $[\frac{1}{Mpa}]$	0
C30 [Mpa]	0	**D3** $[\frac{1}{Mpa}]$	0

Viscoelastic Model: Prony Parameters					
i	g_i **[Pa]**	τ_i **[ms]**	**i**	g_i **[Pa]**	τ_i **[ms]**
1	0.000247	1000	**9**	0.0871686	1.00E-05
2	0.000372	100	**10**	0.135651	1.00E-06
3	0.000392	10	**11**	0.15202	1.00E-07
4	0.000324	1	**12**	0.160863	1.00E-08
5	0.000365	0.1	**13**	0.166768	1.00E-09
6	0.000881	0.01	**14**	0.115523	1.00E-10
7	0.00585	0.001	**15**	0.148929	1.00E-11
8	0.023579	0.0001			

A.3 B368-FV30

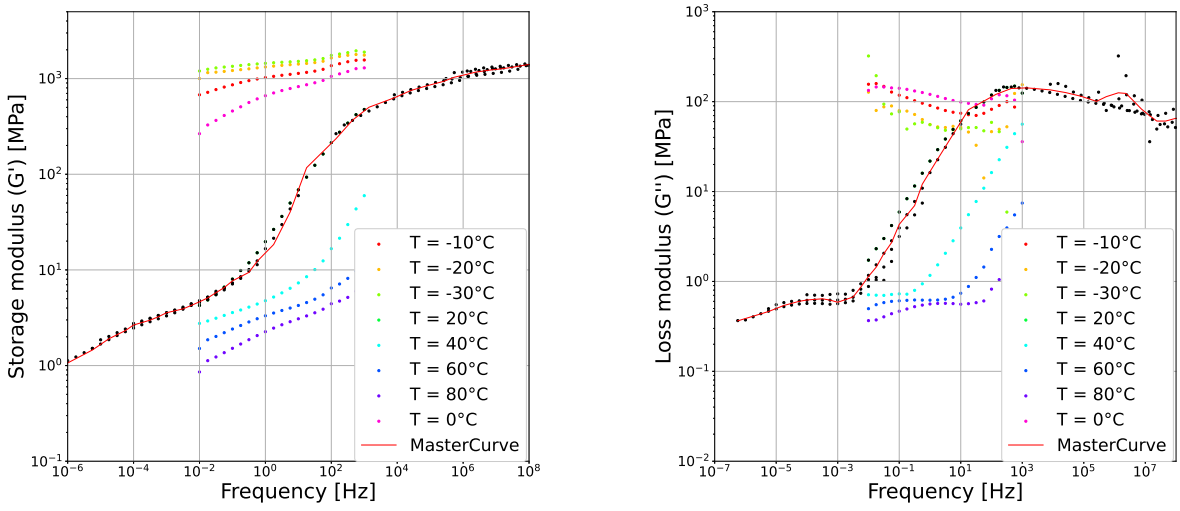

(a) Storage modulus (G')

(b) Loss modulus (G")

Figure A.7: Master-curve construction of coating material B368-FV30 before and after applying horizontal shifts to individual DMTA frequency sweeps.

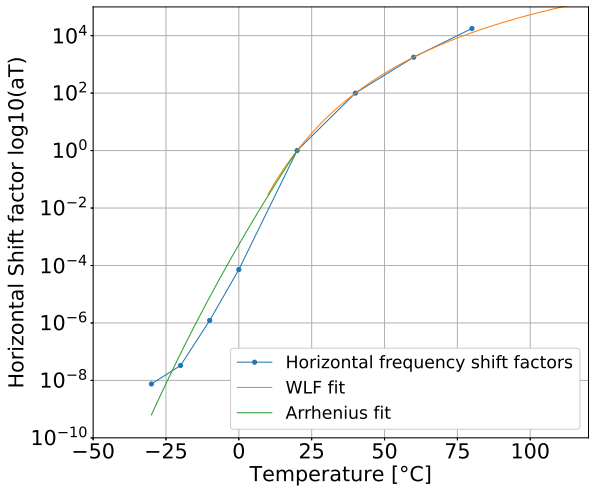

Figure A.8: Coating material B368-FV30 raw shift factor data, overlaid with WLF and Arhenius fit .

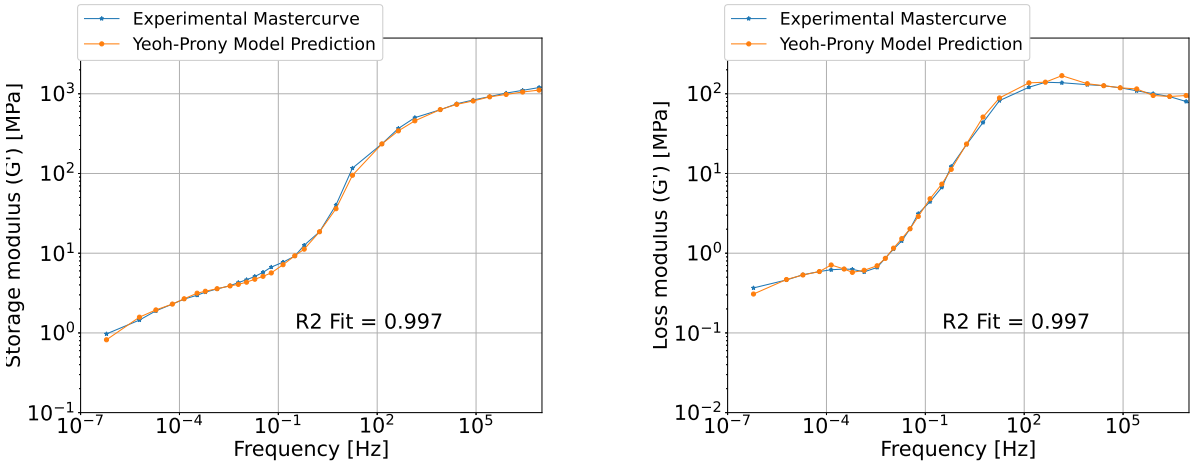

(a) Storage modulus (G')

(b) Loss modulus (G')

Figure A.9: Material model calibration of coating material B368-FV30 with Yeoh hyperelastic model and Prony series approximation to DMTA based mastercurve.

Table A.3: Yeoh hyperelastic model and Prony series approximation model parameters for coating B368-FV30.

Hyperelastic Model: Yeoh parameters			
C10 [Mpa]	6.77E+08	**D1** $[\frac{1}{Mpa}]$	1.20e-10
C20 [Mpa]	0	**D2** $[\frac{1}{Mpa}]$	0
C30 [Mpa]	0	**D3** $[\frac{1}{Mpa}]$	0

Viscoelastic Model: Prony Parameters					
i	g_i **[Pa]**	τ_i **[ms]**	**i**	g_i **[Pa]**	τ_i **[ms]**
1	0.00061368	100000	**9**	0.146896	0.001
2	0.00048212	10000	**10**	0.190489	0.0001
3	0.0008309	1000	**11**	0.129424	1.00E-05
4	0.00045841	100	**12**	0.133708	1.00E-06
5	0.00087888	10	**13**	0.088303	1.00E-07
6	0.00332181	1	**14**	0.123544	1.00E-08
7	0.00983196	0.1	**15**	0.002227	1.00E-09
8	0.0927053	0.01	**16**	0.07576	1.00E-10

A.4 B368-FV15

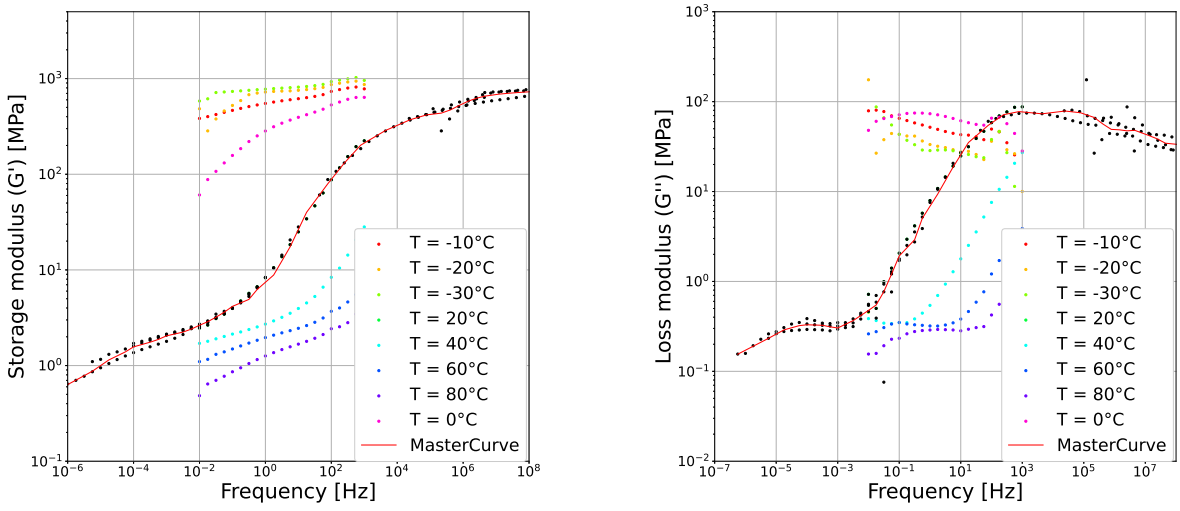

(a) Storage modulus (G')

(b) Loss modulus (G")

Figure A.10: Master-curve construction of coating material B368-FV15 before and after applying horizontal shifts to individual DMTA frequency sweeps.

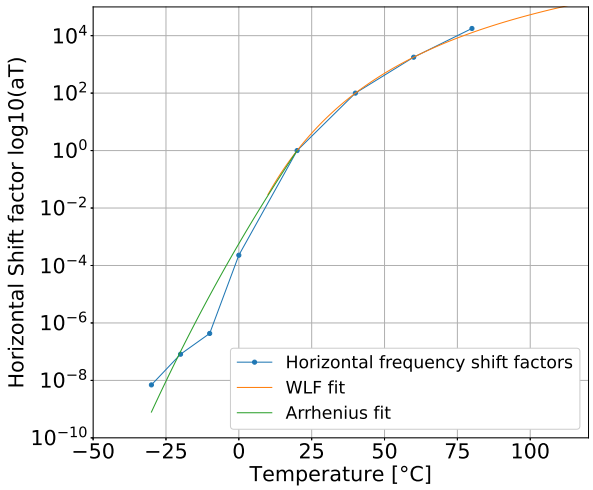

Figure A.11: Coating material B368-FV15 raw shift factor data, overlaid with WLF and Arhenius fit .

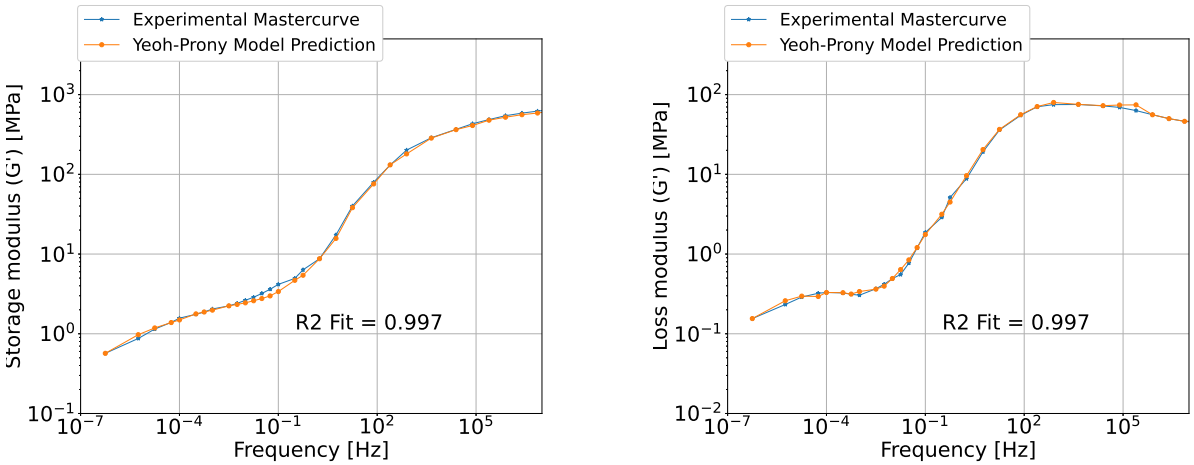

(a) Storage modulus (G')

(b) Loss modulus (G')

Figure A.12: Material model calibration of coating material B368-FV15 with Yeoh hyperelastic model and Prony series approximation to DMTA based mastercurve.

Table A.4: Yeoh hyperelastic model and Prony series approximation model parameters for coating B368-FV15.

Hyperelastic Model: Yeoh parameters			
C10 [Mpa]	3.77E+08	**D1** $[\frac{1}{Mpa}]$	1.86e-10
C20 [Mpa]	0	**D2** $[\frac{1}{Mpa}]$	0
C30 [Mpa]	0	**D3** $[\frac{1}{Mpa}]$	0

Viscoelastic Model: Prony Parameters					
i	g_i **[Pa]**	τ_i **[ms]**	**i**	g_i **[Pa]**	τ_i **[ms]**
1	0.000587	100000	**10**	0.180571	0.0001
2	0.000521	10000	**11**	0.126161	1.00E-05
3	0.000671	1000	**12**	0.163776	1.00E-06
4	0.000598	100	**13**	0.0860861	1.00E-07
5	0.000619	10	**14**	0.0952436	1.00E-08
6	0.002754	1	**15**	0.0654033	1.00E-09
7	0.007858	0.1	**16**	0.0737329	1.00E-10
8	0.062467	0.01	**17**	0.000115649	1.00E-11
9	0.132147	0.001			

APPENDIX B

Appendix B - SPIFT

B.1 Temperature Profiles

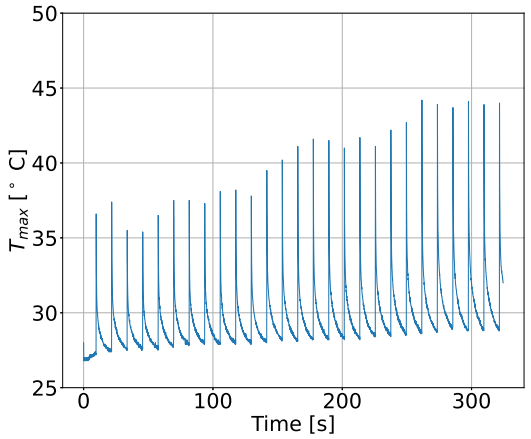

(a) B357-FV15

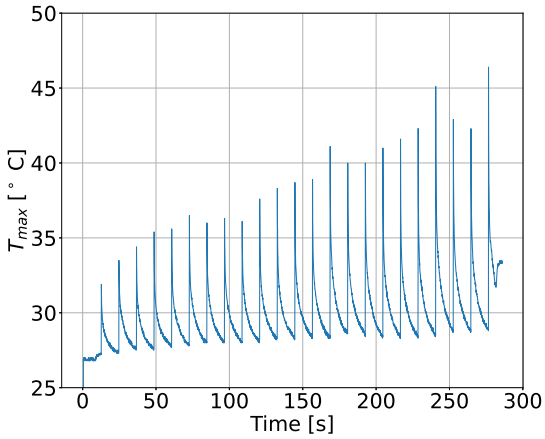

(b) B357-FV15

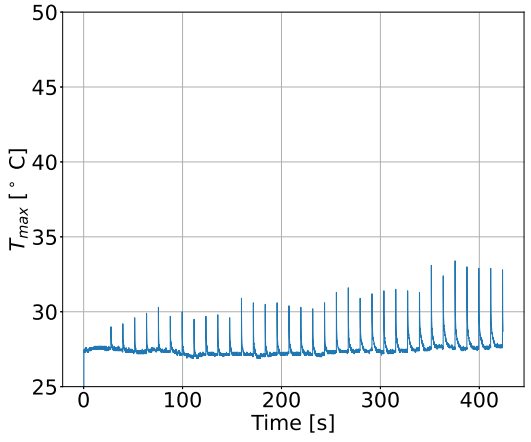

(c) B368-FV30

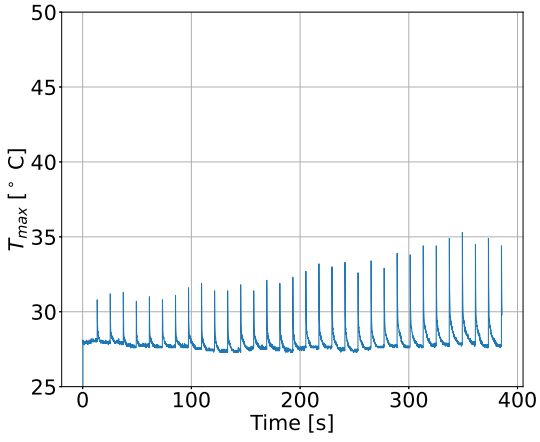

(d) B368-FV15

Figure B.1: Preliminary SPIFT test raw temperature profiles.

B.2 Impact Fatigue

Table B.1: SPIFT impact fatigue test: Damage detection raw data files link.

Material	Test ID	V_{impact}	URL
B357-FV30	A-1	174.54	https://video.dtu.dk/media/SPIFT_B357-FV30_V175/0_1jrrbrvn
	A-2	165.01	https://video.dtu.dk/media/SPIFT_B357-FV30_V165/0_s8c0osqc
B357-FV15	B-1	171.45	https://video.dtu.dk/media/SPIFT_B357-FV15_V175/0_xd2wg87d
	B-2	167.36	https://video.dtu.dk/media/SPIFT_B357-FV15_V165/0_5y6ov5e7
B368-FV30	C-1	176.41	https://video.dtu.dk/media/SPIFT_B368-FV30_V175/0_gebaiiuc
	C-2	170.51	https://video.dtu.dk/media/SPIFT_B368-FV30_V170/0_7343n4mm
	C-3	164.79	https://video.dtu.dk/media/SPIFT_B368-FV30_V165/0_xlyvokkc
	C-4	158.86	https://video.dtu.dk/media/SPIFT_B368-FV30_V160/0_c3s5eg1l
	C-5	156.44	https://video.dtu.dk/media/SPIFT_B368-FV30_V155/0_7wpf0xac
B368-FV15	D-1	175.19	https://video.dtu.dk/media/SPIFT_B368-FV15_V175/0_5d06tbw4
	D-2	170.41	https://video.dtu.dk/media/SPIFT_B368-FV15_V170/0_qw1hcqbe
	D-3	166.75	https://video.dtu.dk/media/SPIFT_B368-FV15_V166/0_datzqimf
	D-4 (1)	162.74	https://video.dtu.dk/media/SPIFT_B368-FV15_V162_Test1/0_nc68reuv
	D-4 (2)	162.74	https://video.dtu.dk/media/SPIFT_B368-FV15_V162_Test2/0_3fc086zg
	D-5	155.77	https://video.dtu.dk/media/SPIFT_B368-FV15_V155/0_ei5nosvg

APPENDIX C

Appendix C - RET Prediction

C.1 Pressure profiles

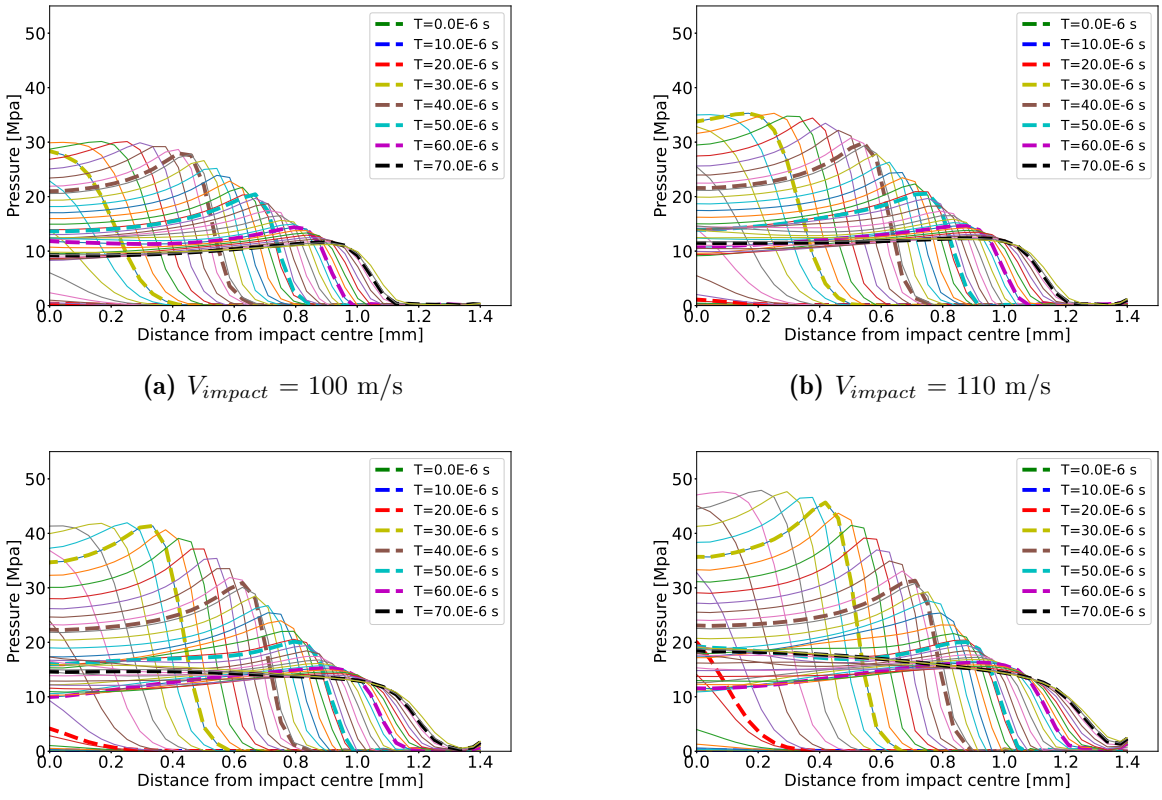

(a) $V_{impact} = 100$ m/s

(b) $V_{impact} = 110$ m/s

(c) $V_{impact} = 120$ m/s

(d) $V_{impact} = 130$ m/s

Figure C.1: Pressure profiles for liquid droplet impact on coating material B357-FV30 for impact velocities of 100-130 m/s.

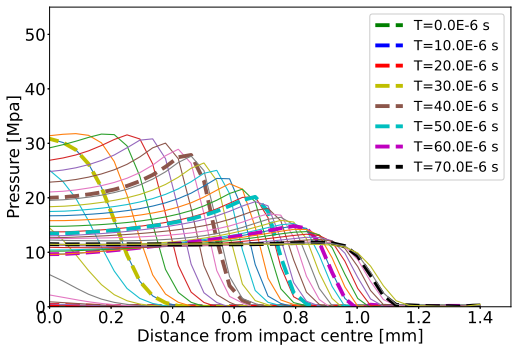

(a) $V_{impact} = 100$ m/s

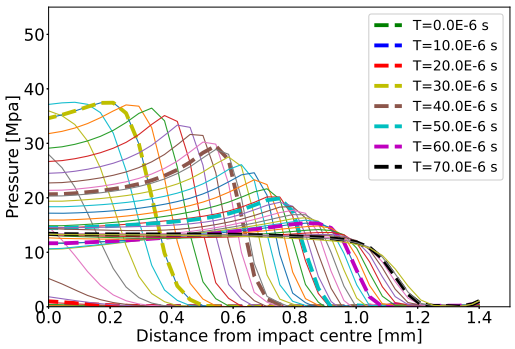

(b) $V_{impact} = 110$ m/s

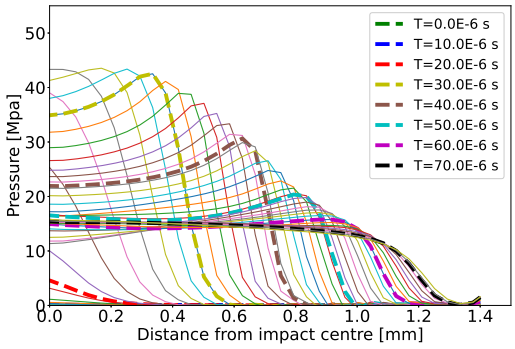

(c) $V_{impact} = 120$ m/s

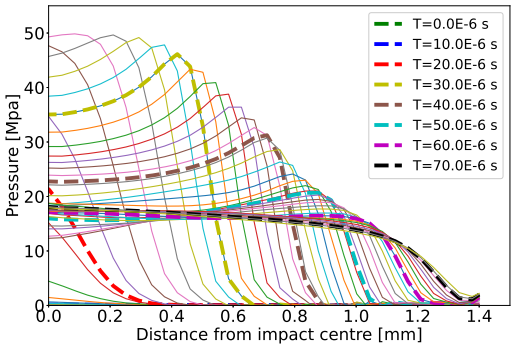

(d) $V_{impact} = 130$ m/s

Figure C.2: Pressure profiles for liquid droplet impact on coating material B357-FV15 for impact velocities of 100-130 m/s.

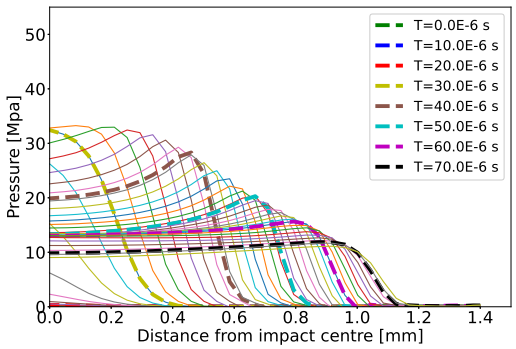

(a) $V_{impact} = 100$ m/s

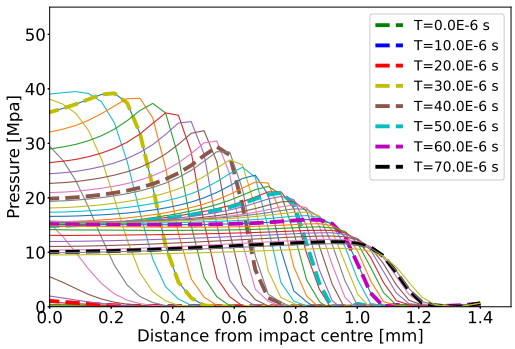

(b) $V_{impact} = 110$ m/s

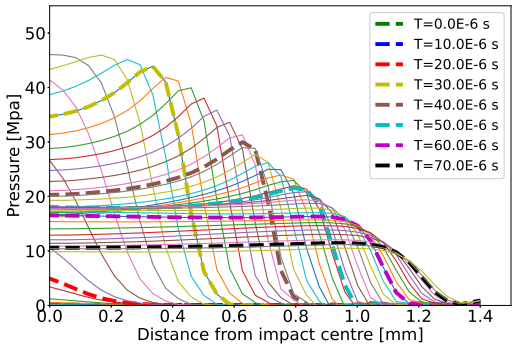

(c) $V_{impact} = 120$ m/s

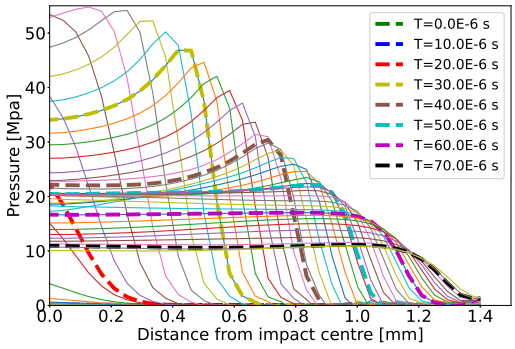

(d) $V_{impact} = 130$ m/s

Figure C.3: Pressure profiles for liquid droplet impact on coating material B368-FV30 for impact velocities of 100-130 m/s.

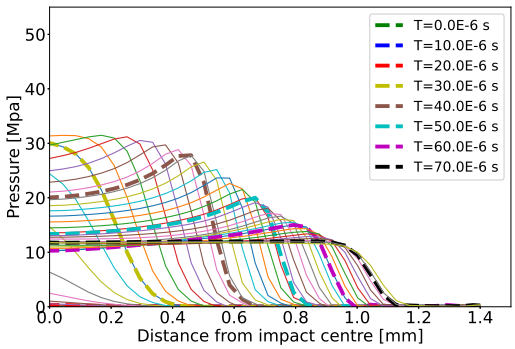

(a) $V_{impact} = 100$ m/s

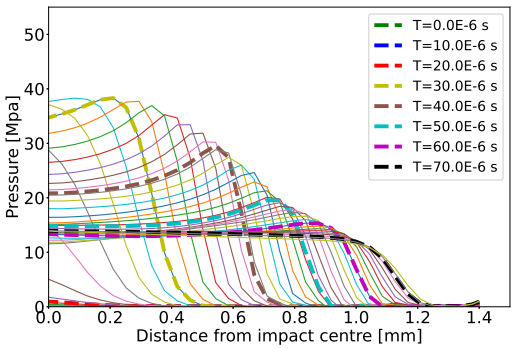

(b) $V_{impact} = 110$ m/s

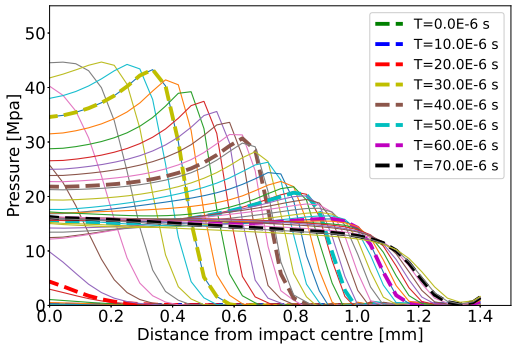

(c) $V_{impact} = 120$ m/s

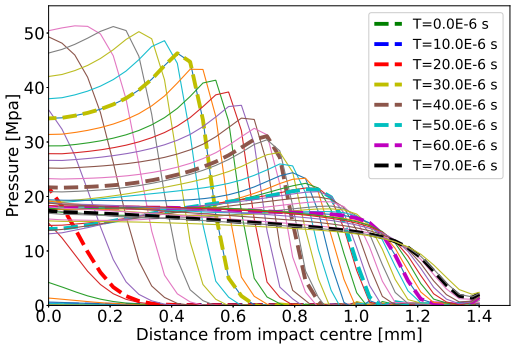

(d) $V_{impact} = 130$ m/s

Figure C.4: Pressure profiles for liquid droplet impact on coating material B368-FV15 for impact velocities of 100-130 m/s.

Bibliography

[1] AeroNordic. "Rain Erosion Testing". In: (2022). URL: https://www.aero-nordic.com/lep-rain-erosion-testing/.

[2] Mehmet Bakırcı and Sezayi Yılmaz. "Theoretical and computational investigations of the optimal tip-speed ratio of horizontal-axis wind turbines". In: *Engineering Science and Technology, an International Journal* 21.6 (2018), pages 1128–1142. ISSN: 2215-0986. DOI: https://doi.org/10.1016/j.jestch.2018.05.006. URL: https://www.sciencedirect.com/science/article/pii/S2215098618301381.

[3] Jakob Bech, C. Hasager, and Christian Bak. "Extending the life of wind turbine blade leading edges by reducing the tip speed during extreme precipitation events". In: *Wind Energy Science Discussions* (February 2018), pages 1–35. DOI: 10.5194/wes-2017-62.

[4] Jörgen Bergström. "5 - Elasticity/Hyperelasticity". In: *Mechanics of Solid Polymers*. Edited by Jörgen Bergström. William Andrew Publishing, 2015, pages 209–307. ISBN: 978-0-323-31150-2. DOI: https://doi.org/10.1016/B978-0-323-31150-2.00005-4. URL: https://www.sciencedirect.com/science/article/pii/B9780323311502000054.

[5] Stanley Smith Cook. "Erosion by water-hammer". In: *Proceedings of the Royal Society of London. Series A, Containing Papers of a Mathematical and Physical Character* 119.783 (1928), pages 481–488.

[6] Enrique Cortés et al. "On the material characterisation of wind turbine blade coatings: the effect of interphase coating–laminate adhesion on rain erosion performance". In: *Materials* 10.10 (2017), page 1146.

[7] Global Wind Energy Council. "GWEC Global Wind Report 2021". In: *Global Wind Energy Council: Bonn, Germany* (2020).

[8] Laura Cozzi et al. "World Energy Outlook 2020". In: *Paris: IEA* (2020).

[9] Georgios Deskos. "Numerical simulations of wind turbine wakes". In: *Imperial College London, PHD* (2018).

[10] Dr. Nagi Elabbasi Dr. Jorgen Bergstrom. "MCcalibration". In: *PolymerFEM.com* (2020).

[11] Nelson Christopher Dzupire, Philip Ngare, and Leo Odongo. "A poisson-gamma model for zero inflated rainfall data". In: *Journal of Probability and Statistics* 2018 (2018).

[12] Mohammadali Eftekhar. “Finite element simulation of particle impact on protective elastomer coatings for wind turbine blades”. In: (2021). DOI: 10.1016/B978-1-78548-313-4.50002-9.

[13] Drew Eisenberg, Steffen Laustsen, and Jason Stege. “Wind turbine blade coating leading edge rain erosion model: Development and validation”. In: *Wind Energy* 21.10 (2018), pages 942–951.

[14] Mohamed Elhadi Ibrahim and Mamoun Medraj. “Water Droplet Erosion of Wind Turbine Blades: Mechanics, Testing, Modeling and Future Perspectives”. In: *Materials* 13.1 (2020). ISSN: 1996-1944. DOI: 10.3390/ma13010157. URL: https://www.mdpi.com/1996-1944/13/1/157.

[15] JA Epaarachchi. “The effect of viscoelasticity on fatigue behaviour of polymer matrix composites”. In: *Creep and fatigue in polymer matrix composites*. Elsevier, 2011, pages 492–513.

[16] Anthony Fraisse et al. “Impact fatigue damage of coated glass fibre reinforced polymer laminate”. English. In: *Renewable Energy* (2018), pages 1102–1112. ISSN: 0960-1481. DOI: 10.1016/j.renene.2018.04.043.

[17] M Gagnon et al. “Hyperelastic modeling of rubber in commercial finite element software (ANSYSTM)”. In: *McGill University, Department of Mechanical Engineering* (2006).

[18] Joseph A GRAND. “Wind power blades energize composites manufacturing”. In: *Plastics Technology* 54.10 (2008).

[19] Woobeom Han, Jonghwa Kim, and Bumsuk Kim. “Effects of contamination and erosion at the leading edge of blade tip airfoils on the annual energy production of wind turbines”. In: *Renewable Energy* 115 (2018), pages 817–823. ISSN: 0960-1481. DOI: https://doi.org/10.1016/j.renene.2017.09.002. URL: https://www.sciencedirect.com/science/article/pii/S0960148117308649.

[20] Robbie Herring et al. “The increasing importance of leading edge erosion and a review of existing protection solutions”. In: *Renewable and Sustainable Energy Reviews* 115 (2019), page 109382.

[21] Robbie Herring et al. “The increasing importance of leading edge erosion and a review of existing protection solutions”. In: *Renewable and Sustainable Energy Reviews* 115 (2019), page 109382. ISSN: 1364-0321. DOI: https://doi.org/10.1016/j.rser.2019.109382. URL: https://www.sciencedirect.com/science/article/pii/S1364032119305908.

[22] FJ Heymann. “High-speed impact between a liquid drop and a solid surface”. In: *Journal of Applied Physics* 40.13 (1969), pages 5113–5122.

[23] “How to protect wind turbine rotor blades from leading edge erosion?” In: (2009). URL: https://www.polytech.com/wtg-manufacturers/elle-leading-edge-protection/.

[24] Fortune Business Inside. "Horizontal-Axis Wind Turbine Market Report Summaries". In: (). URL: https://www.fortunebusinessinsights.com/horizontal-axis-wind-turbine-market-105719.

[25] IRENA. *Renewable power generation cost in 2021*. Technical report. International Renewable Energy Agency, Abu Dhabi, 2021.

[26] K.M.B. Jansen. "Thermomechanical modelling and characterisation of polymers". In: (2007). DOI: 10.1016/B978-1-78548-313-4.50002-9.

[27] Nicolai Frost-Jensen Johansen. "Test Methods for Evaluating Rain Erosion Performance of Wind Turbine Blade Leading Edge Protection Systems". In: *Technical University of Denmark* (2020).

[28] Mark Hugh Keegan, David Nash, and Margaret Stack. "Wind Turbine Blade Leading Edge Erosion: An investigation of rain droplet and hailstone impact induced damage mechanisms". PhD thesis. University of Strathclyde, 2014.

[29] Mark Hugh Keegan, DH Nash, and MM Stack. "On erosion issues associated with the leading edge of wind turbine blades". In: *Journal of Physics D: Applied Physics* 46.38 (2013), page 383001.

[30] "Leading-Edge Erosion Research Used to Reduce Wind Power Plant Performance Uncertainty". In: (2017). URL: https://www.energy.gov/eere/wind/articles/leading-edge-erosion-research-used-reduce-wind-power-plant-performance.

[31] John S Marshall. "The distribution of raindrops with size". In: *J. meteor.* 5 (1948), pages 165–166.

[32] Leon Mishnaevsky et al. "Materials for Wind Turbine Blades: An Overview". English. In: *Materials* 10.11 (2017). ISSN: 1996-1944. DOI: 10.3390/ma10111285.

[33] Sarthak Misra, K. T. Ramesh, and Allison M. Okamura. "Modeling of Tool-Tissue Interactions for Computer-Based Surgical Simulation: A Literature Review". In: *Presence* 17.5 (2008), pages 463–491. DOI: 10.1162/pres.17.5.463.

[34] Francesco Papi et al. "Numerical Modeling of the Effects of Leading-Edge Erosion and Trailing-Edge Damage on Wind Turbine Loads and Performance". In: *Journal of Engineering for Gas Turbines and Power* 142.11 (2020), page 111005.

[35] Signal Processing. "acoustic properties of Table". In: *https://www.signal-processing.com/table.php* ().

[36] Amrit Shankar Verma et al. "A probabilistic long-term framework for site-specific erosion analysis of wind turbine blades: A case study of 31 Dutch sites". In: *Wind Energy* (2021).

[37] "Siemens sets billions: Ørsted must repair hundreds of turbines". In: (2018). URL: https://www.windaction.org/posts/47883.

[38] M. (2009) Smith. "Abaqus user manual version 6.9". In: *Dassault Systèmes Simulia Corp* (2020).

[39] G S Springer. “Erosion by liquid impact”. In: 0.0 (January 1976). URL: https://www.osti.gov/biblio/6340467.

[40] EE Supeni et al. “Design of smart structures for wind turbine blades”. In: *Proceedings of the 2nd Malaysian Postgraduate Conference (MPC 2012)*. Education Malaysia, Sydney (EMAS). 2012, pages 20–36.

[41] Function Bay Tech support. “What is the difference between a hyperelastic material and an elastic material in RecurDyn?” In: (). URL: https://support.functionbay.com/en/faq/single/87/difference-hyperelastic-material-elastic-material-recurdyn.

[42] Anna-Maria Tilg et al. “Variation of leading-edge-erosion relevant precipitation parameters with location and weather type”. In: *Meteorologische Zeitschrift* 30.3 (2021), pages 251–269.

[43] Piotr Wais. “A review of Weibull functions in wind sector”. In: *Renewable and Sustainable Energy Reviews* 70 (2017), pages 1099–1107.

[44] EWC Wilkins. *Cumulative damage in fatigue*. 1956, pages 321–332.

[45] Weihong Zhang and Yingjie Xu. “Constitutive Models of Polycarbonate”. In: *Mechanical Properties of Polycarbonate* (January 2019), pages 29–77. DOI: 10.1016/B978-1-78548-313-4.50002-9.